Influence of disjoining pressure on the stability of a liquid layer on a hard spherical core with respect to the self-charge

V. A. Koromyslov, M. I. Munichev, and S. O. Shiryaeva

Yaroslavl State University
(Submitted May 20, 1997)
Pis'ma Zh. Tekh. Fiz. **23**, 1–7 (October 12, 1997)

It is shown that the critical value of the Rayleigh parameter characterizing the stability of a thin charged layer of liquid on the surface of a hard spherical core increases rapidly as the thickness of the layer decreases. © *1997 American Institute of Physics.* [S1063-7850(97)00110-9]

The instability of a charged layer of viscous liquid of finite depth on a curvilinear hard substrate is encountered in the theory of thunderstorm electricity in charge micro- and macroseparation processes, and in the nucleation of a streak lightning discharge, in liquid mass spectrometry, and in liquid-metal ion sources.[1–3] An investigation of the stability of a thin layer of liquid on the surface of a hard core is therefore relevant. Of particular interest is the stability of extremely thin liquid films since, according to Refs. 2, 4, and 5, when the thickness of a liquid layer on a hard substrate decreases to $h \leqslant 100$ nm, the disjoining pressure has a substantial influence, its magnitude increasing with decreasing film thickness as $\sim h^{-n}$ (where $3 \leqslant n \leqslant 4$, depending on h).

1. Let us suppose that a hard spherical core of radius R_0 is surrounded by a spherically symmetric spherical layer of viscous ideally conducting liquid of outer radius R and charge Q. We shall assume that the liquid is incompressible with the kinematic viscosity ν, density ρ, and surface tension σ. The velocity field of the capillary wave motion $\mathbf{U}(\mathbf{r},t)$, the pressure field $P(\mathbf{r},t)$, and the distortion of the free liquid surface $\xi(\mathbf{r},t)$ caused by the thermal capillary wave motion will be assumed to be of the same order of smallness. We take the external medium to be vacuum and perform the analysis in a spherical coordinate system with its origin at the center of the core, using a linear approximation for the small parameters ξ, U, and P, and dimensionless variables, where $R=1$, $\rho=1$, and $\sigma=1$.

The linearized system of hydrodynamic equations describing the capillary motion of a viscous liquid in this system will have the form:

$$\frac{\partial \mathbf{U}}{\partial t} = -\frac{1}{\rho}\nabla P^{\text{in}} + \nu \cdot \Delta \mathbf{U}; \tag{1}$$

$$\text{div}\mathbf{U} = 0; \tag{2}$$

$$r = R_0: \quad U_r = 0, \quad U_\theta = 0, \quad U_\varphi = 0; \tag{3}$$

$$F(\mathbf{r},t) \equiv r - 1 - \xi(\theta,t) = 0:$$

$$\frac{dF}{dt} \equiv \frac{\partial F}{\partial t} + \mathbf{U}\cdot\nabla F = 0; \tag{4}$$

$$\boldsymbol{\tau}\cdot(\mathbf{n}\cdot\nabla)\mathbf{U} + \mathbf{n}\cdot(\boldsymbol{\tau}\cdot\nabla)\mathbf{U} = 0; \tag{5}$$

$$-(P^{\text{in}} - P^{\text{ex}}) + 2\rho\nu\mathbf{n}\cdot(\mathbf{n}\cdot\nabla)\mathbf{U} + P_\sigma - P_E - P_h = 0. \tag{6}$$

In these expressions $\mathbf{n}$ and $\boldsymbol{\tau}$ are the unit vectors of the normal and tangent to the free surface of the liquid, P^{ex} is the pressure of the external medium on the surface of the droplet, P^{in} is the pressure inside the liquid, P_σ is the Laplace pressure beneath the spherical surface of the liquid layer distorted by the wave motion:[6]

$$P_\sigma = 2 - (2 + \Delta_\Omega)\xi(\theta,t);$$

Δ_Ω is the angular component of the Laplace operator in spherical coordinates.

The electric field pressure P_E on the surface of a charged, ideally conducting droplet is given by:[6]

$$P_E = \frac{Q^2}{8\pi} - \frac{1}{2\pi}Q^2\xi + \frac{1}{4\pi}Q^2 \times \sum_{m=0}^{\infty}(m+1)P_m(\mu)\int_{-1}^{1}\xi P_m(\mu)\,d\mu,$$

$P_m(\mu)$ are normalized Legendre polynomials, $\mu \equiv \cos\theta$.

The author of Ref. 4 isolates four components of the disjoining pressure, which are of different physical natures and cannot generally be described by a single analytic expression. However, for a qualitative analysis of the influence of the disjoining pressure P_h on the stability of thin films, we confine ourselves to the h dependence of the fluctuating component of the disjoining pressure, as was done in a theoretical analysis of the stability of free thin films:[7]

$$P_h = \frac{A}{h^n}\left(1 - \frac{n}{h}\xi(\theta,t)\right),$$

where $h \equiv 1 - R_0$.

2. Solving Eqs. (1)–(6) by a scalarization method described in detail in Ref. 6 yields a dispersion relation for the poloidal capillary motion of the liquid in this system:

$$\det A \equiv \begin{vmatrix} A_{11} & A_{12} & A_{13} & A_{14} & A_{15} \\ A_{21} & A_{22} & A_{23} & A_{24} & A_{25} \\ A_{31} & A_{32} & A_{33} & A_{34} & A_{35} \\ A_{41} & A_{42} & A_{43} & A_{44} & A_{45} \\ A_{51} & A_{52} & A_{53} & A_{54} & A_{55} \end{vmatrix} = 0; \tag{7}$$

$$A_{11} = m; \quad A_{12} = -(m+1); \quad A_{13} = m(m+1)i_m\left(\sqrt{\frac{S}{\nu}}\right);$$

$$A_{14} = m(m+1)k_m\left(\sqrt{\frac{S}{\nu}}\right); \quad A_{15} = -S; \quad A_{21} = 2(m-1);$$

$$A_{22}=-2(m+2);$$

$$A_{23}=-2\sqrt{\frac{S}{\nu}}i_{m+1}\left(\sqrt{\frac{S}{\nu}}\right)+\left[\frac{S}{\nu}+2(m+1)(m-1)\right]i_m\left(\sqrt{\frac{S}{\nu}}\right);$$

$$A_{24}=2\sqrt{\frac{S}{\nu}}k_{m+1}\left(\sqrt{\frac{S}{\nu}}\right)+\left[\frac{S}{\nu}+2(m+1)(m-1)\right]k_m\left(\sqrt{\frac{S}{\nu}}\right);$$

$$A_{25}=0;\quad A_{31}=S+2\nu m(m-1);$$

$$A_{32}=S+2\nu(m+1)(m+2);$$

$$A_{33}=2\nu m(m+1)\left[\sqrt{\frac{S}{\nu}}i_{m+1}\left(\sqrt{\frac{S}{\nu}}\right)+(m-1)i_m\left(\sqrt{\frac{S}{\nu}}\right)\right];$$

$$A_{34}=2\nu m(m+1)\left[-\sqrt{\frac{S}{\nu}}k_{m+1}\left(\sqrt{\frac{S}{\nu}}\right)+(m-1)k_m\left(\sqrt{\frac{S}{\nu}}\right)\right];$$

$$A_{35}=(m-1)(m+2)+\frac{nA}{h^{(n+1)}}-W(m-1);$$

$$A_{41}=mR_0^{(m-1)};\quad A_{42}=-(m+1)R_0^{-(m+2)};$$

$$A_{43}=\frac{m(m+1)}{R_0}i_m\left(\sqrt{\frac{S}{\nu}}R_0\right);$$

$$A_{44}=\frac{m(m+1)}{R_0}k_m\left(\sqrt{\frac{S}{\nu}}R_0\right);\quad A_{45}=0;$$

$$A_{51}=R_0^{(m-1)};\quad A_{52}=R_0^{-(m+2)};$$

$$A_{53}=\sqrt{\frac{S}{\nu}}i_{m+1}\left(\sqrt{\frac{S}{\nu}}R_0\right)+\frac{(m+1)}{R_0}i_m\left(\sqrt{\frac{S}{\nu}}R_0\right);$$

$$A_{54}=-\sqrt{\frac{S}{\nu}}k_{m+1}\left(\sqrt{\frac{S}{\nu}}R_0\right)+\frac{(m+1)}{R_0}k_m\left(\sqrt{\frac{S}{\nu}}R_0\right);$$

$$A_{55}=0,$$

where $W\equiv Q^2/4\pi$, S is the complex frequency, and $i_m(x)$ and $k_m(x)$ are spherical Bessel functions of the first and third kinds, respectively.

Results of numerical calculations made using Eq. (7) are plotted in Fig. 1 as dependences of the growth rates of the first five even modes, whose numbers are indicated on the curves, as functions of the dimensionless radius of the core calculated for $W=13$, $\nu=0.01$, $n=3$, and $A=10^{-7}$. It can be seen that as the film thickness decreases, the instability growth rates fall sharply because of viscous dissipation in the liquid layer and at the solid bottom. This case was examined in Ref. 8. We are only interested in the region $h<100$ nm, where the critical value of the Rayleigh parameter W will depend not only on the mode number m but also on the layer thickness h. Figures 2 and 3 show the right-hand section of Fig. 1 on an enlarged scale with and without allowance for the disjoining pressure, respectively ($A=10^{-7}$ — Fig. 2 and $A=0$ — Fig. 3). Figure 2 shows that the range of stable values of W for a particular mode will be determined by its number and by the degree of supercriticality of the charge. For instance, it can be seen that the dominant mode depends most strongly on the layer thickness but because of the low degree of supercriticality of the charge, the critical values of the parameter W for the tenth mode differ very little from

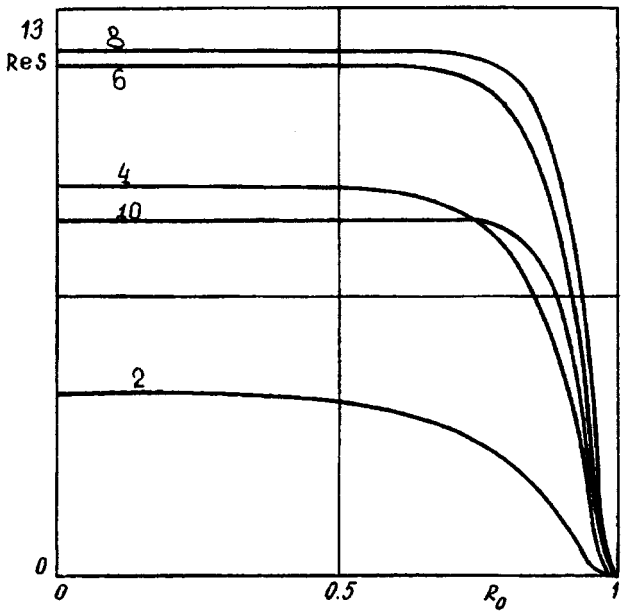

FIG. 1. Dimensionless growth rates of the first few unstable even modes (numbers are shown on the curves) as a function of the dimensionless core radius R_0, calculated for $\nu=0.01$, $W=13$, $n=3$, and $A=10^{-7}$.

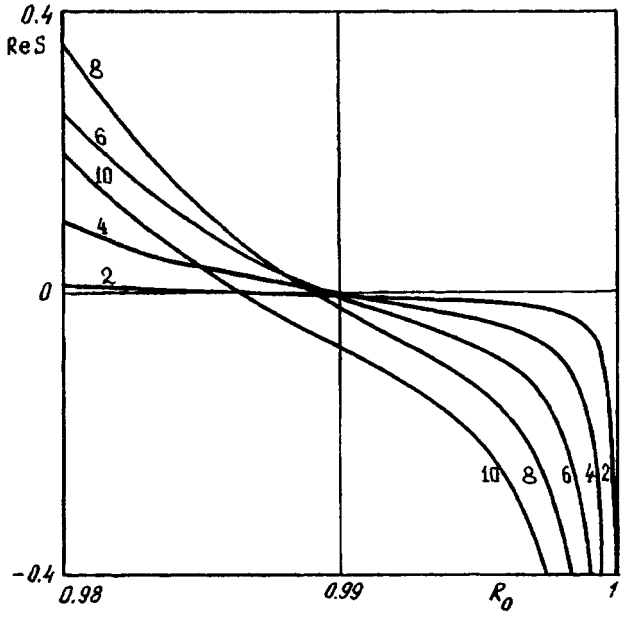

FIG. 2. Enlarged right section of Fig. 1 with allowance for the disjoining pressure ($A=10^{-7}$).

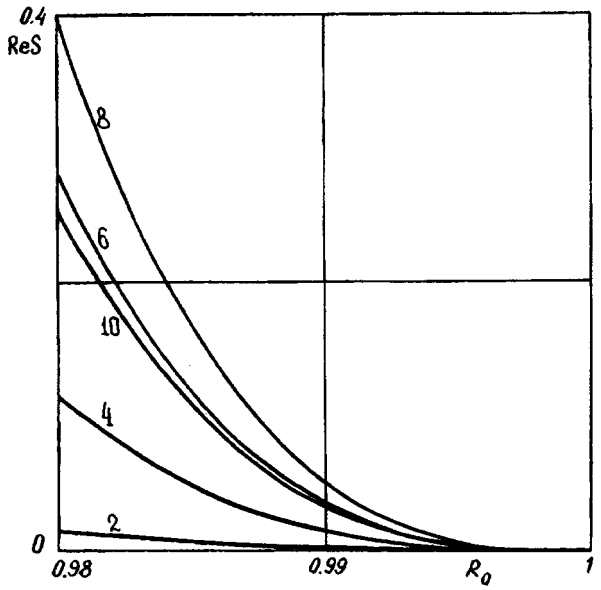

FIG. 3. Enlarged right section of Fig. 1 neglecting the disjoining pressure ($A=0$).

W_{cr} for the second mode. This result is consistent with the critical dependences of W on the layer thickness[2] obtained previously for an ideal liquid.

To conclude, for extremely thin layers of liquid instability will either occur as a result of the predominant buildup of high-order modes or will not occur at all, depending on the charge. A similar situation was observed by Wagner[9] in an experimental investigation of a needle type of liquid-metal ion source.

[1] A. I. Grigor'ev and S. O. Shiryaeva, Izv. Ross. Akad. Nauk. Mekh. Zhidk. Gaza No. 3, 3 (1994).
[2] A. I. Grigor'ev, M. I. Munichev, and S. O. Shiryaeva, J. Coll. Interface Sci. **166**, 267 (1994).
[3] A. I. Grigor'ev and S. O. Shiryaeva, Physica Scripta **54**, 660 (1996).
[4] J. Frenkel, *The Kinetic Theory of Liquids* (Clarendon Press, Oxford, 1946) [Russ. original, Nauka, Moscow, 1975].
[5] B. V. Deryagin, *Theory of Stability of Colloids and Thin Films* [in Russian], Nauka, Moscow (1986).
[6] S. O. Shiryaeva, A. É. Lazaryants, V. A. Koromyslov *et al.*, *Method of Scalarization for Vector Boundary-Value Problems*, Preprint No. 27 [in Russian], Institute of Mathematics, Russian Academy of Sciences, Yaroslavl (1994).
[7] R. K. Jane and E. Ruckenstein, Lecture Notes Phys. **105**, 140 (1979).
[8] A. I. Grigor'ev, S. O. Shiryaeva, A. I. Koromyslov, and M. I. Munichev, Pis'ma Zh. Tekh. Fiz. **22**(10), 23 (1996) [Tech. Phys. Lett. **22**, 398 (1996)].
[9] A. Wagner and T. M. Hall, J. Vac. Sci. Technol. **16**, 1871 (1979).

Translated by R. M. Durham
Edited by Steve Torstveit

Possible formation of $BaCeO_3$ during deposition of $YBa_2Cu_3O_{7-x}$ films on the surface of cerium oxide

A. D. Mashtakov, I. M. Kotelyanskiĭ, V. A. Luzanov, P. B. Mozhaev, G. A. Ovsyannikov, and I. D. Bdikin

Institute of Radio Engineering and Electronics, Russian Academy of Sciences, Moscow
(Submitted February 20, 1997)
Pis'ma Zh. Tekh. Fiz. **23**, 8–13 (October 12, 1997)

Results are presented from an experimental study of the crystallographic parameters of $(1\underline{1}02)Al_2O_3/(001)CeO_2/(001)YBa_2Cu_3O_{7-x}$ film heterostructures fabricated by cathode sputtering at high substrate temperatures $T=600$-$800\,^\circ$C. It is shown that the main limitation on the temperature for deposition of a $YBa_2Cu_3O_{7-x}$ film on a CeO_2 surface is due to the chemical interaction between $YBa_2Cu_3O_{7-x}$ and CeO_2 to form a polycrystalline $BaCeO_3$ layer.
© *1997 American Institute of Physics.* [S1063-7850(97)00210-3]

When silicon or sapphire, the most popular materials in microelectronics, are used as substrates to grow epitaxial high-temperature superconducting films, a single-crystal ''protective'' sublayer must be used to prevent the diffusion of silicon or aluminum atoms from the substrate into the film during the deposition process. One of the most commonly used materials for this protective sublayer when a high-temperature superconducting $YBa_2Cu_3O_{7-x}$ (YBCO) film is deposited on a sapphire substrate is cerium oxide.[1–4] Cerium oxide has a fluorite-type crystal structure with a cubic unit cell parameter $a=0.541$ nm which differs little ($<1\%$) from the translation in the [110] direction of YBCO. The coefficient of linear expansion of CeO_2 $\alpha\approx10^{-5}\ K^{-1}$ lies between those of YBCO ($\alpha=13\times10^{-6}\ K^{-1}$) and sapphire ($\alpha=8\times10^{-6}\ K^{-1}$) and according to current thinking (see Ref. 4, for instance), CeO_2 does not interact with sapphire and YBCO at the temperatures using to deposit high-temperature superconducting films. It has been shown[1–4] that epitaxial (001) YBCO films with fairly good structural and electrophysical parameters can be deposited on a $(1\underline{1}02)$ Al_2O_3 substrate with a thin (30–50 nm) epitaxial protective (001) CeO_2 sublayer at substrate temperatures of 700–770 °C. However, their superconducting parameters cannot be improved by raising the deposition temperature (as can be done with $NdGaO_3$ and $SrTiO_3$ substrates[4,5]). In addition, when the deposition temperature is increased above 770 °, both the structural and electrophysical parameters of the YBCO films show some deterioration.[3] This constraint on the temperature for deposition of a YBCO film on a protective CeO_2 sublayer may arise because at these relatively high temperatures, either the protective properties deteriorate rapidly or a chemical reaction begins to take place between the CeO_2 and YBCO.

Here we present experimental results which indicate that the main constraint on the temperature for deposition of a YBCO film on a CeO_2 surface is caused by a chemical reaction between YBCO and CeO_2 to form a polycrystalline $BaCeO_3$ layer.

An epitaxial CeO_2 film was deposited on sapphire $(1\underline{1}02)$ substrates by magnetron reactive rf sputtering of a metallic Ce target (99.97% pure) in an argon–oxygen mixture (1:1 by volume) at temperatures of 620–770 °C and a pressure of 0.01 mbar. The thermocouple readings were calibrated with a pyrometer in the absence of a discharge. The target diameter was 70 mm, the distance from the substrate was 20 mm, and the rate of deposition was 5 nm/min. After deposition had ended, the substrate temperature was reduced to 56 °C and the chamber was filled with oxygen to atmospheric pressure. The thickness of the CeO_2 film was 70 nm.

Then, YBCO was deposited on the $(1\underline{1}02)$ sapphire substrate with its protective CeO_2 sublayer by dc cathode sputtering of a stoichiometric ceramic YBCO target at an oxygen pressure of 2.5 mbar. The target diameter was 45 mm, the distance from the substrate was 20 mm, and the discharge current density and voltage were 10 mA/cm^2 and 300 V, respectively. The rate of deposition was 1 nm/min. The substrate temperature was kept constant to within $\pm10\,^\circ$C in the range between 600 and 800 °C. After deposition, the following substrate cooling procedure was carried out: the substrate temperature was first reduced to 560 °C within 5 min in an oxygen plasma (with the discharge switched on), the chamber was then filled with oxygen to atmospheric pressure, and the temperature lowered continuously to 330 °C over 75 min in a continuous stream of oxygen, after which the heater was switched off.[5]

The crystal structure of the CeO_2 and YBCO films was investigated by x-ray diffractometry. These studies showed that over the entire range of deposition temperatures (620–770 °C) the CeO_2 films exhibited preferentially (001)-oriented epitaxial growth. The fraction of (111)-oriented CeO_2 crystallites was very small. The maximum intensity ratio $I(333)/I(002)$ of the diffraction peaks on the θ–2θ scan diffraction pattern of CeO_2 did not exceed 0.008. The lattice constant of CeO_2 $a=0.540$ nm, determined using the $(1\underline{1}02)$ peak of sapphire as the reference point, remained almost constant over this range of deposition temperatures. The full width at half-maximum of the (002) rocking curve peak of $CeO_2\approx0.82°$ decreased slightly with increasing deposition temperature.

The quality of the YBCO epitaxial films was almost independent of the deposition temperature of the CeO_2 sublayer and was determined by their deposition conditions. The temperature range for the growth of a YBCO film with good parameters is limited. At substrate temperatures of 700 °C

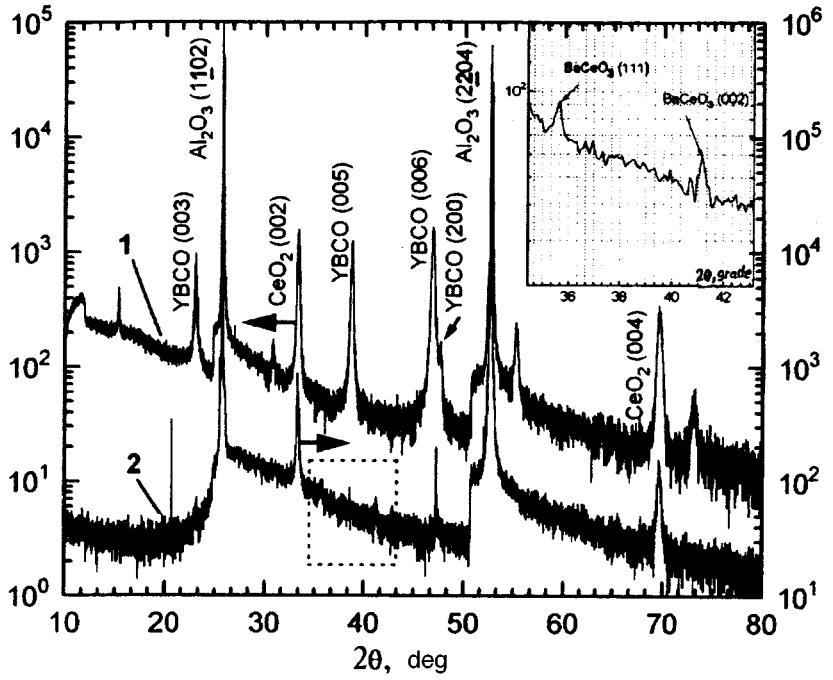

FIG. 1. Diffraction patterns of two $(1102)Al_2O_3/(001)CeO_2/(001)$YBCO heterostructures where the YBCO film is deposited at different temperatures. The diffraction patterns are shifted along the ordinate for clarity: *1* — deposition temperature 710 °C, *2* — 800 °C. The inset shows an enlarged section of pattern *2*, which demonstrates the presence of $BaCeO_3$.

and below, YBCO crystallites are formed with (100)-oriented YBCO. At a deposition temperature of $\approx 700\,^{\circ}$C the intensity ratio of the YBCO peaks is $I(200)/I(006) \approx 0.1$. As the YBCO deposition temperature increased, this ratio decreased and was almost zero at temperatures above 720 °C. At deposition temperatures of 720–750 °C the YBCO films exhibited (001)-oriented epitaxial growth with the full width at half-maximum of the (005) YBCO rocking curve peak $\approx 0.83°$, the parameter $c = 1.1655$ nm, the critical temperature $T_c = 87$–88 K, and the superconducting transition width $\Delta T_c = 0.7$–0.8 K determined from resistive measurements.

When the deposition temperature was increased above 750 °C, in our case the film began to exhibit the properties of an insulator. Figure 1 gives θ–2θ scan patterns of two $(1102)Al_2O_3/(001)CeO_2/(001)$YBCO heterostructures where the YBCO film was deposited at different temperatures (1 — 695 °C and 2 — 770 °C). A comparison between these diffraction patterns reveals the almost complete absence of peaks from the YBCO film for heterostructure 2 for which the YBCO films were deposited at 770 °C. In addition, the intensities of the reflections from the CeO_2 sublayer are between three and four times lower on this diffraction pattern.

The inset shows an enlarged section of pattern 2 which reveals two additional low-intensity diffraction peaks $2\theta \approx 35°40'$ and $2\theta \approx 41°10'$. These peaks cannot be assigned to combinations of the diffraction peaks from sapphire, CeO_2, and YBCO. In our opinion, these peaks may be identified as diffraction peaks from the (111) and (100) planes of a cubic unit cell with the parameter $a = 0.4362$ nm. It is known[6] that the compound $BaCeO_3$ has the perovskite crystal structure with the cubic unit cell parameter $a = 0.4397$ nm. We postulate that these additional peaks correspond to reflections from the (111) and (100) planes of polycrystalline $BaCeO_3$. The decrease in the intensity of the diffraction peaks from the CeO_2 sublayer may be attributed to a reduction in its thickness as a result of the chemical reaction. In fact, the diffraction patterns from layered $(001)CeO_2/(1102)Al_2O_3$ having undergone special annealing at 1000 °C revealed no additional diffraction peaks. Moreover, the intensities of the peaks from (001) CeO_2 increased slightly and the widths of the peaks decreased slightly as a result of the improvement in the structure of the CeO_2 film produced by the annealing. This experiment confirms that no interaction takes place between Al_2O_3 and CeO_2, at least up to 1000 °C.

The onset of the formation of polycrystalline $BaCeO_3$ on the surface of CeO_2 observed during the deposition of a YBCO film at substrate temperatures higher than 770 °C leads to the formation of polycrystalline films whose chemical composition differs from that of $YBa_2Cu_3O_{7-x}$. Thus, the diffraction patterns of these structures exhibit almost no diffraction peaks corresponding to $YBa_2Cu_3O_{7-x}$.

This work was partially supported by the Superconductivity Subgroup of the Russian State Program ''Topical Problems in Condensed-Matter Physics,'' the Russian Fund for Fundamental Research, the INCO-COPERNICUS and INTAS Programs of the European Union, and the Program of Russo-Swedish Collaboration in Superconducting Electronics.

The authors would like to thank Yu. N. Boĭkov, Z. G. Ivanov, and F. V. Komissinskiĭ for their assistance and for helpful discussions.

[1] I. M. Kotelyanskiĭ, V. A. Luzanov, Yu. M. Dikaev *et al*, Sverkhprovodimost' (KIAE) **7**, 1306 (1994).

[2] A. G. Zaitsev, R. Kutzner, and R. Wördenweber, Appl. Phys. Lett. **67**, 2723 (1995).
[3] B. F. Cole, G.-C. Liang, N. Newman *et al.*, Appl. Phys. Lett. **61**, 1727 (1992).
[4] J. M. Owens, E. J. Tarte, P. Beghniur, and R. E. Somekh, IEEE Trans. Appl. Supercond. **5**, 1657 (1995).
[5] P. B. Mozhaev, G. A. Ovsyannikov, S. N. Polyakov *et al.*, Sverkhprovodimost' (KIAE) **8**, 288 (1995).
[6] R. W. G. Wyckoff, *Crystal Structures* (Wiley Interscience, New York, 1964), Vol. 2, p. 310.

Translated by R. M. Durham
Edited by Steve Torstveit

A new possibility for separate measurement of the imaginary and real parts of the third-order nonlinear optical susceptibility of initially isotropic media

I. I. Gancherenok

Belarus State University, Minsk
(Submitted January 23, 1997)
Pis'ma Zh. Tekh. Fiz. **23**, 14–20 (October 12, 1997)

A new possibility for separate measurement of the imaginary and real parts of the cubic optical susceptibility (and for measurement of its phase) of isotropic resonant media is demonstrated theoretically. The theoretical conclusions show good agreement with recent experimental data. © *1997 American Institute of Physics.* [S1063-7850(97)00310-8]

The search for new methods of measuring the cubic optical susceptibility of isotropic media is still attracting interest nowadays.[1] Here the aim is not usually to determine the absolute value of the cubic optical susceptibility but to make separate measurements of the imaginary and real parts of either the effective susceptibility (a combination of the components of $\hat{\chi}^{(3)}$)) or of separate components of the cubic optical susceptibility tensor. The possibility of studying the dispersion of the imaginary and real parts of the cubic optical susceptibility at the same time is also an interesting proposition. In this letter a new method of investigating $\hat{\chi}^{(3)}$ is reported, useful under conditions where the familiar methods do not work.

Since the results of a recent study[2] of the induced anisotropy of a dye solution will be used as experimental confirmation of these theoretical conclusions, the present analysis will be confined to excitation by linearly polarized light which is the most typical for these media. The general algorithm for the theoretical analysis can then be constructed as follows.

1. For a system comprising biharmonic radiation (pump–probe) and an initially isotropic polarization-sensitive medium, the evolution of the vector amplitude of the probe wave may be described as follows:

$$\frac{d\mathbf{E}_1}{dz}=\left(a\hat{S}-\frac{\sigma_1}{2}\hat{I}\right)\mathbf{E}_1=\hat{N}\mathbf{E}_1, \tag{1}$$

where all the parameters appearing in Eq. (1) were identified in a previous study[3] together with the limits of validity of Eq. (1).

2. Adopting the formalism for the differential propagation matrix ($\hat{N}$) advanced by Azzam and Bashara,[4] the equation describing the behavior of the polarization state is

$$\frac{d\chi_1}{dz}=a\Delta\lambda\chi_1, \tag{2}$$

where $\Delta\lambda=\lambda_- -\lambda_+$, λ_i are the eigenvalues of the Hermitian tensor of light-induced anisotropy $\hat{S}$ (Ref. 3), $\chi_1=E_{1v}/E_{1u}$ is a complex variable determining the polarization of the probe wave in an arbitrary basis of the vectors **u** and **v**.

3. In a Cartesian basis, the tensor $\hat{S}$ becomes diagonal. We assume that the pump wave is polarized along the X axis and we calculate the polarization changes to the probe wave as it propagates through a medium whose initial isotropy is impaired by the exciting radiation. The following analysis can be made for the most general case of an elliptically polarized probe wave (here we shall neglect any polarization incoherence of the interacting waves), although the final expressions for the azimuth (θ_1) and the ellipticity (η_1) are extremely cumbersome and cannot be analyzed analytically. Thus, we shall confine our analysis to the case of a linearly and circularly polarized probe beam most frequently encountered experimentally, noting that the case of an elliptically polarized probe wave with the major semiaxis oriented parallel or perpendicular to the X axis, was analyzed in Ref. 3.

1. Linearly polarized probe beam ($\chi_{10}=\tan\theta_{10}$; the subscript ''0'' indicates the value of the parameter characterizing the wave on entry to the medium). The induced rotation of the plane of polarization ($\Delta\theta=\theta_{10}-\theta_1$) and the ellipticity of the probe wave are then defined as

$$\Delta\theta_1=\frac{1}{2}\arctan\left(\frac{\tan 2\theta_{10}-a_1}{1+a_1\tan 2\theta_{10}}\right), \tag{3}$$

$$\eta_1=\tan\left(\frac{1}{2}\arcsin b_1\right), \tag{4}$$

$$a_1=\frac{2\,\mathrm{Re}\,\chi_1}{1-|\chi_1|^2}, \tag{5}$$

$$b_1=\frac{2\,\mathrm{Im}\chi_1}{1+|\chi_1|^2}. \tag{6}$$

It is subsequently convenient to make a numerical analysis of Eqs. (3)–(4), again because of the fairly cumbersome nature of the expressions for $\Delta\theta_1$ and η_1 when all the parameters are identified. Figure 1 gives $\Delta\theta_1$ and η_1 as a function of the azimuth for various pump intensities I. Both figures show that the optimum input azimuth of the probe wave polarization to observe the maximum polarization changes differs from the value of $\pi/4$ reported in the literature[5] and this difference increases with increasing pump intensity. In addition, the values of θ_{10} for which $\Delta\theta_1(\theta_{\Delta\theta})$ and $\eta_1(\theta_\eta)$ have maxima do not coincide, i.e., $\theta_{\Delta\theta}=\theta_\eta$. The induced ellipticity is also a more ''sensitive'' parameter in the sense of the greater asymmetry of $\Delta\theta_\eta(\theta_{10})$ compared with $\theta_{\Delta\theta}(\theta_{10})$. It then follows from expressions (3) and (4) with allowance for Eqs. (2)–(6) that the light-induced linear dichroism

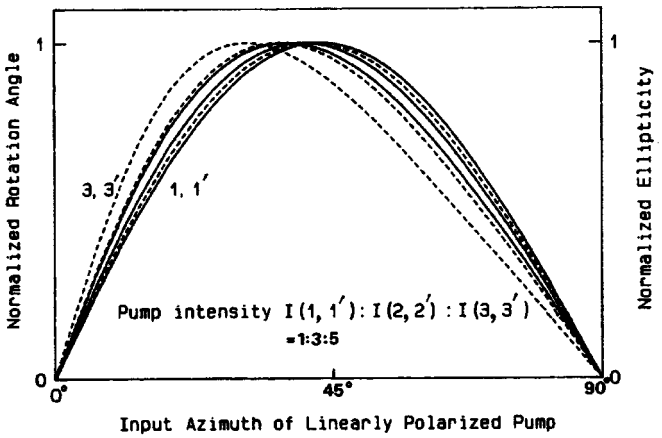

FIG. 1. Theoretical dependences of the normalized light-induced ellipticity (- - - -) and angle of rotation of the plane of polarization (—) of the probe wave as a function of its input azimuth for various pump intensities. The imaginary and real parts of $\chi^{(3)}_{\text{eff}}$ are assumed to be equal.

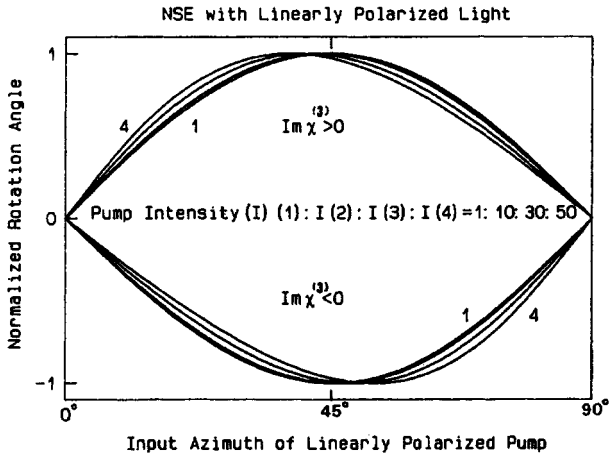

FIG. 2. Azimuthal dependences of the light-induced angle of rotation of the plane of polarization for various pump intensities and $\text{sgn}(\chi^{(3)}_{\text{eff}})$ for different absorption and amplification dichroism.

($\sim \text{Im}(\chi_{1122}+\chi_{1212}) = \text{Im}\chi^{(3)}_{\text{eff}}$) and birefringence ($\sim \text{Re}\chi^{(3)}_{\text{eff}}$) contribute to the rotation of the plane of polarization and are involved in forming the elliptic polarization. However, if the perturbation is fairly weak, the real and imaginary parts can be measured separately since in this case, $\Delta\theta_1$ is determined by $\text{Im}\chi^{(3)}_{\text{eff}}$, and η_1 by $\text{Re}\chi^{(3)}_{\text{eff}}$. Relatively simple calculations yield the following results:

$$\tan\theta_\eta = \pm\exp(-\Delta\lambda\ \text{Re}\ A(z)), \tag{7}$$

$$\eta_{1\max} = \pm\tan\left(\frac{1}{2}\Delta\lambda\ \text{Im}\ A(z)\right), \tag{8}$$

$$(\Delta\theta_1)_{\theta_{10}=\theta_\eta} = \mp\frac{1}{2}\arctan[\sinh(\Delta\lambda\ \text{Re}\ A(z))], \tag{9}$$

where $A(z)$ was determined in Ref. 3 and is proportional to I.

Thus, by measuring θ_η and $\eta_{1\max}$, we can determine separately the real and imaginary parts of the effective cubic optical susceptibility. In addition, relation (9) can also be used to make control measurements for $\text{Im}\chi^{(3)}_{\text{eff}}$. Similar results should be expected from measurements of $\theta_{\Delta\theta}$ and the corresponding polarization changes to the probe wave. In this case, however, a sixth-power algebraic equation must be solved.

2. Circularly polarized probe beam.

Here we have $\chi_{10} = \pm i$, where the ''+'' and ''−'' signs correspond to right and left circular polarization of the probe, both of which are converted into elliptical polarization. It should be stressed that the polarization deformation effect is fairly weak and is only observed in the quadratic approximation in terms of pump wave intensity. We then have

$$\tan 2\theta_1 = \mp\frac{\text{Re}\ \chi^{(3)}_{\text{eff}}}{\text{Im}\ \chi^{(3)}_{\text{eff}}}, \tag{10}$$

$$\sin 2\varepsilon_1 = \pm\left[1-(\Delta\lambda\ \text{Re}\ A(z))^2-\frac{1}{2}\Delta\lambda^2|A(z)|^2\right]. \tag{11}$$

Thus, by measuring the azimuth of the polarization ellipse of the probe beam at the exit from the medium, we can determine the phase of the complex cubic optical susceptibility. This method is preferable because of the high sensitivity of ellipsometric measurements compared with the well-known technique.[6] Attention is also drawn to the precision method of modulation polarization spectroscopy proposed recently for similar purposes.[7]

To conclude, fairly good qualitative agreement is noted between our theoretical results and the experimental data from Ref. 2. However, the smoothing of the experimental values performed in Ref. 2 can scarcely be justified without using a specific theoretical model, indicating the experimental error, and giving a statistical estimate of the consistency between the theoretical curve and the experimental results. Another fundamentally important factor is the choice of probe wavelength relative to the absorption and fluorescence bands, which are in general noncoincident. Absorption and amplification dichroism ''rotate'' the plane of polarization differently (Fig. 2). However, the data on the light-induced polarization changes to the probe beam as a function of the pump intensity given in Ref. 2 partially contradict the results reported in Refs. 8–10. This circumstance, together with the recent experimental observation[11] that the light-induced angle of rotation of the plane of polarization of the probe wave depends nonmonotonically on l, as was predicted in Ref. 9, provides significant motivation for the continuation of theoretical research along these lines.

This work was partially supported by a NATO International Scientific Exchange Programmes–Collaborative Research Grant.

The author would like to thank Doctor T. Dreier (Physikalisch-Chemisches Institut, Heidelberg, Germany) and members of his scientific group for their hospitality during his stay in Germany and for helpful discussions on nonlinear polarization spectroscopy.

[1] N. Tang and J. P. Partanen, Opt. Lett. **21**, 1108 (1996).
[2] L. G. Pikulik, K. I. Rudik, V. A. Chernyavskiĭ *et al.*, Zh. Prikl. Spektrosk. **63**, 242 (1996).
[3] I. I. Gancheryonok, Rev. Laser Eng. **20**, 502 (1992).
[4] R. M. Azzam and N. M. Bashara, *Ellipsometry and Polarized Light* (North-Holland, Amsterdam, 1977; Mir, Moscow, 1981).
[5] H. E. Lessing and J. Von Jena, *Laser Handbook* (North-Holland, Amsterdam, 1986), pp. 793–796.
[6] N. Ma, L. H. Acioli, A. S. L. Gomes *et al.*, Opt. Lett. **16**, 630 (1991).
[7] O. A. Kulikovskaya, *Nonlinear Modulation Polarization Spectroscopy of Bacteriorhodopsin-based Media*, Author's Abstract of Candidate's Dissertation [in Russian], Chernovtsy (1996); V. B. Taranenko, V. Yu. Bazhenov, and O. A. Kulikovskaya, Pure Appl. Opt. **5**, 731 (1996).
[8] A. I. Kurasbediani and V. V. Mumladzde, *Optoelectronics, Quantum Electronics, and Applied Optics* [in Russian], Metsniereba, Tbilisi (1980), pp. 122–128.
[9] V. A. Gaisyonok, I. I. Gancheryonok, and P. G. Zhavrid, Technical Digest of Papers presented at the 15th International Conference on Coherent and Nonlinear Optics, St. Petersburg, 1995, Vol. 1, pp. 431–432.
[10] I. I. Gancheryonok, P. G. Zhavrid, and V. A. Gaĭsenok, Abstracts of Papers presented at the Second International Conference on Laser Physics and Spectroscopy, Grodno, Belarus [in Russian], pp. 25–26.
[11] J. Joseph, F. J. Aranda, D. V. G. L. N. Rao *et al.*, Opt. Lett. **21**, 1499 (1996).

Translated by R. M. Durham
Edited by Steve Torstveit

Concept of low-entropy compression as applied to the development of chemically clean hypersonic wind tunnels

I. V. Sokolov

Institute of General Physics, Russian Academy of Sciences, Moscow
(Submitted April 28, 1997)
Pis'ma Zh. Tekh. Fiz. **23**, 21–25 (October 12, 1997)

An analysis of the thermodynamic constraints on the possible development of chemically clean hypersonic wind tunnels (in which the air temperature remains below the oxidation temperature of nitrogen) yields the conclusion that the acceleration of the gas stream before entering the supersonic nozzle in these wind tunnels should be nonsteady-state. Thermodynamically ideal parameters are determined for this system and technical solutions are proposed. © *1997 American Institute of Physics.* [S1063-7850(97)00410-2]

The concept of low-entropy supercompression is known from laser fusion.[1] The goal is to develop the highest possible material density ρ subject to a pressure constraint $P(\rho,s)$ (s is the entropy). To achieve this, s should have the lowest possible value, equal to the initial value of s in the uncompressed material. Isentropic compression requires the absence of shock waves and is achieved in a simple wave[2] generated by an accelerated shell.

It will be shown that the physical problems encountered in the development of hypersonic wind tunnels are in many respects similar to the problem of low-entropy compression and, in principle, may be solved by the same method.

For the flow of an air stream around objects at the velocity v typical of re-entry into the atmosphere, the hypersonic wind tunnel should have the following characteristics (T is the temperature):

$$P_0 \sim 1 \text{ Torr}, \quad T_0 \sim 250\text{K}, \quad v_0 \cong 4-5 \text{ km/s},$$

$$h_0 = \frac{\gamma}{\gamma-1}\frac{P_0}{\rho_0} + \frac{v_0^2}{2} \cong 10 \text{ MJ/kg}, \tag{1}$$

where $\gamma = 1.4$ is the adiabatic exponent. It is convenient to introduce the specific enthalpy h because in the absence of heating h = const in a steady-state stream, and for bulk heating by an external source $dh = dQ$, where dQ is the heat imparted per unit mass of gas.

In a conventional hypersonic wind tunnel facility, high values of h are achieved by heating the stationary ($v = 0$) gas in a high-pressure chamber from which a steady-state (with conservation of h) flow of gas emerges via a supersonic nozzle. However, at $v = 0$ the enthalpy (1) corresponds to a temperature $T_s \cong 6 \times 10^3$ K at which nitrogen undergoes appreciable oxidation.[2] If the composition of the air in the hypersonic wind tunnel is to match the chemical composition of the upper layers of the atmosphere, the temperature throughout the acceleration process should not exceed the critical values

$$T \leqslant T_c \cong 2000-2500 \text{ K}. \tag{2}$$

In order to overcome the inconsistency between the high value of T_s and condition (2), the authors of Ref. 3 suggested that for moderate $h \cong 3$ MJ/kg the enthalpy deficit $h_0 - h$ in the high-pressure chamber could be made up by heating the flow in a supersonic nozzle using a high-power laser or a microwave generator.[1] However, the thermodynamic constraints on $h_0 - h = \int dQ$ indicate that this approach is unsatisfactory.[4] The first law of thermodynamics gives:

$$dQ = dU + v\,dv = dU - dP/\rho, \tag{3}$$

where U is the internal energy. The work done by the gas is equated to the kinetic energy increment $d(v^2/2)$ and the equation $\rho v\,dv/dx = -dP/dx$ is then used. It is assumed for simplicity that the initial temperature is $T_m = T_c$. In order to find the constraint on h_0, for given initial and final values of ρ_{in}, $T_{\text{in}} = T_c$, ρ_0, P_0 we determine the maximum amount of heat $h_0 - h = \int dQ$ which may be transferred to the gas stream without violating condition (2).

It follows from the property of maximizing the work done in the Carnot cycle (second law of thermodynamics) that the maximum of the functional $\int dQ$ is achieved in a Carnot half cycle: heating and expansion of the gas in the supersonic nozzle should take place isothermally as far as the state $T = T_c$, $\rho = \rho_f = \rho_0 (T_c/T_0)^{1/(\gamma-1)} \sim 10^{-4}$–$10^{-3}$ g/cm^3, which is related to the final state by an adiabatic curve. No heating should take place downstream. Equation (3) gives:

$$h_0 - h \leqslant RT_c \ln(\rho_{\text{in}}/\rho_f) \sim 0.6 \text{ MJ/kg} \ \ln(\rho_{\text{in}}/\rho_f), \tag{4}$$

and even for $\rho_{\text{in}} \sim 0.5$ g/cm^3 the enthalpy increment is insufficient to obtain (1).

With allowance for Eq. (4), the gas stream should have a fairly high value of h on entry to the supersonic nozzle (before heating), which cannot be achieved by steady-state flow from a high-pressure chamber without violating condition (3). The system for acceleration of the gas entering the supersonic nozzle should be nonsteady-state, so that h may increase.[2]

Let us consider the following problem. Let us analyze the nonsteady-state acceleration of a gas flow by a piston moving at the velocity $V(t)$. At zero time $t = 0$ the gas is at rest, with the gas parameters T_s, ρ_s, the speed of sound c_s, and the initial distance between the piston and the supersonic nozzle is equal to L. We shall determine the maximum enthalpy which can be imparted to the gas without violating condition (2).

This problem is similar to that of low-entropy compression. The highest possible value of h is achieved by com-

pression without the formation of a shock wave, i.e., in a simple Riemann wave. Then $c=c_s+2v(\gamma-1)$ (Ref. 2) and assuming condition (2) we have:

$$h_{\max}=\frac{c_{\max}^2}{\gamma-1}+\frac{v_{\max}^2}{2}=\frac{c_s^2}{\gamma-1}\left[\frac{T_c}{T_s}+\frac{2}{\gamma-1}\left(\sqrt{\frac{T_c}{T_s}}-1\right)^2\right]. \tag{5}$$

The first term in brackets is associated with heating and the second with the kinetic energy. As a result of the large coefficient $2/(\gamma-1)\approx 7$, the contribution of the kinetic energy predominates when $T_c>1.3\,T_s$. If we impose the constraint that the entire mass of gas should acquire the enthalpy (5), the dependence $V(t)$ becomes quite specific:

$$V=\frac{2c_s}{\gamma-1}\left[\left(1-\frac{t}{\tau}\right)^{-\frac{\gamma-1}{\gamma+1}}-1\right], \quad t<\tau\left[1-\left(\frac{T_c}{T_s}\right)^{-\frac{\gamma+1}{2\gamma-2}}\right],$$

$$V=\frac{2c_s}{\gamma-1}\left(\sqrt{\frac{T_c}{T_s}}-1\right), \quad \tau\left[1-\left(\frac{T_c}{T_s}\right)^{-\frac{\gamma+1}{2\gamma-2}}\right]<t<\tau,$$

$$\tau=L/c_s. \tag{6}$$

This is accompanied by the formation of a uniform gas plug of length $l=L(T_s/T_c)^{1/(\gamma-1)}$ and

$$v=\frac{2c_s}{\gamma-1}\left(\sqrt{\frac{T_c}{T_s}}-1\right), \quad c=c_s\sqrt{\frac{T_c}{T_s}},$$

$$\rho=\rho_s\left(\frac{T_c}{T_s}\right)^{1/(\gamma-1)}=\rho_s L/1. \tag{7}$$

The value of the enthalpy corresponds to that given by Eq. (5) and at $T_s=280$ K, $T_c=2000$ K is $h\cong 10$ MJ/kg. After expansion and heating of the air plug in the supersonic nozzle with a further increase in enthalpy, its value exceeds that required by Eq. (1) with some margin. This leads us to conclude that a chemically clean (i.e., compliant with condition (2)) hypersonic wind tunnel may be developed by nonsteady-state acceleration of the air before it enters the nozzle and radiative heating in the supersonic nozzle.

For applications, a compromise is needed between thermodynamically ideal systems (giving upper bounds and exclusion principles) and technical possibilities. For instance, a realistic proposition is a system in which a moving gas plug is created by a shock tube[2] and then enters a supersonic nozzle, where it is heated and accelerated. In this case, $h_0\sim 10$ MJ/kg can also be achieved.

Finally, during the acceleration process the air may be present as frozen blocks rather than in the gas phase. This results in the following system: a Snowblast[3] accelerates frozen blocks to a velocity of $\cong 5$ km/s and projects them into a microwave furnace which vaporizes the blocks during their transit time. A steady-state (!) flow of air is obtained at the exit.

In this system the requirements for the radiative heating power are reduced to realistic levels, but the problem of accelerating even a single frozen block (currently being studied in connection with the injection of fuel pellets in a fusion reactor[5]) poses appreciable technical difficulties.

The author would like to thank A. V. Krasil'nikov (Central Scientific-Research Institute of Mechanical Engineering) for consultations, and I. A. Kossyĭ (Institute of General Physics of the Russian Academy of Sciences) and M. Caplan (LLNL) for drawing his attention to work under the US DOE Project No. W-7405-ENG-48.

[1)]It may also be feasible to heat the gas using a powerful neutron flux from a nuclear reactor. Note that although nonradiative methods of heating a gas stream are used in existing hypersonic wind tunnels, their contribution to the final enthalpy is negligible.

[2)]It must be stressed that nonsteady-state acceleration of the flow is specifically required and numerous nonsteady-state methods of generating a high pressure in a gas at rest in a high-pressure chamber (using an electric discharge, explosion, implosion, accelerated pistons) do not solve the problem.

[3)]A special snowthrower: ''With mightly blowers it engulfed the snow which both plows piled, and hurled it in a herculean arc beyond the runway's edge.'' – Arthur Hailey, *Airport.*

[1] E. I. Zababakhin and I. E. Zababakhin, *The Phenomenon of Unbounded Cumulation* [in Russian], Nauka, Moscow (1988).
[2] Ya. B. Zel'dovich and Yu. P. Raizer, *Physics of Shock Waves and High-Temperature Hydrodynamic Phenomena*, Vols. 1 and 2, transl. of 1st Russ. ed. (Academic Press, New York, 1966, 1967) [Russ. original, 2nd ed., Nauka, Moscow, 1966].
[3] R. B. Miles, G. L. Brown, W. R. Lempert *et al.*, AIAA J. **33**, 1463 (1995).
[4] M. Caplan, I. Kossyi, I. Sokolov, and V. Silakov, Report No. UCL-CR-124366, S/C-B319818, Lawrence Livermore National Laboratory (1996).
[5] B. M. Manzon, Usp. Fiz. Nauk, **134**, 611 (1981) [Sov. Phys. Usp. **24**, 662 (1981)].

Translated by R. M. Durham
Edited by Steve Torstveit

Possible method of reducing annealing temperatures of radiation defects in ion-implanted silicon carbide

Z. V. Dzhibuti, N. D. Dolidze, G. Sh. Narsiya, and G. L. Éristavi

Iv. Dzhavakhishvili State University, Tbilisi
(Submitted April 8, 1997)
Pis'ma Zh. Tekh. Fiz. **23**, 26–29 (October 12, 1997)

It is shown that the temperatures of post-implantation annealing of radiation defects in silicon carbide may be reduced by pulsed photon treatment. With a correct choice of spectral composition and radiation energy, pulsed photon treatment is effective for annealing radiation defects through the selective absorption of photons at the corresponding levels. It is suggested that the annealing mechanism is ionizational (annealing under these experimental conditions cannot be explained by a thermal mechanism alone). © *1997 American Institute of Physics.* [S1063-7850(97)00510-7]

Silicon carbide has recently attracted considerable interest as a widely used material for fabricating high-temperature semiconductor devices and optoelectronics devices. However, some difficulties are encountered in the fabrication of devices using this material because of the need to carry out diffusion processes at high temperatures.[1] The use of ion implantation as a method of doping in silicon carbide does not eliminate the need for high-temperature heat treatment — in this case it is required for annealing of radiation defects and activation of implanted impurities ($T>1600$ K) (Ref. 1).

Here we consider a possible method of reducing the post-implantation heating temperatures for silicon carbide samples. Samples of 6H-SiC ($n=2\times10^{18}$ cm^{-3}) were implanted with B^+ ions of energy $E=50$ keV to a dose $\Phi=6\times10^{15}$ cm^{-2}. Post-implantation annealing of radiation defects involved pulsed photon treatment. The photon sources were halogen lamps with a tungsten filament or xenon flashlamps with a flash duration $\tau=10^{-2}$ s. At the flash durations obtained in the halogen-lamp annealing the maximum temperature of the samples could be measured with a Chromel–Alumel thermocouple (0.1 mm thick).[2]

The investigations involved measuring the optical transmission spectra, assuming that in the irradiated crystals any change in the optical transmission is mainly caused by absorption at radiation defects introduced by the ion implantation.[3] It can be seen from the experiment that after ion implantation in SiC samples, the optical transmission is reduced appreciably in the spectral range studied (see Fig. 1, curve *1*). Exposure to a single xenon radiation pulse (50 J/cm^2) increases the transmission over the entire spectral range (curve *2*), although a further increase in the number of pulses to twenty causes no significant changes. A different picture is observed when the sample is exposed to one or several halogen lamp flashes of 90 W/cm^2 power and 10 s duration, which does not produce any appreciable change in the transmission spectrum. However, the subsequent action of a single xenon radiation pulse is sufficient to produce a considerably greater increase in the optical transmission than in the first case, particularly in the short-wavelength part of the spectrum (curve *3*). The same results may be achieved by the action of a single, higher-power, halogen lamp flash ($P=300$ W/cm^2, $\tau=10$), in which case the temperature of the sample does not exceed 1100 K. Subsequent pulses of xenon radiation no longer have any effect (curve *4*).

These results cannot be attributed exclusively to a thermal mechanism, considered by most researchers to be the main mechanism when analyzing similar experiments on other semiconductor materials.[4] However, these results can easily be explained by a mechanism based on changes in the quantum state of the crystal electronic subsystem in the presence of photon irradiation.[5–8] It can be seen from the experiment that in addition to the power, another important factor is the spectral composition of the radiation. This observation also supports an ionization mechanism where the use of sources with a broad photon energy spectrum (unlike lasers) may act selectively on defects with different activation energies, causing them to undergo rearrangement or annealing at lower temperatures.[9,10]

These results suggest that by optimizing the spectral composition and radiation power, the use of pulsed photon

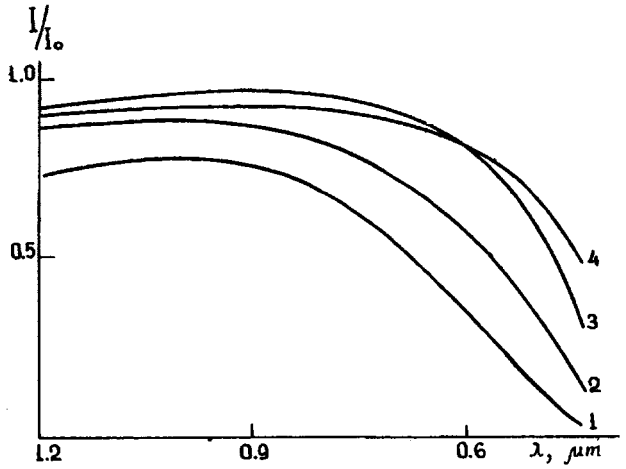

FIG. 1. Spectral dependence of the relative transmission of B^+-implanted 6H-SiC ($E=50$ keV, $\Phi=6\times10^{15}$ cm^{-3}) exposed to pulsed photon treatment: *1* — after ion implantation, *2* — pulsed photon treatment with xenon lamp ($E=50$ J/cm^2, $\tau=10^{-2}$ s), *3* — pulsed photon treatment with halogen lamps ($P=90$ W/cm^2, $\tau=10$ s) and with a xenon lamp ($E=50$ W/cm^2, $\tau=10$ s), and *4* — pulsed photon treatment with halogen lamps ($P=300$ W/cm^2, $\tau=10$ s).

treatment for post-implantation heating of SiC may appreciably reduce the annealing temperatures.

[1] Yu. M. Tairov and V. F. Tsvetkov, in *Handbook of Electrical Engineering Materials*, Vol. 3, edited by Yu. V. Koritskiĭ, V. V. Pasynkov, and B. M. Tareev [in Russian], Énergatomizdat, Leningrad (1988), pp. 446–472.
[2] V. V. Gusakov, A. P. Kovarskiĭ, V. V. Popov, and B. E. Samorukov, Vopr. Radioélektron. Ser. Tekh. Proizvod. Oborud. No. 1, 45 (1986).
[3] V. V. Bolotov, N. B. Pridachin, and L. S. Smirnov, Fiz. Tekh. Poluprovodn. **10**, 566 (1976) [Sov. Phys. Semicond. **10**, 338 (1976)].
[4] A. V. Dburechenskiĭ, G. A. Kachurin, E. V. Nidaev, and L. S. Smirnov, *Pulsed Annealing of Semiconductor Materials* [in Russian], Nauka, Moscow (1982).
[5] V. V. Kapaev, Yu. V. Kopaev, and S. N. Molotkov, Mikroélektronika **12**, 499 (1983).
[6] I. G. Gverdtsiteli, A. B. Gerasimov, Z. V. Dzhibuti, and M. G. Pkhakadze, Poverkhnost' No. 11, 132 (1985).
[7] A. G. Ital'yantsev, V. N. Mordkovich, and É. M. Temper, Fiz. Tekh. Poluprovodn. **18**, 928 (1984) [Sov. Phys. Semicond. **18**, 577 (1984)].
[8] A. B. Gerasimov, Z. V. Dzhibuti, M. A. Kuprava, and M. G. Pkhakadze, Soobshch. Akad. Nauk Gruzii **145**, No. 1, 67 (1992).
[9] Z. B. Dzhibuti and N. D. Dolidze, Pis'ma Zh. Tekh. Fiz. **17**(5), 41 (1991) [Sov. Tech. Phys. Lett. **17**, 172 (1991)].
[10] A. B. Gerasimov, N. D. Dolidze, R. M. Donina, B. M. Konovalenko, G. L. Ofengeim, and A. A. Tsertsvadze, Phys. Status Solidi A **70**, 23 (1982).

Translated by R. M. Durham
Edited by Steve Torstveit

Use of a Sagnac interferometer for measurements of linear nonreciprocal birefringence in a transverse magnetic field

D. V. Shabanov and M. A. Novikov

Institute of Applied Physics, Russian Academy of Sciences, Nizhniĭ Novgorod
(Submitted February 26, 1997)
Pis'ma Zh. Tekh. Fiz. **23**, 30–34 (October 12, 1997)

A method of measuring phase nonreciprocity in materials using a Sagnac interferometer is proposed and implemented in which the working point is shifted into the region of maximum slope of the interference pattern by means of an absorbing exit mirror. The principal advantage of this method over the laser technique is that there are no stringent constraints on the losses in the materials. This method was used for the first time at 0.83 μm to measure the nonreciprocal linear birefringence in a $LiIO_3$ crystal in a transverse magnetic field. © *1997 American Institute of Physics.* [S1063-7850(97)00610-1]

Optical interferometry using a Fizeau–Sagnac ring interferometer is used in various applications and, with particular success, in optical gyroscopy. Interest has recently been focused on nonreciprocal optical effects with a view to their practical use for developing nonreciprocal elements for linearly polarized waves, and also for studying new fundamental phenomena in materials located in an external magnetic field or in magnetically ordered media (crystals). A well-known nonreciprocal optical effect is the Faraday effect, involving circular nonreciprocal birefringence in a longitudinal magnetic field. A lesser known effect is the nonreciprocal linear birefringence in a transverse magnetic field, which is due to spatial dispersion and which in some classes of crystals is manifested as a nonreciprocal change in the refractive index for linearly polarized light waves propagating in opposite directions in a transverse magnetic field. This change is proportional to the magnetic field, and its sign depends on the direction of the field. The effect is attributed to the appearance of a nonzero fourth-rank tensor in the expansion of the electric displacement vector:[4]

$$D=\varepsilon_{ij}\cdot E_j+\gamma_{ijkl}\cdot \partial E_j/\partial x_k\cdot H_{0l}+\ \ldots, \tag{1}$$

where H_{0l} is the external applied magnetic field. The factor with the derivative may be replaced by $K_k E_j$, where K is the wave vector (we omit the $\sqrt{-1}$), whereupon we find that the size of the effect for a given magnetic field is inversely proportional to the wavelength. Nonreciprocal linear birefringence was predicted in Refs. 2–4 and was observed experimentally in Ref. 1 using a ring laser. In the experiment of Ref. 1, where the nonreciprocal linear birefringence in a $LiIO_3$ crystal was measured for the first time, the sample was placed in a ring laser cavity in the path of the counterpropagating waves. The nonreciprocal change in the refractive index observed when a transverse magnetic field was applied to the sample led to the establishment of a frequency difference between the counterpropagating waves which was used to determine the change in the refractive index in the crystal. However, this technique imposes very stringent requirements as to the absence of bulk absorption and to the optical homogeneity of the crystal. The aim of the present study is to propose and implement a method of measuring nonreciprocal phase effects which does not have these disadvantages and can be used for measurements of various materials at 0.83 μm. We propose to use a Fizeau–Sagnac interferometer. To do this we developed a system based on a three–mirror Fizeau–Sagnac interferometer, shown in Fig. 1, where *1* is an emitting laser diode, *2* is a semitransmitting mirror with losses, *3* and *4* are nontransmitting mirrors, *5* is a photodiode detector, *6* is a semitransmitting mirror, and *7* is a photodiode detector used to align the system. The use of an interferometer can appreciably relax the requirements as to the optical homogeneity of the sample and the mirrors.

In a Sagnac interferometer the interfering beams propagate in different directions but around the same ring system. Thus, to measure the nonreciprocal phase difference the working point must be shifted into the region of maximum sensitivity by delaying one beam relative to the other by a quarter wavelength. The standard procedure for solving this problem by inserting a nonreciprocal phase element inside the ring interferometer poses serious technical difficulties associated with the development of this element. In our case, the problem was solved more simply by using an absorbing[5] beam splitter *2* and an asymmetric (lateral) exit from the interferometer. The signal at the working exit is formed from two interfering beams: the beam reflected twice by the beam splitter *2*, and the beam transmitted twice through the beam splitter *2*. Thus, the interference signal also incorporates an additional phase difference proportional to the difference between the reflection and transmission phases. The output signal may be expressed as the following sum:

$$I_{\text{out}}=I_r+I_t+2\sqrt{I_r\times I_t}\,\cos(df+(f_{t1}+f_{t2}-f_{r1}-f_{r2})), \tag{2}$$

where I_r and I_t are the powers of the beams twice transmitted and twice reflected by the mirror, respectively, and f_{t1}, f_{t2} and f_{r1}, f_{r2} are the angles of transmission and reflection. For a lossless exit mirror this difference is 180° and does not influence the phase difference of the counterpropagating waves. As a result of losses, this difference can be made arbitrary, including 90°, the value which is required to shift the working point into the region of maximum sensitivity. The beam splitter *2* was deposited as two layers: 130 Å nickel and 360 nm SiO_2, giving a phase shift close to 90°. The power supply to the laser diode *1* incorporated photo-

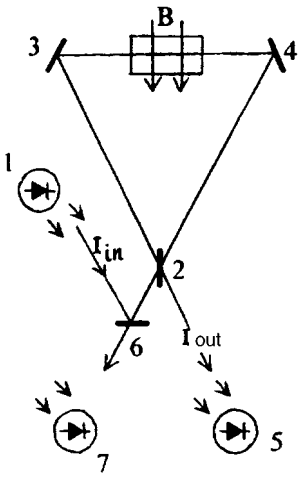

FIG. 1.

current feedback to reduce the level of excess fluctuations of the output radiation. Alignment of the system involved superposing the two interfering beams by aligning the mirrors as follows. Some of the power from the ring system formed by mirrors *2*, *3*, and *4* propagates in the opposite direction and is fed via mirror *6* to the photodetector *7*. This component is formed by two beams: the first transmitted and then reflected by mirror *2* and the second reflected and then transmitted by mirror *2*. In this way the mirror does not introduce any phase shift between these beams, and when their paths are superposed, the result of their summation gives the maximum signal at the photodetector *7*, which is achieved by aligning the mirrors.

The experimental method was as follows:

The crystal being studied was inserted between mirrors *3* and *4* and after aligning the system to give the maximum signal at the photodetector *7*, a transverse magnetic field B was applied to the crystal. For the beams propagating in different directions, the effect has a different sign, i.e., one beam is delayed more than the other, which gives a change in intensity proportional to B when they interfere at the exit, the sign of this change depending on the crystal orientation. The magnetic field is varied with a constant frequency $F=120$ Hz. The measurements were made by a synchronous detection method, which enhances the sensitivity of the system. The change in I_{out} was used to determine the phase difference between the interfering beams from which the required change in refractive index was obtained using the formula $df=kldn$ (df is the phase difference, k is the wave number in vacuum, l is the sample length, and dn is the change in the refractive index). The sensitivity was determined by the noise of the radiation source and the induced signal generated due to the inadequate magnetic field screening and was approximately 10^{-6} rad at $I_{\text{out}}=8\mu$A. This method was used to make measurements at 0.83 μm for two crystals: $LiIO_3$ and potassium dihydrogen phosphate (KDP). A strong, clearly identifiable effect was observed for $LiIO_3$, where the proportionality factor between the change in the refractive index and the magnetic field inducing this change was measured to within 10% as 1.2×10^{-12} Oe^{-1}. The effect was below the sensitivity limit of the system for an orthogonally polarized light wave in $LiIO_3$ and for all polarizations in KDP. For comparison we note that in Ref. 1 the effect was measured in $LiIO_3$ at 0.63 μm and its magnitude was estimated as 2×10^{-12} Oe^{-1}. Thus our results are consistent with the predicted wavelength dependence.

In closing, we should like to thank I. A. Andronova for assistance with the experiment.

[1] V. A. Markelov, M. A. Novikov, and A. A. Turkin, JETP Lett. **25**, 378 (1977).
[2] V. M. Agranovich and V. L. Ginzburg, *Crystal Optics with Spatial Dispersion, and Excitons*, 2nd ed. (Springer-Verlag, New York, 1984) [Russian original, 2nd ed., Nauka, Moscow, 1979].
[3] V. N. Lyubimov, Dokl. Akad. Nauk SSSR **181**, 858 (1968) [*sic.*].
[4] M. A. Novikov, Kristallografiya **24**, 666 (1979) [Sov. Phys. Crystallogr. **24**, 383 (1979)].
[5] K. W. Raines and M. J. Downs, Opt. Acta **25**, 549 (1978).

Translated by R. M. Durham
Edited by Steve Torstveit

Mode selection for a piezoelectric layer in a bulk-acoustic-wave composite acoustic resonator

G. D. Mansfel'd

Institute of Radio Engineering and Electronics, Russian Academy of Sciences
(Submitted April 18, 1997)
Pis'ma Zh. Tekh. Fiz. **23**, 35–41 (October 12, 1997)

An analysis is made of the mode selection for a thin piezoelectric layer in a bulk-acoustic-wave composite layered acoustic resonator by transformation of the impedance using a set of quarter-wave layers. Depending on the number of layers, the impedance of the substrate on which the piezoelectric layer is deposited may be abruptly increased or sharply reduced. This serves to simulate a ''fixed'' or ''free'' surface. As a result, a mechanically strong resonator structure is produced, operating at the natural frequencies of a thin piezoelectric layer. A numerical simulation is made of multilayer structures formed by alternating quarter-wave layers of $LiNbO_3$ and $LiTaO_3$. It is shown that if these layers are of micron thickness and there is a sufficiently large number of them, the acoustic properties of the substrate do not influence the frequency characteristics and Q factor of the thin piezoelectric vibrating layer in the microwave range. © *1997 American Institute of Physics.* [S1063-7850(97)00710-6]

An alternative to conventional resonator elements[1] (surface-acoustic-wave systems, membrane resonators) in the microwave frequency range may be afforded by single-frequency bulk-acoustic-wave resonators operating at the natural frequencies of thin piezoelectric films on mechanically strong substrates. These systems may be developed using the well-known idea of transforming the impedance of the substrate at the interface with the transducer by using quarter-wave layers,[2] which can simulate a mechanically ''free'' or ''fixed'' transducer–substrate interface. In this case, since the layer can be almost completely acoustically isolated from the substrate, the constraints on the layer are reduced — it is only necessary to develop a single perfectly flat surface on which the structure is deposited, and the problems of achieving parallelism and monitoring the thickness of the substrate are eliminated.

Here, an analysis is made of the parameters of multilayer resonator structures in the microwave frequency range using single-crystal $LiNbO_3$ and $LiTaO_3$ layers, which are now technologically feasible to fabricate.

Figure 1 shows the structure of the composite resonator studied. Between an electroacoustic transducer — a layer of piezoelectric *1* with metal electrodes *2* and *2′* — and a substrate *3*, there is a multilayer system of quarter-wave layers formed by materials with alternating different material acoustic impedances Z_1 and Z_2. The system of n quarter-wave layers is designed to transform the input impedance Z_s of the substrate to the desired values $Z_{in}^{(n)}$ at the interface with the transducer. The input electrical impedance Z_e of the composite structure is calculated using a system of boundary conditions which equate the mechanical stresses at the free boundaries to zero and describe the continuity of the strains and mechanical stresses at the interfaces between the layers:[3,4]

$$Z_e=\frac{1}{i\omega C_0}\left[1+\frac{K^2}{1+K^2}\frac{1}{bl}\times\frac{i(Z_m+Z_{m'})Z_0\sin bl-2Z_0^2(1-\cos bl)}{(Z_0^2+Z_mZ_{m'})\sin bl-i(Z_m+Z_{m'})Z_0\cos bl}\right]. \tag{1}$$

Here Z_m and $Z_{m'}$ are the input impedances of the external electrode and the internal metal electrode, which is loaded by the periodic layer structure on the substrate; K is the electromechanical coupling constant of the transducer material, C_0 is the electrical capacitance, b is a complex wave vector which allows for attenuation, Z_0 is the acoustic impedance of the transducer material, and l is its thickness. The input acoustic impedances of all the layers is calculated by employing the following n times in succession:

$$Z_{in}^{(i)}=Z_c^{(i)}\frac{Z_{in}^{(i-1)}\cos b_il_i+iZ_c^i\sin b_il_i}{Z_e^{(i)}\cos b_il_i+iZ_{in}^{(i-1)}\sin b_il_i}, \tag{2}$$

where $Z_l^{(i)}$ is the material acoustic impedance of the ith layer, $Z_{in}^{(i-1)}$ is the input acoustic impedance of the $(i-1)$th layer, b_i are the complex wave vectors for the ith layers, l_i are their thicknesses, $Z_{in}^{(0)}=Z_s$, and $i=0,\ldots,n$.

An analysis is made of a model structure consisting of a substrate formed by a lithium niobate slab with plane-parallel faces, one of which is free and on the surface of the other are systematically deposited n quarter-wave layers of lithium tantalate and lithium niobate, and a transducer layer also made of lithium niobate. The metal electrodes are assumed to be ideally conducting layers of infinitely small thickness, so that $Z_{m'}=Z_{in}^{(n)}$. The velocities and absorption coefficients of the materials were taken from Ref. 5.

Figure 2 shows the transformation of the modulus of the electrical impedance of the structure as a function of the

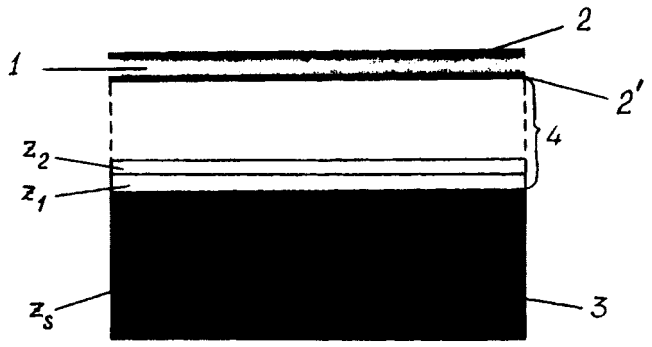

FIG. 1. Structure of composite multilayer acoustic resonator.

frequency and number of layers (n is even). The thickness of the piezoelectric transducer is close to half the wavelength at frequency ≈ 3 GHz. Figure 2a corresponds to the case where there are no quarter-wave layers ($n=0$). Frequency-periodic resonance peaks can be identified (alternating series and parallel resonances). This behavior is typical of a multifrequency composite resonant structure[3] in which the frequencies of the subsequent resonances differ by the fundamental resonance frequency of the structure (the condition for this is that the total phase shift over the thickness of the structure is πm, where m is an integer). The substrate — a relatively thick slab with plane-parallel faces — is responsible for the relatively small intermode spacings. When the number of quarter-wave layers is small ($n=16$), the spacing between the series and parallel resonance frequencies increases (Fig. 2b) and the resonance curves become completely rearranged. For $n=32$ the resonance curve, shown in Fig. 2c, has a single principal minimum and a single principal maximum determined by the parallel and series resonances of the transducer layer. The influence of the substrate, which now plays a negligible role, is observed as small peaks on the resonance curve. For $n=52$ the influence of the substrate almost disappears. The frequency dependences of the modulus and phase

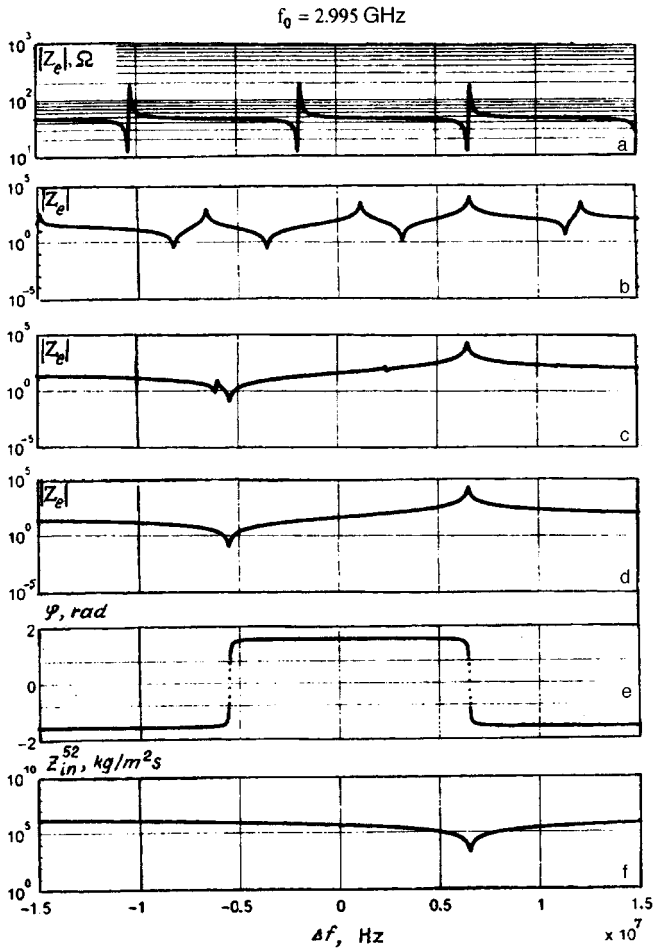

FIG. 2. Frequency dependences of the modulus of the impedance of a composite acoustic resonator with various numbers of layers near the frequency $f_0=2.995$ GHz: a — $n=0$, b — $n=16$, c — $n=32$, d — $n=52$, e,f — frequency dependences of the phase (φ) of the electrical impedance and the modulus of the input acoustic impedance of a multilayer structure at the interface with the transducer with $n=52$.

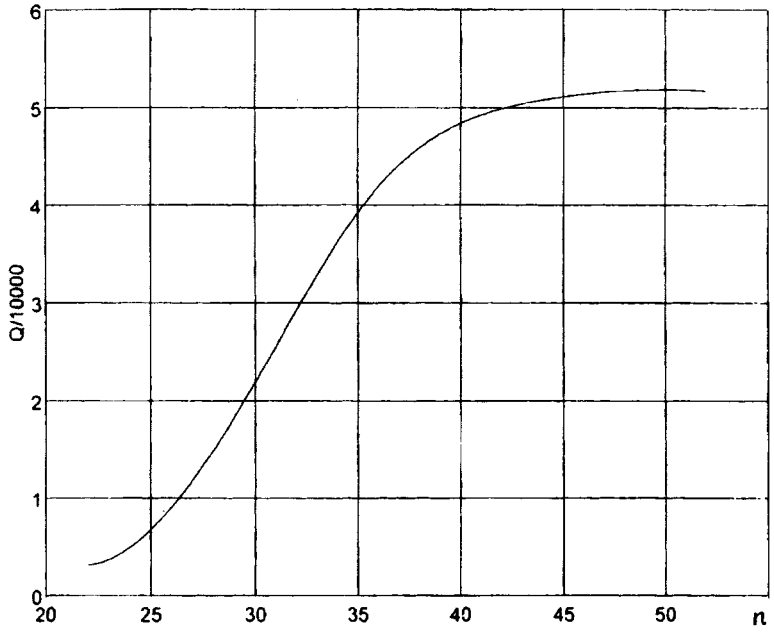

FIG. 3. Resonator Q factor versus the number of layers.

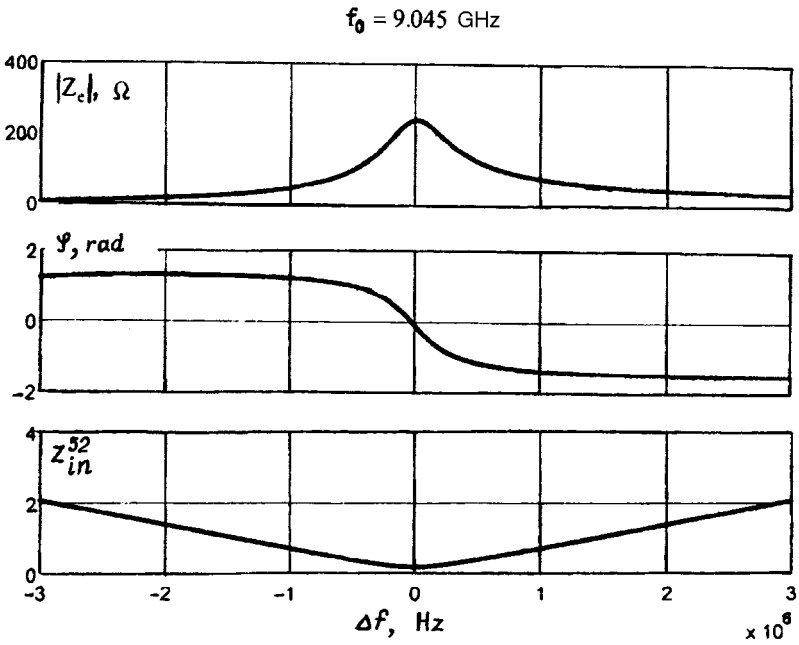

FIG. 4. Frequency dependences of the modulus and phase of the electrical impedance of the structure and of the input acoustic impedance of a multilayer structure at the interface with the transducer at the third harmonic of the parallel resonance (f_0=9.045 GHz).

of Z_e plotted in Figs. 2d and 2e almost correspond to those of a free semiconductor layer, since the acoustic load (Fig. 1f, $Z_{in}^{(52)} \approx 2\times 10^3$ kg/m^{2}s) of the internal boundary of the transducer is small compared with the impedance of the transducer itself ($Z_0 = 3.4\times 10^7$ kg/m^{2}s).

Figure 3 gives the Q factor at the parallel resonance point as a function of the number of layers. For the calculations the boundaries of the pass band were determined from the condition that the phase of the impedance is $\pm\pi/4$. It can be seen that from $n \approx 46$ the influence of the substrate can be neglected. This structure will also operate at harmonics of the natural frequency of a half-wave layer. Figure 4 shows resonance curves of Z_e and $Z_{in}^{(52)}$ at the third harmonic (9 GHz). The Q factor at the parallel resonance frequency is 1.7×10^4.

Note that if there is a large odd number of layers, the impedance at the internal boundary of the transducer, according to Eq. (2), will be much greater than the impedance of the transducer itself. To obtain resonance at the same frequency, the thickness of this transducer layer should be close to $\lambda/4$.

To conclude, if there is a sufficiently large number of layers, the substrate may be made of any material and will not have any significant influence on the Q factor of the resonance and its electrical characteristics.

[1] J. Zelenka, *Piezoelectric Resonators and Their Applications* (Elsevier, New York, 1986; Mir, Moscow, 1990).
[2] L. M. Brekhovskikh, *Waves in Layered Media* (Academic Press, New York, 1960) [Russian original, USSR Academy of Sciences Press, Moscow, 1957].
[3] V. S. Veretin, A. G. Kozorezov, B. N. Krutov, and G. D. Mansfel'd, Radiotekh. Élektron. **37**, 401 (1992).
[4] G. S. Kino, *Acoustic Waves: Devices, Imaging, and Analog Signal Processing* (Prentice-Hall, Englewood Cliffs, N.J. 1987; Mir, Moscow, 1990).
[5] A. I. Morozov, V. V. Proklov, and B. A. Stankovskiĭ, *Piezoelectric Transducers for Radio Electronics Devices* [in Russian], Radio i Svyaz', Moscow (1981).

Translated by R. M. Durham
Edited by Steve Torstveit

Information-compressed structure of an edge laser speckle pattern

Yu. V. Vasil'ev, E. F. Kuritsyna, and A. E. Luk'yanov

M. V. Lomonosov State University, Moscow
(Submitted April 8, 1997)
Pis'ma Zh. Tekh. Fiz. **23**, 42–46 (October 12, 1997)

A correlation is established experimentally between the real ''faceted'' structure of the cutting area of a blade according to electron microscopy data and the spatial quantization of an image of the recorded speckle field (upon the maximum compression of the recorded information to logical zeroes and ones) in coherent optical analyses of the diffraction effect at the blade edge. This correlation may prove useful for solving the inverse technical problem (with equally justified variants of concepts for the theoretical modeling of a specific situation). © *1997 American Institute of Physics.* [S1063-7850(97)00810-0]

It is known[1] that when a Gaussian laser beam undergoes diffraction at the straight edge of a safety razor blade, a complex speckle structure is formed in the surrounding space, where the extremely anisomeric speckles are of major interest. These are attributable to micro-irregularities on the cutting area of the blade. The cutting area is at the end of a symmetric, wedge-shaped, tapered edge of a steel plate 80 μm thick, it has a length of 37 mm and an average width of around 300 nm, which is less than the wavelength of light. Thus very bright, monochromatic, continuous narrow parallel lines or bands — edge laser speckles — can be identified on a flat sheet of photographic paper mounted parallel and at a large distance L from a straight diffraction edge.

After the photographic paper has been developed, the speckles are seen by the observer as a negative image — as dark lines or bands on a white background. The one-dimensionality of the speckles simplifies a rapid analysis of the unknown micromorphology of the cutting area using the recorded information, on photographic paper for instance, thus allowing the information compression process to be specifically controlled.[2] Compression of information is a powerful and flexible tool in experimental studies of speckles and the microinhomogeneities generating them.

Here we aim to determine experimentally whether a recorded optical pattern has any law governing the relative distribution of edge laser speckles. If the answer is yes, the entire analysis is converted to the region of an iconic. At the first stage, it is advisable to confine our description to the simplest information-compressed structure formed by the edge laser speckles of an optical pattern. In familiar language, this means that we shall use methods of contrast black and white photography without the concept of halftones.

A positive answer to the question was obtained in experiments using a UIG-22M holographic measuring device. The investigations were made using an optical system shown schematically in Fig. 1. An LGN-503 argon laser *1* directly or via a focusing spherical lens *2* illuminates the cutting area of a blade *3* (the straight edge of the blade coincides with the z axis in the right-hand Cartesian coordinate system xyz). An edge laser speckle pattern is recorded on a narrow rectangular sheet of photographic paper in a photographic frame *4* (at a distance $L=1.5$ m along the x axis). The long side of the sheet is parallel to the z axis and the short side is parallel to the y axis. The laser beam ($\lambda=488$ nm wavelength, TEM_{00} spatial mode, electric vector of plane wave parallel to z axis, and effective beam diameter $D=2.5$ mm) propagates along the y axis and is incident perpendicularly on the beveled face of the tapered blade edge (width of face ~ 1 mm) in the plane $y=0$. The edge laser speckles are isolated from the complex speckle structure by mounting the frame *4* beyond this plane.

It was observed, using a JSM-U3 scanning electron microscope, that the cutting area of the blade is divided into numerous plane microfaces which randomly vary the angle of incidence with respect to the z axis. Their length also varies randomly between values of the order of one and tens of wavelengths of light. Each microface may be considered as an independent scatterer of incident coherent radiation. Thus, Fraunhofer speckles are recorded objectively in an optical experiment.[3]

When the cutting area of the blade is illuminated by a direct laser beam, it is established that the width of the edge laser speckles is of the same order of magnitude as the diffraction-theory estimate of the speckles:[3] $\Delta z \sim \lambda L/D$. When a lens is installed[2] (the rear focal plane coincides with the $y=0$ plane), the cross section of the Gaussian beam is compressed and the speckles become broader and brighter. After the contrast photographic paper has been exposed, alternate black and white bands of different width can be identified (Fig. 2).

The black bands correspond to the point where predomi-

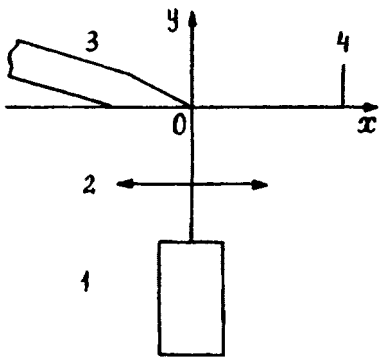

FIG. 1. Schematic diagram of experiment.

 1063-7850/97/100753-02$10.00 © 1997 American Institute of Physics

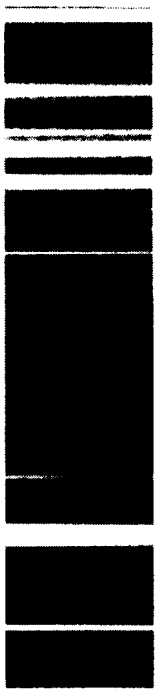

FIG. 2. Typical example of the simplest information-compressed structure of an edge laser speckle pattern (in the far field when the cutting area of the blade is illuminated by a small aperture focused Gaussian argon laser beam).

nantly cophasal scattered waves are incident from the microfaces of the blade. Amplitude summation of the cophasal waves leads to exaggerated values of the illuminance. The white bands correspond to points of reduced illuminance where the antiphase scattered waves cancel each other. For a concise description of the information-compressed structure of the initial optical pattern, the black bands can be arbitrarily called speckles and the white bands — antispeckles (in the sense of the accompanying physical phenomena).

Experience shows that the width of the speckles and antispeckles is a multiple of some value B. On photographic paper (Fig. 2), for instance $B \sim 1$ mm and thus these speckles can easily be perceived visually by selecting a lens with the required focal length. The observed multiplicity of the widths indicates that the recorded image is spatially quantized in terms of the z coordinate. Along this coordinate the speckles and antispeckles are essentially wave packets. The speckles are rectangular wave packets corresponding to the recorded (real) states of the optical field and the antispeckles are packets of undetermined internal structure corresponding to the nonrecorded (visual) states of the optical field. In the experiments the speckles in the initial pattern have a level of illuminance above the recording threshold established experimentally from the specific conditions of the particular technical problem.

The interpretation of an information-compressed structure in terms of wave packets is useful for solving the inverse problem — finding the characteristics of the cutting area from the recorded radiation scattering. The situation may be analyzed by a completely equivalent method in terms of the optical degrees of freedom of the images using either well-known spectral concepts or geometric optics. The first case uses the concept of Gabor information bands in the spatial spectrum of the scattered radiation, while the second is based on Kotel'nikov information wave packets. Essentially the analysis takes into account the principal lobe of the angular distribution of the subsystem radiation which consists of identically spatially oriented microfaces of the cutting area forming a complex re-emitter. The azimuthal angle of the principal lobe of the various subsystems forming the illuminated section of the edge should correspond to the directions determined by the measurement points of the Kotel'nikov theorem. The choice of one of these concepts to solve a specific technical problem is dictated only by practical suitability.[2]

[1] Yu. V. Vasil'ev and A. E. Luk'yanov, Zh. Tekh. Fiz. **64**(8), 168 (1994) [Tech. Phys. **39**, 838 (1994)].
[2] A. A. Kharkevich, *Spectra and Analysis* [in Russian], Fizmatgiz, Moscow (1962)
[3] M. Françon, *Laser Speckle and Applications in Optics* (Academic Press, New York, 1979; Mir, Moscow, 1980).

Translated by R. M. Durham
Edited by Steve Torstveit

Probing of a random phase screen by a focused spatially modulated laser beam. Diffraction at a large number of inhomogeneities

V. P. Ryabukho and A. A. Chausskiĭ

Saratov State University;
Institute of Problems in Precision Mechanics and Control, Russian Academy of Sciences, Saratov
(Submitted April 2, 1997)
Pis'ma Zh. Tekh. Fiz. **23**, 47–53 (October 12, 1997)

The contrast of the Young's interference fringes formed in the diffraction field when a dynamic random phase screen is illuminated by a focused, spatially modulated laser beam is obtained analytically as a function of the statistical parameters of the screen. A threshold relative bleaching effect is established for a highly dispersive medium when a low-divergence illuminating beam is used. © *1997 American Institute of Physics.* [S1063-7850(97)00910-5]

When a random phase screen is probed by a broad laser beam with interference fringes — a spatially modulated laser beam — Young's fringes are formed in the diffraction field whose contrast evolves in the longitudinal direction as a function of the statistical parameters of the screen.[1] When a focused, spatially modulated laser beam is used, Young's fringes are only observed when using an inertial photodetector with a moving random phase screen.[2] Our aim in the present paper is to determine the analytical dependence of the contrast of these fringes on the statistical parameters of the random phase screen.

If a spatially modulated laser beam with parallel interference fringes is used,[2] two spatially separated laser spots are formed in its focal zone (Fig. 1). The relation between the diameters d of these spots and the inhomogeneity correlation length l_ϕ strongly influences the contrast of the fringes observed in the diffraction field for a moving screen. Three typical cases must be distinguished: diffraction by a large number of inhomogeneities ($d \gg l_\phi$), diffraction by a small number of inhomogeneities ($d \approx l_\phi$), and deflection of the interference fringes ($d < l_\phi$). Here we consider the quantitative relation between the contrast of Young's interference fringes and the statistical parameters of a random phase screen for diffraction by a large number of inhomogeneities in the screen ($d \gg l_\phi$).

When a diffraction-limited objective is used with an aperture diameter D greater than the period Λ_0 of the fringes, the diameter $d \approx 2\lambda f/D$ of the spots on the surface of a random phase screen is smaller than the distance between their centers $\rho_0 = \lambda f/\Lambda_0$. Thus, two nonidentical (uncorrelated in terms of fluctuational components), partially developed speckle fields form in the scattered radiation, and their interference leads to the formation of fringes with the period $\Lambda_z = \lambda z/\rho_0$ within individual speckles with dimensions $\varepsilon_\perp \approx \lambda z/d$. Transverse motion of the random phase screen is accompanied by speckle dynamics and by the formation of Young's fringes with the same period Λ_z but whose contrast V is lower than the contrast V_0 without the screen.[2] The contrast of the Young's fringes formed by the interference of uncorrelated, partially developed speckle fields is determined by the relation between the intensities of the unscattered field components $\overline{I_1}$ and $\overline{I_2}$, and the average intensities of the fluctuation components $\langle \tilde{I}_1 \rangle$ and $\langle \tilde{I}_2 \rangle$, and may be written as follows:[3]

$$V = V_0 \frac{\overline{I_1}}{\langle \tilde{I}_1 \rangle + \overline{I_1}} = V_0 \frac{\overline{I_2}}{\langle \tilde{I}_2 \rangle + \overline{I_2}}. \tag{1}$$

Thus the problem of determining the dependence of V on the statistical parameters of a random phase screen reduces to finding the intensities $\langle I_1 \rangle = \langle \tilde{I}_1 \rangle + \overline{I_1}$ as functions of these parameters.

In the approximation of Fresnel diffraction and a Gaussian illuminating laser beam, the average intensity of the diffraction field should be written as[4,5]

$$\langle I_1(\boldsymbol{\zeta}, z) \rangle \cong \int_{-\infty}^{\infty}\int \int_{-\infty}^{\infty}\int \exp\left(-\frac{\Delta\boldsymbol{\rho}^2}{2w_0^2}\right) \times \exp\left(-\frac{2\mathbf{R}^2}{w_0^2}\right) \mu_t(\Delta\boldsymbol{\rho}) \exp\left[\frac{ik}{z}\mathbf{R}\cdot\Delta\boldsymbol{\rho}\right] \times \exp\left[-\frac{ik}{z}\Delta\boldsymbol{\rho}\cdot\boldsymbol{\zeta}\right] d^2\mathbf{R}\, d^2\Delta\boldsymbol{\rho}, \tag{2}$$

where w_0 is the radius of the waist of the focused Gaussian beam, $\Delta\boldsymbol{\rho} = \boldsymbol{\rho}_1 - \boldsymbol{\rho}_2$, $\mathbf{R} = (\boldsymbol{\rho}_1 + \boldsymbol{\rho}_2)/2$, $\boldsymbol{\rho}_1$ and $\boldsymbol{\rho}_2$ are the coordinates in the plane of the random phase screen (Fig. 1), $\mu_t(\Delta\boldsymbol{\rho})$ is the correlation coefficient of the complex transmission of the screen $t(\boldsymbol{\rho}) = \exp(-i\varphi(\boldsymbol{\rho}))$, and $\varphi(\boldsymbol{\rho})$ is a ran-

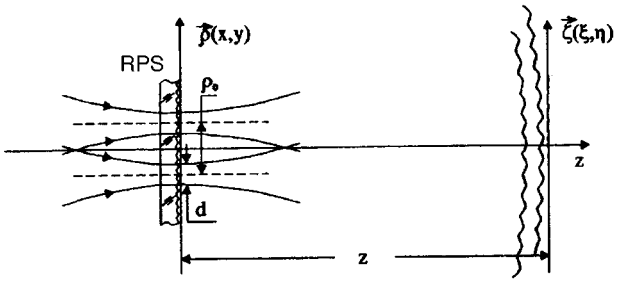

FIG. 1. Diffraction of a focused spatially modulated laser beam by many scattering centers.

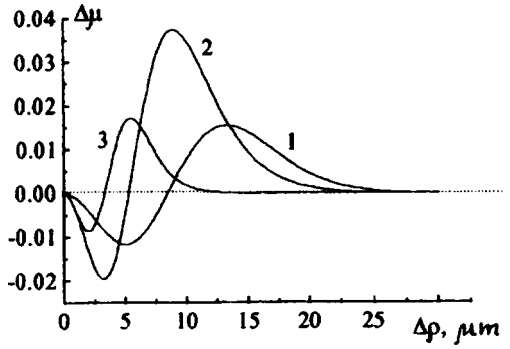

FIG. 2. Difference between the correlation coefficients of the complex transmission of a random phase screen determined using formulas (3) and (4) for various values of σ_ϕ: *1* — $\sigma_\phi=1$; *2* — $\sigma_\phi=2$; *3* — $\sigma_\phi=\pi$; $l_\phi=10$ μm.

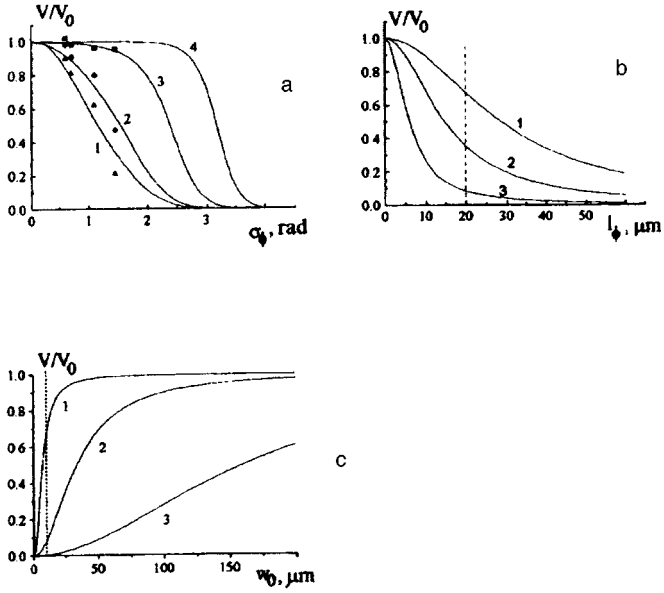

FIG. 3. Experimental data and theoretical curves of the relative contrast of the Young's fringes as a function of the statistical parameters of the random phase screen σ_ϕ, I_ϕ, and constriction radius w_0 of the illuminating Gaussian beam on the surface of the screen: a — *1* — $w_0=6.3$ μm; *2* — $w_0=11$ μm; *3* — $w_0=40$ μm; *4* — $w_0=200$ μm; $l_\phi=7.5$ μm. b — *1* — $w_0=40$ μm; *2* — $w_0=80$ μm; *3* — $w_0=160$ μm; $\sigma_\phi=2.5$. c — *1* — $\sigma_\phi=1.5$; *2* — $\sigma_\phi=2.5$; *3* — $\sigma_\phi=\pi$; $l_\phi=5$ μm.

dom phase function of the coordinates. For normally distributed φ the coefficient μ_t may be written as[4,5]

$$\mu_t(\Delta\boldsymbol{\rho})=\exp\{-\sigma_\phi^2[1-K_{\varphi(\Delta\boldsymbol{\rho})}]\}, \tag{3}$$

where σ_ϕ^2 and K_ϕ^2 are the variance and correlation coefficient of the spatial phase fluctuations $\varphi(\boldsymbol{\rho})$. In order to integrate expression (2), we need to transform $\mu_t(\Delta\boldsymbol{\rho})$ to a simpler form. This can be achieved for a Gaussian profile $K_\phi(\Delta\boldsymbol{\rho})=\exp(-\Delta\boldsymbol{\rho}^2/l_\phi^2)$, writing $\mu_t(\Delta\boldsymbol{\rho})$ as follows:

$$\mu_t(\Delta\boldsymbol{\rho})=[1-\exp(-\sigma_\phi^2)]\exp\left(-\frac{\Delta\boldsymbol{\rho}^2}{\rho_\perp^2}\right)+\exp(-\sigma_\phi^2), \tag{4}$$

where

$$\rho_\perp=l_\phi\left[-\ln\left\{\frac{1}{\sigma_\phi^2}\ln\left[\frac{\exp(+\sigma_\phi^2-1)}{\exp(+1)}+1\right]\right\}\right]^{1/2} \tag{5}$$

is the correlation length of the fluctuation component of the boundary field. The differences between the values of $\mu_t(\Delta\boldsymbol{\rho})$ calculated using formulas (3) and (4) do not exceed 0.04 (Fig. 2). Thus, expression (4) may be considered to be a good approximation for μ_t. Using expression (4) and Fourier transforming the Gaussian functions in Eq. (2) with respect to the variables $\mathbf{R}$ and $\Delta\boldsymbol{\rho}$, we obtain an analytical expression with an explicit physical meaning for the normalized average intensity of the diffraction field:

$$\begin{aligned}\langle I(\boldsymbol{\zeta}z)\rangle\cong&\exp(-\sigma_\phi^2)\frac{w_0^2}{w^2(z)}\\&\times\exp\left(-\frac{2\boldsymbol{\zeta}^2}{w^2(z)}\right)+[1-\exp(-\sigma_\phi^2)]\\&\times\frac{w_0^2}{w^2(z)+2(\lambda z/\pi\rho_\perp)^2}\\&\times\exp\left(-\frac{2\boldsymbol{\zeta}^2}{w^2(z)+2(\lambda z/\pi\rho_\perp)^2}\right),\end{aligned} \tag{6}$$

where $w(z)=w_0(1+\lambda^2z^2/\pi^2w_0^4)^{1/2}$ is the radius of the unscattered Gaussian beam in the plane of observation. The first term in expression (6) is the intensity distribution of the unscattered component, and the second term is the average intensity of the fluctuation component of the field.

Using expressions (1) and (6), we can easily write the complete form of the expression for the contrast of the Young's fringes in the plane of observation. This expression is simplified for $z\gg z_0$, where $w(z)\cong\lambda z/\pi w_0$, and with the assumed condition $(2w_0)^2=(d)^2\gg(l_\phi)^2$, and therefore $(2w_0)^2\gg(\rho_\perp)^2$, it is written for the paraxial region ($\boldsymbol{\zeta}\approx0$)

$$V(\sigma_\phi,l_\phi,w_0)=V_0\left\{1+\frac{1-\exp(-\sigma_\phi^2)}{\exp(-\sigma_\phi^2)}\,\frac{\rho_\perp^2}{2w_0^2}\right\}^{-1}. \tag{7}$$

Figure 3 gives experimental data (Fig. 3a) and theoretical curves of the relative contrast V/V_0 calculated using Eq. (7) plotted as a function of the statistical parameters of the random phase screen σ_ϕ and l_ϕ, and the waist radius w_0 of the illuminating Gaussian beam. We draw attention to the threshold behavior of the fringe contrast for comparatively large σ_ϕ and small l_ϕ when the illuminated region has a fairly large diameter $2w_0$ and the divergence of the illuminating beam is therefore low (Fig. 3a, curves *3* and *4*). The small variation in the contrast of the fringes in the region of small σ_ϕ is caused by competition between two processes — a decrease in the intensity of the unscattered component $\overline{I_1}$ and a reduction in the average intensity of the fluctuation component $\langle\tilde{I}_1\rangle$ caused by a decrease in the correlation length of the boundary field $\rho_\perp$ with increasing σ_ϕ (see Eq. (5)). Formula (7) may be further simplified by using the approximation $\rho_\perp\approx l_\phi/\sigma_\phi$, which is follows from Eq. (5) for $\sigma_\phi\geqslant1$.

The observed threshold effect of relative bleaching of a highly dispersive object may be utilized in the diagnostics of biological media[6] and to monitor comparatively coarse rough surfaces.

For light diffraction at a large number of inhomogeneities in a screen it is sufficient that the condition $(2w_0)^2 \geqslant 10l_\phi^2$ hold.[7] The vertical dashed lines in Fig. 3 indicate the arbitrary limits of validity of these dependences. For $2w_0 < l_\phi$ the speckle modulation disappears in the diffraction field and deflection of the interference fringes is observed for the moving screen. This leads to qualitative changes in the dependence of the contrast of the Young's fringes on the screen parameters σ_ϕ and l_ϕ which must be taken into account when a focused, spatially modulated laser beam is used for the diagnostics of random phase objects.

[1] V. P. Ryabukho, Yu. A. Avetisyan, and A. B. Sumanova, Opt. Spektrosk. **79**, 299 (1995) [Opt. Spectrosc. J. **79**, 275 (1995)].

[2] V. P. Ryabukho and A. A. Chausskiĭ, Pis'ma Zh. Tekh. Fiz. **21**(16), 57 (1995) [Tech. Phys. Lett. **21**, 658 (1995)].

[3] V. P. Ryabukho, Opt. Spektrosk. **78**, 970 (1995) [Opt. Spectrosc. J. **78**, 878 (1995)].

[4] S. M. Rytov, Yu. A. Kravtsov, and B. I. Tatarskiĭ, *Introduction to Statistical Radiophysics. Part 2, Random Fields* [in Russian], Nauka, Moscow (1978).

[5] J. W. Goodman, *Statistical Optics* (Wiley, New York, 1985; Mir, Moscow, 1988).

[6] V. V. Tuchin, I. L. Maksimova, D. A. Zimnyakov, I. L. Kon, A. Kh. Mavlutov, and A. A. Mishin, Proc. SPIE **2925**, 118 (1996).

[7] E. Jakeman, Opt. Eng. **23**, 453 (1984).

Translated by R. M. Durham

Edited by Steve Torstveit

Propagation characteristics of the dynamic state in a capillary discharge jet

S. E. Emelin, A. L. Pirozerskiĭ, V. S. Semenov, and G. E. Skvortsov

Scientific-Research Institute of Physics, St. Petersburg State University
(Submitted May 12, 1997)
Pis'ma Zh. Tekh. Fiz. **23**, 54–59 (October 12, 1997)

A study is made of the so-called dynamic state of a metastable substance, characterized by the onset of a nonequilibrium energy interaction (interchange), involving various waves, in the excited material. The intensity of the optical emission is used to analyze the dynamic state; an investigation is made of the propagation of its leading and trailing edges. Various propagation characteristics and natural solitary-wave forms are identified; their similarity to ionization waves allows making some assumptions about the essential nature of this process. The observed effects are important for establishing the physical conditions for the formation of the substance of ball lightning and are also interesting for the physics of flames, electrical breakdown, and electrode spots. © *1997 American Institute of Physics.*
[S1063-7850(97)01010-0]

It was shown in Ref. 1 that in the metastable substance of a capillary discharge jet there forms a dynamic state induced by the action of the plasma generator and propagating along the jet at appreciable velocity. The velocity near the exit aperture of the spark gap was estimated from the delay of the characteristic perturbations of the time dependence of the signal from the probing microwave apparatus. In that study the source of the perturbations was jumps in the parameters as a result of low-frequency nonlinear oscillations of the current. For studying the parts of the jet at some distance from the spark gap the method used in Refs. 1 and 2 had to be modified, since, outside the region of high export currents the perturbations created by the current oscillations are small, propagation of the jet through the waveguide aperture is accompanied by additional perturbations, and the large dimensions of the waveguide make for low spatial resolution. Thus, in the present study we used the leading edges of the current pulse as sources of strong perturbations, and the state of the excited material and its dynamics were analyzed using the time dependence of the radiation intensity in the 0.3–1-μm range, as in Refs. 3–5. The propagation characteristics were determined by comparing synchronized oscilloscope traces of the signals from two detectors separated by a distance of 15 mm along the jet (see Figs. 1a–1f).

The erosion generator incorporated a polyethylene spark gap with a channel of length $l_c=20$ mm and diameter $d_c=1.8-2.0$ mm, a copper end electrode of diameter $d_c=1.4$ mm, a choke coil $L=0.5$ mH, a limiting resistance $R=200\ \Omega$, and a storage device $C=0.2$ mF. The time constant of the circuit was $\tau_{sch}=L/R=2.5\ \mu$s. The initial voltage of the storage device was $U_s=1.3-1.6$ kV and the current cutoff voltage was $U_e\sim 1.25$ kV.

The signals from the measuring apparatus had a delay caused, not only by the time taken for the leading edge of the state to reach the detectors, but also by the time taken to establish the dynamic regime. In order to study the stages of the transition process, we carried out an additional experiment in which the discharge was forcibly terminated at a particular time by shorting the electrodes of the spark gap using a programmed mechanical device. Oscilloscope traces were recorded for the radiation detector signal from the channel and the discharge current and voltage, and a series (sweep) of signatures of the moving and transforming electrode spots was recorded on copper foil, as in Ref. 2. By comparing these data, we determined a range of parameters, including the optical radiation intensity and its decay time constant after the switching off of the current, the diameter and resistivity of the discharge volume, and so on, and we made an analysis of the core formation process. We found experimentally that during the establishment process, beginning with expansion of the discharge and lasting between a few tenths and a few milliseconds ($d_c=1.4-5.0$ mm), the decay time constant of the radiation increases by approximately two orders of magnitude and then varies negligibly. The radiation intensity and the resistivity of the discharge volume behave similarly.

As the leading edge of the dynamic state propagates, the signals from the electrical probe and the radiation detector positioned side by side appear simultaneously. When the length of the luminous part of the jet at the end of the pulse was $\sim$10–15 cm, the velocity of the leading edge of the radiation, determined 55 mm from the spark gap according to the delay of the signal from the second detector relative to the first (see Figs. 1a and 1b), was $V_1\sim 15$ m/s. This velocity decreases with increasing channel diameter and is clearly close to the velocity of the material. The beginning of the luminous part of the jet (10–15 mm) consists of a bright frontal section and a rear section of continuously decreasing brightness. The presence of a steep leading edge adjacent to an abrupt radiation peak indicates a buildup of excitations, whose flux propagates more rapidly than the material away from the generator and is reflected from the boundary of a plasma-like state. It also indicates that the displacement of this boundary resembles a leader.

As the initial voltage U_s increases to 1.5 kV, an increase in the radiation intensity is observed during the pulse (see Fig. 1c) and after the jet has reached approximately half of the maximum length, an intensity dip followed by a rise is formed beyond the leader. Some 15 mm before the second detector, a new delayed and modified leader is formed and

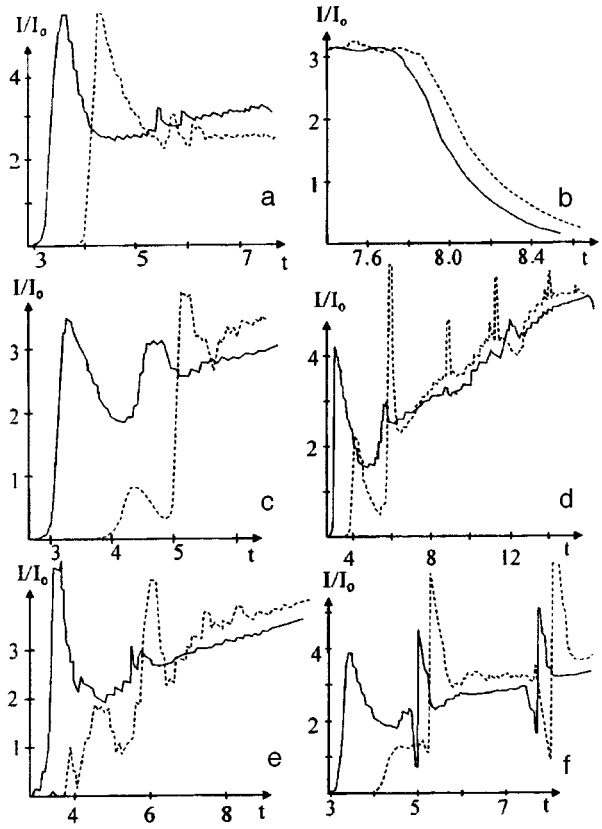

FIG. 1. Radiation intensity in the range 0.3–1 μm (in arbitrary units) as a function of time (in ms) at distances of 47.5 mm (solid curves) and 62.5 mm (dashed curves) from the spark gap. The initial voltage of the storage device is $U_s = 1.35$ kV (a, b), $U_s = 1.5$ kV (c), and $U_s = 1.6$ kV (d–f).

the old one dissipates because of the lost energy supply. Thus, the propagation of a conducting, plasma-like state is a stepwise process.[6] Similar effects at some distance from the leading edge give radiation intensity amplification peaks an order of magnitude shorter (see Fig. 1d), which may go beyond the leading edge (see Fig. 1e). Some of these exhibit a decrease in the radiation in front of the peak — a shadow region (see Fig. 1f). In our view, this indicates that isolated excitations and fragments of excited material are entrained by solitary waves and form energetically denser objects which absorb radiation, propagate at a velocity several times higher, and are capable of sustaining their state independently for some time.

The concluding stage of the discharge is characterized by abrupt termination of current through the spark gap and relaxation of the plasma-like state of the metastable substance. The decay time constant differed substantially for different parameters. The electrical potential of the jet exhibits the fastest relaxation (the rise time of the potential variation in Ref. 1 was less than 30 ns), followed by the microwave reflection (less than 10 μs in the absence of additional perturbations such as acoustic ones), and the optical radiation (more than 0.3 ms, see Fig. 1b).

The delay in the onset of relaxation of the radiation (see Fig. 1b) increases with distance from the spark gap and the trailing edge velocity V_2 of the dynamic state determined from this decreases from 150 m/s at 55 mm from the spark gap to 40 m/s at 10 mm from the leading edge of the leader.

These experimental results confirm that a particular state, described as dynamic in Ref. 1, is established in the metastable substance of a capillary discharge jet. Under some conditions, this leads to appreciable lengthening of the luminous part of the jet, removal of current and the formation of a core, and the appearance of various external indications of an excited condensed state, such as stability of shape and the capacity to release energy in a metal, disintegrating on impact with a target. This state induced by a plasma generator is only observed in mobile forms and thus, having a wave nature, is associated with the establishment of conditions for the existence of various types of slowly decaying waves. Their intense excitation activates transport phenomena, establishing in the metastable substance a nonequilibrium energy interchange having a preferred direction of energy flux, viz., away from the generator. The natural forms of the dynamic state observed as solitary waves under these conditions move away from the generator at a velocity several times higher than the velocity of the material but considerably lower than the velocity of sound. They are similar to ionization waves but exist against a background of energy accumulation effects typical of a metastable material formed by a metal or polymer destroyed under highly nonequilibrium conditions. Their behavior makes them similar to autowaves in active media, so that in Ref. 7 they were called excitation waves. The nonlinear effects which accompany their propagation and are responsible for the conversion of structural–energy states can lead to wave self-focusing, which may explain the concentric structure of the jet.[2]

[1] S. E. Emelin *et al.*, Pis'ma Zh. Tekh. Fiz. **22**(24), 21 (1996) [Tech. Phys. Lett. **22**, 1005 (1996)].
[2] S. E. Emelin, V. S. Semenov *et al.*, in *Ball Lightning in the Laboratory* [in Russian], Khimiya, Moscow (1994), pp. 87–95.
[3] V. V. Kropochev, E. A. Manykin, *et al.*, *ibid.*, pp. 211–217.
[4] R. F. Avramenko *et al.*, *Studies of Electrical Discharges in the Atmosphere* [in Russian], Yaroslavl State University Press, Yaroslavl (1991), pp. 74–84.
[5] L. A. Tummerman and B. A. Chayanov, in *Research in Experimental and Theoretical Physics* [in Russian], Academy of Sciences of the USSR Press, Moscow (1959), pp. 231–243.
[6] Yu. P. Raizer, *Physics of Gas Discharges* [in Russian], Nauka, Moscow (1992).
[7] S. E. Emelin, V. S. Semenov, V. L. Bychkov *et al.*, Zh. Tekh. Fiz. **67**(3), 19 (1997) [Tech. Phys. **42**, 269 1997)].

Translated by R. M. Durham
Edited by Steve Torstveit

Breakup of a highly charged bubble in a dielectric liquid into parts of comparable size

A. I. Grigor'ev, V. A. Koromyslov, and A. N. Zharov

Yaroslavl State University
(Submitted May 20, 1997)
Pis'ma Zh. Tekh. Fiz. **23**, 60–65 (October 12, 1997)

An analysis is made of the conditions for instability of a charged gas bubble in a dielectric liquid. It is shown that unlike a charged droplet, the criterion for instability of a bubble is determined by two dimensionless parameters: the Rayleigh parameter and the ratio of the gas pressure in the parent bubble to the Laplace pressure. © *1997 American Institute of Physics.*
[S1063-7850(97)01110-5]

The breakup of charged bubbles in a dielectric liquid is a phenomenon of interest for various branches of technical physics and chemical technology, and particularly for the theory of breakdown of liquid dielectrics. It has been established experimentally that charged bubbles may break up into several small bubbles as a result of instability with respect to the surface charge.[1] Nevertheless, as yet there has been no adequate theoretical explanation for the experimental results, even though a fairly comprehensive theory has been developed for the mechanism driving the evolution of a qualitatively similar instability of highly charged liquid droplets (see the review presented in Ref. 2).

1. We consider a spherical charged bubble in a nonconducting incompressible liquid having permittivity ε, occupying an infinite volume, and having a uniform temperature T throughout. We assume that R is the bubble radius, Q is the charge, σ is the surface tension of the liquid–gas interface, and p is the gas pressure in the bubble. We pose the question: At what bubble radius will the potential energy have a minimum for Q = const? To answer this question, we write the expression for the potential energy of the bubble

$$U=4\pi R^2\sigma+\frac{Q^2}{2R}+p\frac{4\pi}{3}R^3,$$

and we equate to zero the derivative $\partial U/\partial R$:

$$\frac{\partial U}{\partial R}=8\pi R\sigma-\frac{Q^2}{2R^2}+4\pi R^2 p=0.$$

It is then easy to see that the minimum potential energy of the bubble corresponds to the state where

$$W=1-\beta, \tag{1}$$

where

$$W=\frac{Q^2}{16\pi R^3\sigma}, \quad \beta=\frac{Rp}{2\sigma}.$$

2. We now pose the question: For what values of the parameters W and β may the spherical shape of the bubble become unstable? By analogy with a charged droplet of incompressible liquid, this question may be answered by analyzing the pressure balance at the bubble surface:

$$p+\frac{Q^2}{8\pi R^4}-\frac{2\sigma}{R}=0.$$

Dividing this relation by the last term, we obtain relation (1). We can talk of instability of the bubble when the sum of the gas pressure and the electric pressure exceeds the Laplace pressure, i.e., when

$$W+\beta\geqslant 1. \tag{2}$$

Relations (1) and (2) differ from those for a spherical charged droplet[2] in that they contain the parameter β. However, it should be borne in mind that, because of the incompressibility, satisfaction of the instability criterion for a charged droplet of incompressible liquid, $W\geqslant 1$ (Ref. 2), implies that the spherical shape of the droplet should become unstable relative to the dominant mode of the capillary oscillations ($n=2$), i.e., the droplet is pulled into a spheroid. For the particular case of a bubble in a liquid, fulfillment of condition (2) primarily implies that the bubble radius may begin to change, i.e., instability of the $n=0$ mode or instability of the bubble relative to radial oscillations. This process may be accompanied by loss of stability in relation to dissolution of the gas (evaporation or condensation of the vapor) in the liquid. Note that for a droplet of incompressible liquid the dominant mode is $n=2$, and $n=0$ radial oscillations are impossible because of the constant volume of the droplet.[3] These two instabilities have different characteristic growth times. It seems that for W close to unity, the growth rate of the hydrodynamic mode ($n=2$), corresponding to a change in the shape of the droplet, exceeds the growth rate of the $n=0$ mode associated with the characteristic diffusion time of the gas molecules or vapor. Under these conditions, the bubble will be elongated to form a spheroid and will break up into parts as its eccentricity increases.

Depending on the relation between the relaxation time of the electric charge at the surface of the bubble and the characteristic growth time of the instability, it is possible to identify a limiting bubble breakup regime in which the relaxation time of the electric charge is much greater than the instability growth time. In this case, the charge may be considered to be frozen into the surface of the bubble. We shall analyze the laws governing breakup of a bubble for this particular case.

3. Let us assume that an initially spherical bubble, for which condition (2) is satisfied, becomes unstable and is pulled into a figure similar to a spheroid, whose elongation leads to the growth of the necking (sausage) instability along the plane of symmetry perpendicular to the axis of symmetry and results in the formation of two, equal-volume, symmetri-

cally positioned bubbles, having the same charges and connected by a neck. This process produces two bubbles of equal radii $r_1=r_2\equiv r$ and charge $q_1=q_2\equiv q$, which are then compressed, decreasing in volume under the action of Laplace forces, which are greater for the daughter bubbles than for the parent ones. Since the bubbles undergo compression at constant liquid temperature (on assumption that the specific heat of an infinite volume is infinite), the compression process will be considered to be isothermal. In that case, work leading to an increase in the potential energy of the bubbles will be done on the gas in the bubbles.

The total change in the potential energy is determined by

$$\Delta U=4\pi\sigma(2r^2-R^2)+\frac{q^2}{\epsilon r}-\frac{Q^2}{2\epsilon R}-\frac{8}{3}\pi r^3 p_* in\left(\frac{2r^3}{R^3}\right),$$

where p_* is the gas pressure in the daughter bubbles after compression. The first term in this expression gives the change in the surface energy of the Laplace forces, the second gives the change in the electrical energy, and the third describes the work of isothermal compression of the daughter bubbles.

We shall assume that the pressure in the bubble is made up of the pressure of the included gas and the saturated vapor pressure of the liquid at a given temperature. Neglecting condensation and evaporation of the gas in the bubbles, we assume that its mass in the initial and final bubbles remains constant. We express the mass of gas in the parent and daughter bubbles, m and m_*, respectively, from the Mendeleev–Clapeyron equation:

$$m=\frac{4\pi}{3}R^3\frac{\mu p_g}{R_g T},\quad m_*=\frac{4\pi}{3}r^3\frac{\mu p_g^*}{R_g T},$$

where μ is the molar mass of the gas, R_g is the gas constant, and p_g and p_{g*} are the gas pressure in the parent and daughter bubbles, respectively. The equation of conservation of mass can then be used to find the gas pressure in the daughter bubbles: $p_{g*}=p_g R^3/(2r^3)$. The saturated vapor pressure in the daughter and parent bubbles can then be considered to be the same because it does not depend on the bubble volumes. Thus, the total pressure in the daughter bubble may be written as: $p_*=p_{g*}+p_s$, where p_s is the saturated vapor pressure in the parent bubble. Alternatively, defining the total pressure p in the parent bubble, we obtain

$$p_*=p_{g*}-p_g+p=p\left(\gamma\left[\frac{R^3}{2r^3}-1\right]+1\right),$$

where $\gamma=p_g/p$. Thus, if $\gamma=1$, the bubble must be considered to be gas and if $\gamma=0$, it only contains saturated vapor.

The condition for stability of the daughter bubbles may be obtained by equating to zero the first derivative of the change in the potential energy over the radius of the daughter bubble for $q=$ const. Using the expression for the gas pressure this condition is written as

$$\frac{2\sigma}{r}-p\left(\gamma\left[\frac{R^3}{2r^3}-1\right]+1\right)-\frac{q^2}{8\pi\varepsilon r^4}=0.$$

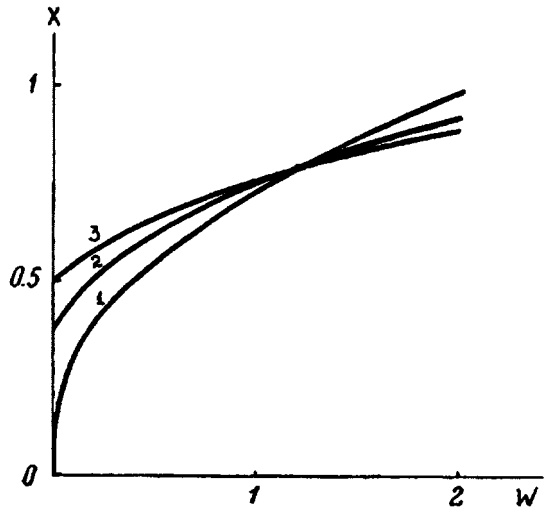

FIG. 1. Dimensionless radius X of daughter bubbles as a function of the dimensionless Rayleigh parameter W for $\beta=0.5$: *1* — $\gamma=0$; *2* — $\gamma=0.5$; *3* — $\gamma=1$.

Assuming that the charge of the daughter bubble is half the charge of the initial bubble and dividing the entire equation by the first term, we obtain an equation determining the dimensionless radius $X=r/R$ of the stable daughter bubble:

$$4X^3-\beta\gamma(2X-4X^4)-4X^4\beta-W=0. \tag{3}$$

Calculations using Eq. (3) show that as the Rayleigh parameter W for the parent bubble increases for $\beta=$const, the dimensions of the daughter bubbles also increase. Figure 1 gives the dimensionless bubble radius as a function of the Rayleigh parameter. It can be seen from the curves that the presence of gas in the bubble substantially influences the dimensions of the daughter bubbles, increasing them for $W\leqslant 1.2$ and decreasing them for $W\geqslant 1.2$.

Figure 2 gives the dimensionless radius of the daughter droplets as a function of the Rayleigh parameter W, as in Fig. 1, but in this case the dependence is obtained for the critical value $W+\beta=1$. It can be seen that the daughter bubbles of

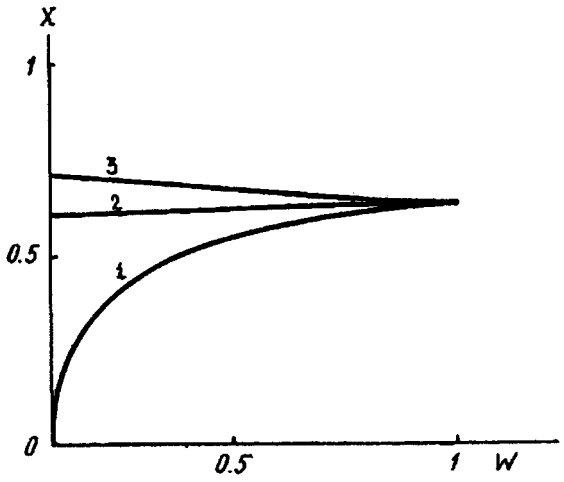

FIG. 2. The same dependence as in Fig. 1 calculated for $\beta=1-W$. Curve *1* corresponds to $\gamma=0$, curve *2* corresponds to $\gamma=0.5$, and curve *3* to $\gamma=1$.

a pure gas parent bubble decrease with increasing W and have a minimum for a vacuum bubble. The opposite situation is observed for a pure vapor bubble — the daughter bubbles increase with increasing W, even though the amount of vapor decreases.

To conclude, for an unstable bubble with small W the presence of saturated vapor in the bubbles will reduce the daughter bubbles as a result of condensation of the vapor whereas for large W it will lead to growth of these daughter bubbles as a result of evaporation.

[1] C. G. Garton and Z. Krasucki, Trans. Faraday Soc. **60**, 211 (1964).
[2] A. I. Grigor'ev and S. O. Shiryaeva, Izv. Ross. Akad. Nauk Ser. Mekh. Zhidk. Gaza No. 3, 3 (1994).
[3] L. D. Landau and E. M. Lifshitz, *Fluid Mechanics*, 2nd ed. (Pergamon Press, Oxford, 1987) [Russian original, 3rd ed., Nauka, Moscow, 1986].

Translated by R. M. Durham
Edited by Steve Torstveit

Wave number dependence of the critical conditions for instability of a charged liquid film in a fluctuational force field

D. F. Belonozhko, A. I. Grigor'ev, and M. I. Munichev

Yaroslavl State University
(Submitted May 20, 1997)
Pis'ma Zh. Tekh. Fiz. **23**, 66–70 (October 12, 1997)

It is shown that the critical conditions for instability of the charged free surface of a liquid film with a fixed thickness d in the region where the influence of fluctuational forces is substantial ($d<100$ nm) depend strongly on the wave number and do not depend on the viscosity of the liquid. © *1997 American Institute of Physics.* [S1063-7850(97)01210-X]

Studies of the stability of a thin film of conducting liquid on a solid substrate in a fluctuational force field (under the influence of the disjoining pressure[1,2]) are of interest for applications to problems in the operation of needle-type liquid-metal ion sources, vacuum mass spectrometry, and the theory of thunderstorm electricity.[3,4]

1. We shall calculate the spectrum of capillary waves at a flat charged surface of an ideally conducting liquid layer of thickness d, density ρ, viscosity ν, and surface tension γ, bounded by vacuum and situated in a gravitational field $\mathbf{g}$ and an electrostatic field $\mathbf{E}$. We assume that the upper medium has the permittivity ε. The electric field $\mathbf{E}$ at the surface of the liquid is determined by the potential difference between the electrodes, a lower electrode located at $z=-d$, covered with a layer of wetting liquid maintained at the potential $\Phi_1=0$, and a parallel counterelectrode positioned at the distance b from the liquid surface and having the potential $\Phi_2=V$.

Let us assume that in a Cartesian coordinate system with the z axis directed vertically upward $\mathbf{n}_z \| -\mathbf{g}$ (where $\mathbf{n}_z$ is the unit vector of the z Cartesian coordinate), the x axis determines the direction of motion of the plane capillary wave $\sim\exp(st+ikx)$, and the $z=0$ plane coincides with the free unperturbed surface of the liquid (s is the complex frequency, k is the wave number, t is the time, and $i=\sqrt{-1}$). Let us assume that the function $\xi(x,t)=\xi_0\exp(st+ikx)$ describes a small perturbation of an equilibrium flat liquid surface caused by thermal capillary wave motion of extremely small ($\xi_0\sim(kT/\gamma)^{1/2}$) amplitude, where k is Boltzmann's constant and T is the absolute temperature. The velocity field $\mathbf{U}(\mathbf{r},t)$ of the liquid motion caused by the perturbation $\xi(x,t)$ has the same order of smallness. Let us also assume that the thickness of the liquid layer is such that the influence of the fluctuational forces is important for its stability, i.e., $d<100$ nm (Refs. 1 and 2). Since it has been assumed that the liquid wets the substrate on which it lies, the fluctuational forces (the disjoining pressure acting on the layer from the substrate) play a stabilizing role.[1,2] For this qualitative analysis we assume, as in Ref. 2, that the disjoining pressure is related to the layer thickness by

$$P_d=\frac{A}{(d+\xi)^3}.$$

We only determine the order-of-magnitude value of the constant $A\simeq 10^{-13}$ erg. To linearize the problem, we need to use a linear expansion of P_a in terms of ξ near $z=0$:

$$P_d=P_{d0}+P_{d1};$$

$$P_{d0}=\frac{A}{d^3};\quad P_{d1}=-\frac{3A}{d^4}\xi.$$

By solving in a linear approximation for small quantities using the classical method of separating the velocity field into potential and vortex components based on the Helmholtz theorem, as in Ref. 5, we can easily obtain the dispersion relation for the spectrum of capillary motion of the liquid in this system. In dimensionless variables, where $\rho=\gamma=d=1$, and the physical parameters characterizing the system are measured in units of their characteristic scales

$$g_*=\frac{\gamma}{\rho d};\quad A_*=\gamma d;\quad \nu_*=\sqrt{\frac{\gamma d}{\rho}};\quad k_*=\frac{1}{d};$$

$$s_*=\sqrt{\frac{\rho d}{\gamma}};\quad W_*=\frac{\gamma}{d};\quad b_*=d,$$

the dispersion relation has the form

$$4qk^2(k^2+q^2)+(k^2+q^2)^2(k\ \sinh(k)\sinh(q) - q\ \cosh(k)\cosh(q))+4k^3q(q\ \sinh(k)\sinh(q) - k\ \cosh(k)\cosh(q))-\frac{Z(k,W)}{\nu^2}(q\ \cosh(q)\sinh(k) - k\ \cosh(k)\sinh(q))=0; \tag{1}$$

$$q^2\equiv k^2+a\nu;\quad Z(k,W)\equiv kg+3Ak+k^3-Wk^2\ \coth(kb).$$

2. The condition for the onset of instability of the charged free liquid surface is $Z(k,W)\leqslant 0$ (Refs. 6 and 7):

$$Z(k,W)\equiv kg+3Ak+k^3-Wk^2\ \coth(kb)<0.$$

The equation $Z(k,W)=0$ clearly determines the boundary between the stable ($Z(k,W)\geqslant 0$) and unstable ($Z(k,W)<0$) states of the system. Curves giving the stability boundary for various distances b from the upper electrode, with and without allowance for the disjoining pressure, are plotted in Figs. 1 and 2. It can be seen that at $\lambda<10d$, the critical conditions are almost independent of the fluctuational forces. The existence of disjoining pressure only significantly influences the critical conditions for instability of the free surface at wave-

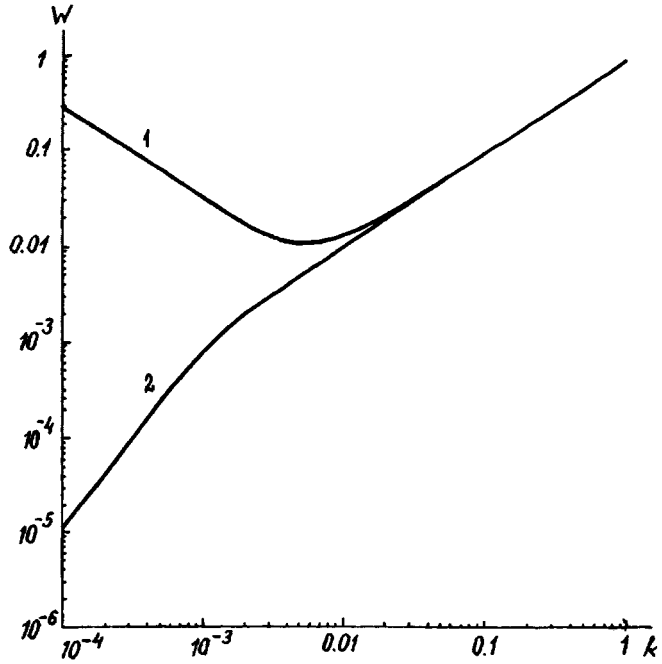

FIG. 1. Stability boundary of a charged free liquid surface: $Z(k,W)=0$, calculated for $b=10$. Curve *1* allows for fluctuational forces with $A=10^{-5}$, $g=10^{-9}$. Curve *2* neglects the influence of fluctuational forces.

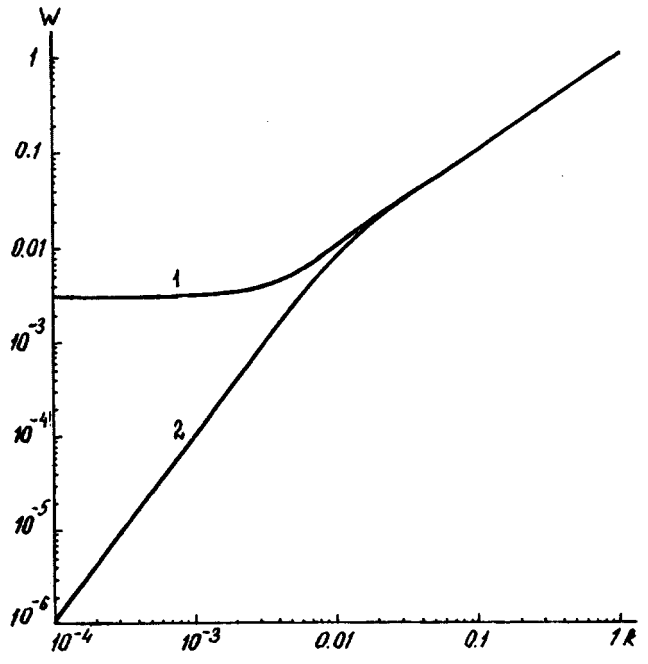

FIG. 2. Stability boundary of a charged free liquid surface: $Z(k,W)=0$, calculated for $b=100$. Curve *1* allows for fluctuational forces with $A=10^{-5}$, $g=10^{-9}$. Curve *2* neglects the influence of fluctuational forces.

lengths considerably greater than the thickness of the film, but in this case, as can be seen from the figures, the critical conditions depend strongly on the distance between the electrodes b. It is deduced from Figs. 1 and 2 that in these situations, the influence of fluctuational forces on the critical conditions for instability of a charged liquid surface should be investigated for wave numbers $k \lesssim 0.01$.

The figures show that allowance for the action of fluctuational forces reduces the wave number range of the unstable wavelengths on the high-k side by an amount determined by the parameter W. The fluctuational forces can ensure that the motion in the liquid film is stable for all k if $W<10^{-2}$ and the distance from the upper electrode is $b=10^5$ (Fig. 1), and also for $W<10^{-3}$ when $b=10^2$ (Fig. 2). Figure 1 shows that if $b=10^5$, then at least for $10^{-2}<W \leqslant 2\times10^{-2}$ the set of unstable wavelengths is bounded on the low-k side.

To conclude, for $b=10^2$ the influence of disjoining pressure is observed as a decrease in the critical value of k for which the motion in the system becomes unstable and the presence of a lower boundary on the range of variation of the parameter W for which unstable wavelengths can exist. For $b=10^5$ the latter effect is stronger, and it is also observed that the set of values of the unstable wavelengths k is bounded on the side of extremely low wave numbers.

[1] B. V. Deryagin, *Theory of Stability of Colloids and Thin Films* [in Russian], Nauka, Moscow (1986).
[2] J. Frenkel, *Kinetic Theory of Liquids* (Clarendon Press, Oxford, 1946) [Russian original, Nauka, Leningrad, 1945].
[3] M. D. Gabovich, Usp. Fiz. Nauk. **140**, 137 (1983) [Sov. Phys. Usp. **26**, 447 (1983)].
[4] M. D. Grigor'ev and S. O. Shiryaeva, Izv. Ross. Akad. Nauk Ser. Mekh. Zhidk. Gaza No. 3, 3 (1994).
[5] V. G. Levich, *Physicochemical Hydrodynamics* [in Russian], Fizmatgiz, Moscow (1959).
[6] L. D. Landau and E. M. Lifshitz, *Electrodynamics of Continuous Media*, 2nd ed. rev. and enlarged, with L. P. Pitaevskiĭ (Pergamon Press, Oxford, 1984) [cited Russian original, Nauka, Moscow, 1992].
[7] D. F. Belonozhko, A. I. Grigor'ev, M. I. Munichev, and S. O. Shiryaeva, Pis'ma Zh. Tekh. Fiz. **22**(10), 84 (1996) [Tech. Phys. Lett. **22**, 425 (1996)].

Translated by R. M. Durham
Edited by Steve Torstveit

Characteristics of a submicrosecond transverse discharge in mixtures of helium with N_2 and CO molecules and xenon atoms

A. K. Shuaibov, A. I. Dashchenko, A. A. Sinishin, and V. S. Shevera

Uzhgorod State University, Uzhgorod, Ukraine
(Submitted May 5, 1997)
Pis'ma Zh. Tekh. Fiz. **23**, 71–76 (October 12, 1997)

An investigation is made of the electrical and optical characteristics of a moderate-pressure transverse discharge in typical active media of infrared CO lasers. The discharge was ignited in a system of unprofiled ''grid–plane'' electrodes with automatic ultraviolet preionization by a corona discharge and had a 2×3 cm aperture. The pulse repetition frequency was 1–10 Hz, the current pulse length was $\leqslant0.5$ μs, and the pressure of the working mixtures was 10–100 kPa. Studies were made of the transverse discharge current voltage pulses, and also the spectral and temporal characteristics of the plasma radiation in N_2:CO, He:N_2:CO, and He:N_2:CO:Xe mixtures in the ultraviolet and visible ranges. © *1997 American Institute of Physics.* [S1063-7850(97)01310-4]

Since the beginning of their research and development,[1] electric-discharge CO lasers operating in the $\lambda=5.0$–5.5 μm range have been regarded with interest (alongside CO_2 molecular lasers) for technological applications. The shorter lasing wavelength than CO_2 lasers makes them more promising for technological applications, but until recently these have been impeded by the need to cool the active media of CO lasers to liquid nitrogen temperatures.[2] Now, by a using a medium-pressure electrical discharge with a high pump pulse repetition frequency, it has become possible to develop relatively simple electric-discharge CO lasers operating at room temperature. For instance, an efficiency of 13.5% and an average output power of 100–250 W at $T=300$ K have been achieved in a microwave-pumped CO laser.[3] The energy and spectral characteristics of this CO laser depended strongly on the Xe concentration in the He:N_2:CO:Xe:O_2 mixture. In studies of these lasers particular attention has been paid to the energy and spectral characteristics of the plasma in the infrared[4,5] but very few investigations have been made in the visible and ultraviolet. Results of similar investigations for the active media of CO_2 lasers were described in Refs. 6 and 7.

Here we present results of an investigation of the electrical and optical characteristics of a submicrosecond moderate-pressure transverse discharge in N_2:CO, He:N_2:CO, and He:N_2:CO:Xe mixtures in the 250–600 nm spectral range.

1. The experiments were carried out using a transverse discharge module. A photoelectric system was used to record the plasma radiation, current, and voltage pulses on the electrodes. A transverse discharge was ignited in a system of unprofiled ''plane–grid'' electrodes with a working surface area of 3×30 cm and an interelectrode gap of 2 cm. Preionization was provided by a pulsed corona discharge between the points of the needles and the grid. The discharge was ignited using an inverting LC system with a 90 nF main working capacitor and a 2 nF peaking capacitor. The switch was a TGI1 2500/50 thyratron. The repetition frequency of the current pulses was 1–10 Hz. The ultraviolet preionization system was supplied using a pulsed corona discharge from a capacitor $C=0.47$ nF across the needle–grid gap, which ignited automatically 50–150 ns before the main discharge. The plasma radiation spectra were studied using an MDR-2 monochromator, a Foton photomultiplier, and a KSP-4 automatic plotter. The pulsed plasma radiation was recorded with an ÉLU-14 FC linear electron multiplier and a 6LOR-04 oscilloscope.

2. Figure 1 shows a typical plasma emission spectrum for a transverse discharge in a He:N_2:CO:Xe mixture. The highest-intensity radiation from molecules and their ions in an N_2:CO discharge was recorded on the following transitions: $CO(b^3\Sigma^+-a^3\Pi)$, $CO(d^3\Delta_1-a^3\Pi)$, $CO(a^3\Sigma^+-a^3\Pi)$, $CO(B-A)$, $N_2(C-B)$, $CN(B-X)$, NO-(β-, γ-systems), $N_2^+(B-X)$, and $OH(A-X)$. As the content of nitrogen molecules in the double mixture decreased, the intensity of radiation in the bands of the $CO(B-A)$ Ångstrom system increased compared with those of the $N_2(C-B)$ system and the intensity of the radiation from the CN radical at $\lambda=388$ nm. The nature of the emission spectrum changed for a transverse discharge in a He:N_2:CO=20:4.8:1.6 kPa mixture: emission bands of $Co^+(B-X)$ ions appeared in the $\lambda=$ 250–280 nm range, the intensity of the radiation from N_2 and CO molecules was enhanced in the visible range, and ultraviolet bands of N(β, γ systems) and $CN(B-X)$ bands were observed. The appearance of CO^+ ion emission bands was caused by Penning ionization of CO molecules by metastable He atoms.[8]

3. Figure 2 shows oscilloscope traces of the voltage pulses, current, and radiation pulses due to the molecular transitions. The base length of the main voltage pulse was 100 ns whereas that of the current was $\leqslant500$ ns. The voltage pulses for the nitrogen and carbon monoxide molecular transitions exhibited long afterglows. The first short peak of the emission pulses for the electronic–vibrational transitions of N_2 and CO molecules occurred during the rise time of the current pulse and had a duration of $\leqslant30$ ns while the base length of the second peak was 200–300 ns. Almost no afterglow was observed for emission on transitions of the CN radical (Fig. 2). The first peak of the emission pulse appeared during the leading edge of the transverse-discharge current

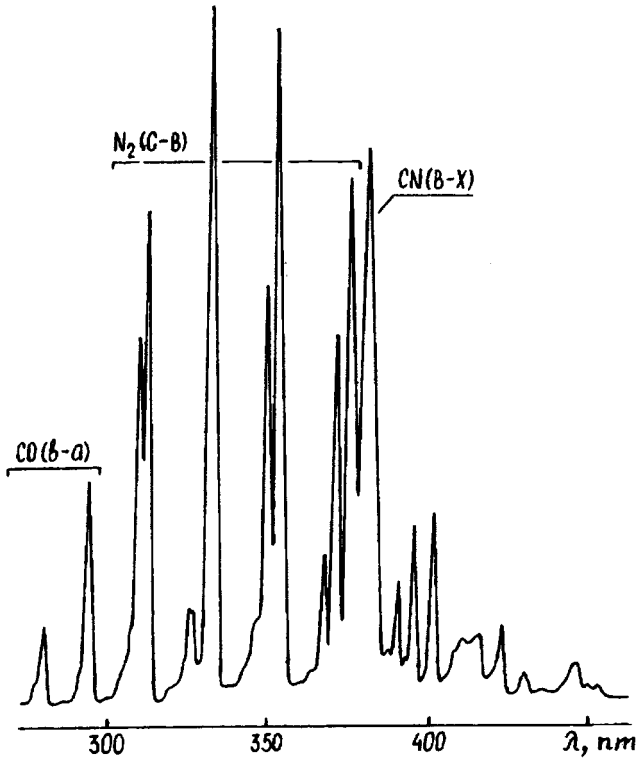

FIG. 1. General emission spectrum of a transverse discharge plasma in a He:N_2:CO:Xe=8.1:3.2:1.6:0.4 kPa mixture.

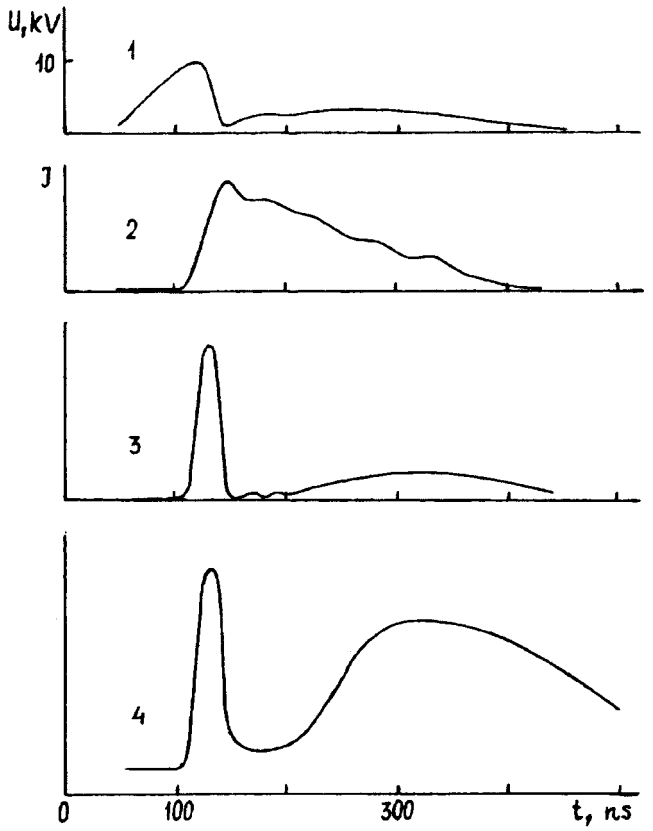

FIG. 2. Oscilloscope traces of voltage (*1*), current (*2*), and emission at $\lambda=337$ nm $N_2(C-B)$ (*3*), and $\lambda=388$ nm $CN(B-N)$ (*4*) for a transverse discharge in a He:N_2:CO=8.5:3.2:1.6 kPa mixture.

and was attributed to direct electron impact excitation of the upper states of N_2 and CO molecules. The second peak occurred during the decay time of the transverse discharge current pulse and was probably caused by interaction between metastable molecules. The second peak of the afterglow on the $N_2(B-X)$ transitions had the largest area for the N_2:CO discharge and the smallest for the He:N_2:CO:Xe mixture. Since the main source for filling of the $N_2(C)$ state in the discharge afterglow is associative exchange:[9,10]

$$N_2(A,v=1)+N_2(A,v=0)\rightarrow N_2(X,v=2)+N_2(C), \quad (1)$$

the addition of easily ionized impurities (Xe atoms) leads to a drop in the density of metastable nitrogen molecules and reduces the intensity of the emission on the $N_2(C-B)$ transitions in the discharge afterglow.

4. A uniform discharge with a 2×3 cm aperture was obtained in all active media of the electric-discharge CO laser, which allows us to simulate the conditions for excitation of a microwave-pumped CO laser at low pulse repetition frequencies and at room temperature. No significant heating of the gas mixtures was observed under the experimental conditions, as could be seen from the weakly developed rotational structure of the radiation on transitions in the 2^+ system of N_2. In helium-rich media the uniformity of the discharge was conserved as far as pressures of 1–1.5 atm.

To conclude, our investigation of the characteristics of a moderate-pressure transverse discharge in N_2:CO and He:N_2:CO(Xe) mixtures has shown that a uniform glow discharge with a 6 cm^2 aperture may be obtained in a system of unprofiled electrodes with pulsed corona preionization. This discharge excitation system can be used to study processes of excitation of the electronic states of N_2 and CO molecules, which provide a channel for parasitic loss of discharge pump power in infrared CO lasers. Small amounts of xenon added to the active media of CO lasers caused a drop in the electron temperature which was observed as a decrease in the intensity of the second emission peak on the $N_2(C-B)$ and $CO(b-a)$ transitions.

The authors would like to thank V. V. Skubenich for assistance with interpreting the plasma emission spectra.

[1] N. N. Sobolev and V. V. Sokovikov, Kvantovaya Elektron. (Kiev), No. 4(10), 3 (1972).
[2] V. V. Blinov, V. M. Vakhulenko, I. B. Kovsh, and Yu. Ya. Usanov, Itogi Nauki Tekh. Ser. Élektronika **28** (1991).
[3] S. Sato, K. Shimizu, and K. Shimamoto, Opt. Lett. **19**, 719 (1994).
[4] H. Kanazawa, F. Matsuzaka, M. Uehara, and K. Kasuya, IEEE J. Quantum Electron. **30**, 1448 (1994).
[5] A. P. Averin, V. A. Bel'kov, E. P. Glotov, A. N. Gol'shkov *et al.*, Kvantovaya Elektron. (Moscow) **11**, 1856 (1984) [Sov. J. Quantum Electron. **14**, 1245 (1984)].
[6] D. V. Gurevich, M. A. Kanatenko, and I. V. Podmoshenskiĭ, Zh. Prikl. Spektrosk. **44**, 908 (1986).
[7] A. A. Kuchinskiĭ, B. V. Lyublin, and V. A. Sheverev, Zh. Prikl. Spektrosk. **45**, 364 (1986).
[8] N. B. Kolokolov and A. B. Blagoev, Usp. Fiz. Nauk **163**(3), 55 (1993) [Phys. Usp. **36**, 152 (1993)].
[9] Yu. V. Golubovskiĭ and V. M. Telezhko, Teplofiz. Vys. Temp. **2**, 996 (1984).
[10] S. M. Kurkin and V. M. Shashkov, Teplofiz. Vys. Temp. **22**, 999 (1984).

Translated by R. M. Durham
Edited by Steve Torstveit

Space–time chaos during the formation of a solid state

N. V. Bodyagin and S. P. Vikhrov

State Radio Engineering Academy, Ryazan
(Submitted April 21, 1997)
Pis'ma Zh. Tekh. Fiz. **23**, 77–80 (October 12, 1997)

An analysis is made of the dynamics of formation of the solid phase of a substance. It is established that the solidification process includes a stage of low-dimensional space–time chaos. The idea of reconstructing the growth dynamics from the structure of a material is discussed.
© *1997 American Institute of Physics.* [S1063-7850(97)01410-9]

The transition from the liquid (gaseous) to the solid state of a material is a self-organization process whose dynamics may be studied using the Takens method, well known in the theory of nonlinear systems.[1]

As it solidifies, a material changes its properties with time and is distributed nonuniformly in space, i.e., it is a space–time system. To reconstruct its dynamics, we need to reconstruct the time evolution using the Takens method at various points in the material structure. While such an approach is possible, it is incompatible with existing computing capabilities. It is more promising to obtain information on the growth dynamics from the characteristics of the material structure.

It was shown in Ref. 2 that the spatial distribution of a ''snapshot'' of a space–time system may be reconstructed using methods developed to reconstruct the temporal evolution. The surface of a material is a ''snapshot'' of the solidification processes. On this basis, we measured the fractal dimension D_S of surfaces of gallium arsenide, carbon, amorphous silicon, tungsten, and other materials using the surface profile obtained with a tunneling electron microscope. The height of the profile was measured from a certain level, taken as zero, and was measured at discrete intervals for 15 000–20 000 points in each case. The data were processed using the Grassberger–Procaccia algorithm. It was established that for all surfaces, the value of D_S was between two and three and had a fractional part. Similar values of D_S were observed for surfaces of various materials analyzed by adsorption techniques, secondary electron spectroscopy, and small-angle scattering, and also in the structure of porous and amorphous materials.[3,4]

The fact that the fractal dimension has the value $2<D_S<3$ implies[5] that the surface structure of the materials may be described as ''frozen'' low-dimensional chaos.

By analogy with the Lyapunov exponents λ_t characterizing the time evolution of a system, we introduce the concept of the spatial Lyapunov exponents λ_r for the surface structure. These exponents may be determined by methods of measuring λ_t by directly replacing time by distance.

The exponents λ_r and λ_t characterize the stability of the space–time system. Positive λ_t determine the rate of divergence of nearby trajectories of the system in phase space and are calculated according to the formula

$$\lambda_t = A/t_c, \tag{1}$$

where A is a constant and t_c is the correlation time over which the system loses information about its initial state. By analogy, it may be postulated that λ_r characterizes the spatial correlations and is defined as

$$\lambda_r = B/l_c, \tag{2}$$

where B is a constant and l_c is the correlation length, i.e., the distance between two regions of the material structure over which the relative information between the regions becomes zero. From the point of view of thermodynamics, λ_r determines the degree of disequilibrium of the material structure.

It was shown in Ref. 6 that l_c and t_c are determined by

$$l_c = \rho_t/2\rho_S, \tag{3}$$

$$t_c = \rho_r/2\rho_S, \tag{4}$$

where ρ_t and ρ_r are the densities of the temporal and spatial dimensions, and ρ_S is the density of the ordinary entropy. However, we find

$$\rho_t/\rho_r = v_i, \tag{5}$$

where v_i is the rate of propagation of information in the medium.[7] When formulas (3) and (4) are taken into account, expression (5) becomes

$$l_c/t_c = v_i. \tag{6}$$

In solidification processes the information carriers are atoms of the material which reach the surface during growth. Thus, v_i is equivalent to the rate of formation of the solid state v_g, and expression (6) may be rewritten as

$$l_c/t_c = v_g. \tag{7}$$

Substituting into Eq. (7) the expression for l_c and t_c from formulas (1) and (2), we obtain

$$\lambda_t/\lambda_r = Cv_g, \tag{8}$$

where $C=A/B$ is a constant. Clearly C and v_g are positive values. It therefore follows from expression (8) that if $\lambda_r>0$ exists, then $\lambda_t>0$ also exists. In other words, if the system is distributed chaotically in space, it will also behave irregularly in time. The reverse statement is clearly also true for large space–time systems.

Since the surface structure of materials comprises ''frozen'' chaos, at least one $\lambda_r>0$ is found.[5] Consequently, there exists at least one $\lambda_t>0$ and the dynamics of formation

of the solid state is determined by space–time chaos of low dimension.

The proposed approach can be used to identify the dynamics of growth processes by using methods of nonlinear dynamics to analyze information on the structure of materials obtained by traditional methods. An accurate knowledge of the dynamics can be applied to control solidification processes and obtain a material with a prespecified structure.

[1] A. A. Aivazov, N. V. Bodyagin, and S. P. Vikhrov, Proc. Mater. Res. Soc. **420**, 145 (1996).
[2] V. S. Afraimovich, A. B. Ezersky, M. I. Rabinovich *et al.*, Physica D **58**, 365 (1992).
[3] V. S. Ivanova, A. S. Balankin, I. Zh. Bunin, and A. A. Oksogoev, *Synergetics and Fractals in Materials Technology* [in Russian], Nauka, Moscow (1994).
[4] E. Feder, *Fractals* (Mir, Moscow, 1991).
[5] G. Nicolis and I. Prigogine, *Exploring Complexity* (Freeman, New York, 1989; Mir, Moscow, 1990).
[6] L. N. Korzinov and M. I. Rabinovich, Izv. Vyssh. Uchebn. Zaved Prikl. Nelin. Dinam. **2**(1), 59 (1994).
[7] P. Grassberger, Physica Scripta **40**, 346 (1989).

Translated by R. M. Durham
Edited by Steve Torstveit

Dynamical criteria for reproducibility of the structure of solid materials

N. V. Bodyagin and S. P. Vikhrov

State Radio Engineering Academy, Ryazan
(Submitted April 21, 1997)
Pis'ma Zh. Tekh. Fiz. **23**, 81–84 (October 12, 1997)

Reasons for the irreproducibility of the structure of solid materials grown under the same technological conditions are examined. Dynamical criteria for irreproducibility are developed, and a fundamental limit on the irreproducibility and its dependence on the dimensions of the system are determined. © *1997 American Institute of Physics.* [S1063-7850(97)01510-3]

The poor reproducibility of the structure of materials synthesized by the same technology is a major problem. Its existence is usually attributed to deviations of various technological parameters from the norm, and the chief means of improving reproducibility is assumed to be a matter of specifying the parameters to better precision. This approach is ineffective, however. One reason for this is the absence of criteria for assessing the influence of various factors on the reproducibility.

It was shown in Ref. 1 that the solid state is formed via a stage of low-dimension dynamical chaos. We postulate that the instability of the motion characteristic of chaotic dynamics is responsible for the poor reproducibility of the structure of materials. Thus, the reproducibility criteria should be related to the invariant characteristics of chaotic systems. We consider several such criteria.

1. Kolmogorov–Sinai entropy (S_{KS}). This is the sum of positive Lyapunov exponents and characterizes the degree of instability of the growth processes.

2. The solidification process takes place directly in an intermediate layer between the solid and liquid (gas) phases. The reproducibility criterion is the relation between the time of existence t_{IL} of the material in this layer and the time $T_{\max}$ over which the system still remembers its initial state. The time t_{IL} is given by

$$t_{\mathrm{IL}} = d_{\mathrm{IL}}/v_g, \tag{1}$$

where d_{IL} is the layer thickness and v_g is the growth rate. The time $T_{\max}$ can be expressed in the form:[3]

$$T_{\max} = (\rho_D/\rho_S)\log(1/\varepsilon), \tag{2}$$

where ρ_D is the fractal dimension density, ρ_S is the entropy density, and ε is the precision of defining the initial state, which is determined by deviations of the topological parameters Δp from the norm and by the fluctuations f:

$$\varepsilon = \Delta p + f. \tag{3}$$

The following cases are possible: if $t_{\mathrm{IL}} \ll T_{\max}$, the structure of the material is accurately reproduced, if $t_{\mathrm{IL}} \approx T_{\max}$, it is partially reproduced, and if $t_{\mathrm{IL}} \gg T_{\max}$, it is poorly reproduced.

3. The degree of reproducibility may be characterized in terms of the average relative information.[2] Let us suppose that as a result of measurements of some characteristic at various points in the structure of the material produced in the first process, we obtain the set $s(1)$ and in the second process we obtain the set $s(2)$. The average relative information between these sets is determined according to the formula

$$I(1,2) = \sum P(s(1),s(2))\log_2[(P(s(1), s(2))/(P(s(1))P(s(2))], \tag{4}$$

where $P(s(1))$ and $P(s(2))$ are the probability functions for the characteristics of both materials, and $P(s(1), s(2))$ is the combined probability. The summation in expression (4) is over the number of measurements.

The average relative information can be determined experimentally from the profile of the material surface, the histogram of the radial distribution function, and the optical absorption spectra.

All these criteria are invariant with respect to specific technologies and can be applied to assess the influence of various factors on the reproducibility. These criteria may be calculated using methods and algorithms used to determine the characteristics of nonlinear systems.[2]

A consequence of the dynamical instability of the growth processes is the existence of a fundamental reproducibility limit R_{lim} which determines the limiting precision of defining the technological parameters, above which any increase in precision is ineffective.

The perturbation growth in the structure of a material during solidification is given by

$$R = \varepsilon \exp(S_{KS} t_{\mathrm{IL}}). \tag{5}$$

Assuming $\Delta p \to 0$ in Eq. (3), we obtain the value R_{lim} which is associated with unavoidable fluctuations and cannot be reduced.

The value of R_{lim} is determined as the point when the dependence of R on Δp saturates. This implies that f becomes greater than Δp.

It was shown in Ref. 4 that the following dependence on the system dimension V is valid for the Lyapunov exponents:

$$\lambda = C/V, \tag{6}$$

where C is a constant. From this it follows that as V decreases, the Lyapunov exponents and therefore the degree of irreproducibility increase.

However, near the stable state the amplitudes of the internal fluctuations behave as $1/V$. At the critical point they increase as values of the order of $V^{-1/2}$. Thus, for macroscopically large systems the internal fluctuations are negli-

gible. For small systems the internal fluctuations play an important role together with the external ones and are also responsible for reducing the reproducibility.

These conclusions are relevant to the technologies of microelements and nanoelements used in microelectronics.

The reason why the appearance of any structure is probabilistic and cannot be reproduced repeatedly stems from the instability of the growth processes deriving from the chaotic dynamics. Simply specifying the technological parameters to greater precision is the least effective way of improving the reproducibility. It is necessary to employ methods used to control nonlinear systems based on an accurate knowledge of the dynamics of the processes.

[1] A. A. Aivazov, N. V. Bodyagin, and S. P. Vikhrov, Proc. Mater. Res. Soc. **420**, 145 (1996).
[2] H. D. I. Abarbanel, R. Brown, and J. J Sidorovich, Rev. Mod. Phys. **65**, 1331 (1993).
[3] L. N. Korzinov and M. I. Rabinovich, Izv. Vyssh. Uchebn. Zaved. Prikl. Nelin. Dinam. **2**(1), 59 (1994).
[4] P. Grassberger, Physica Scripta **40**, 346 (1989).

Translated by R. M. Durham
Edited by Steve Torstveit

Formation of complex multifrequency signals by a magnetron amplifier

S. V. Voskresenskiĭ and G. G. Sominskiĭ

St. Petersburg Technical University
(Submitted April 30, 1997)
Pis'ma Zh. Tekh. Fiz. **23**, 85–89 (October 12, 1997)

Experimental results are obtained which demonstrate that a nonautonomous electron-oscillator system in a magnetron-type device becomes randomized under the action of a nonharmonic signal. © *1997 American Institute of Physics.* [S1063-7850(97)01610-8]

In crossed-field magnetron systems, the space charge confined by a magnetic field and by edge electric fields in a single three-dimensional trap is unstable and is usually in oscillatory states.[1–3] Studies of collective processes in the space charge in these systems can provide a better understanding of the mechanisms and laws governing the complex dynamics of distributed electron systems, and are also needed to identify effective methods of improving existing systems and developing powerful new sources of microwave oscillations. It has recently been established that useful information on the oscillations of an electron cloud in crossed fields may be obtained, not only in passive measurements (see, for instance, Refs. 1–3) of current modulation at its confining electrodes or of the radiation emitted by the electron cloud, but also by active probing with specially generated rf signals.[4] Here we continue our experimental investigation of the action of external rf signals on the oscillations of the space charge in crossed fields.

The measurements were made using a high-power pulsed amplitron with a secondary-emission cathode in the decimeter wavelength range. The amplitron was triggered by an input signal at frequency f_i from an auxiliary magnetron. Control signals were generated by axisymmetric rf fields in the end part of the interaction space in the amplitron.[4] We studied the action of harmonic signals having a time-constant amplitude and power P_s up to approximately 600 W in the frequency range $100 \leqslant f_s \leqslant 600$ MHz, and also of time-decaying multifrequency signals whose typical form is shown in Fig. 1a. The maximum amplitude of the multifrequency signal U_{MF} was 10 kV and its duration did not exceed 50 ns. Changes in the amplitude-frequency characteristics of the natural space-charge oscillations in the cathode region of the amplitron and also in its rf exit channel were monitored under the action of the control signals. The spectral characteristics of the oscillations were determined by Fourier analysis of single time realizations of signals of $\sim$5–50 ns duration using a method described in Ref. 4. This procedure allowed us to identify changes in the ''instantaneous'' spectra of the anode current pulse of the amplitron at various times.

It was established that the action of the harmonic signals is a threshold process (noticeable for $P_s \geqslant 50$–100 W) and most strongly influences the spectrum of space charge oscillations at discrete frequencies of similar value or multiples of the characteristic frequencies f_a of its so-called axial oscillations.[1,4] The nature of the action varies negligibly during the entire anode current pulse. Either a decrease or an increase in the components of the oscillation spectrum of the electron cloud was observed under different operating conditions of the amplitron (for different values of the magnetic field B and the anode voltage U_a). Changes in the characteristics of the space charge oscillations appreciably influenced the spectrum of the amplitron output signal. Parasitic signals near frequencies $f_i + nf_a$, where n is an integer in the range $1 \leqslant n \leqslant 3$, were usually observed. The amplitudes of these parasitic signals were 15–20 dB lower than the amplitudes A_i of the output signal at frequency f_i. Figures 1b and 1c show typical changes in the amplitude A of the discrete peaks of the spectrum in the output channel as a function of the frequency f_s (Fig. 1b) and power P_s (Fig. 1c) of the control signal. These measurements indicate first, that the axial oscillations of the space charge may be controlled by the generated rf fields and second, that there is a relation between the parasitic oscillations of the amplitron and the collective processes in the cathode liner of the electron cloud.

The data obtained indicate that the spectrum of the amplitron output signals is considerably more strongly influenced by the large-amplitude multifrequency signals. The spectra were recorded with a delay τ_d relative to the beginning of the multifrequency signal pulse, which varied in the range $50 \leqslant \tau_d \leqslant 500$ ns. Figure 2 shows typical spectra of the output signal recorded without a control signal (Fig. 2a) and for the maximum signal $U_{\mathrm{MF}} = 10$ kV (Fig. 2b). It can be seen that under the action of the multifrequency signals oscillations are observed in a wide frequency band $f_i \leqslant f \leqslant 2.5 f_i$ and their amplitudes A_f are close to the amplitude A_i at the frequency f_i. The ratio A_f/A_i varies comparatively little for 100–150 ns after the end of the multifrequency signal and only then decays rapidly in time. For a fixed delay $50 \leqslant \tau_d < 100$–150 ns, the amplitudes A_f of the signals increase with increasing U_{MF} over the entire frequency range $f_i \leqslant f \leqslant 2.5 f_i$. Figure 2 shows typical changes in the average values of A_f/A_i for a series of frequency intervals 500 MHz wide in the range between 1.5 and 6.0 GHz, as a function of the delay τ_d (Fig. 2c) and the amplitude of the multifrequency signal (Fig. 2d). Estimates of the absolute power values show that in the typical amplitron operating regime $B = 0.12$ T, $U_a = 13.5$ kV, when the output power in the absence of the control signal is $P_0 \sim 30$ kW, the application of a multifrequency signal, redistributing the rf energy over the spectrum, more than halves the specific (per unit frequency interval) power at the frequency f_i. In this case, the total power is increased 1.5–2 times in the entire range $f \leqslant 2.5 f_i$.

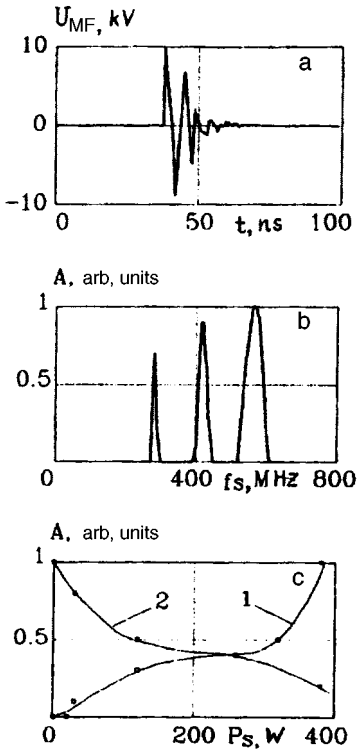

FIG. 1. a — Typical profile of multifrequency control signal $U_{MF}(t)$; b — change in the amplitude A of the parasitic signal in the output channel at frequency $f \sim 0.92 f_i$ as a function of the frequency f_s of the harmonic control signal, measured at maximum power P_s; c — change in the amplitude A of the parasitic signals in the exit channel at frequencies $f \sim 0.92 f_i$ (*1*) and $0.93 f_i$ (*2*) as a function of the power P_s of the harmonic control signal measured at frequencies f_s: *1* — 140 MHz, *2* — 560 MHz. The characteristics in Figs. 1b and 1c were measured for the magnetic field $B = 0.1$ T and the anode voltage $U_a = 10.5$ kV.

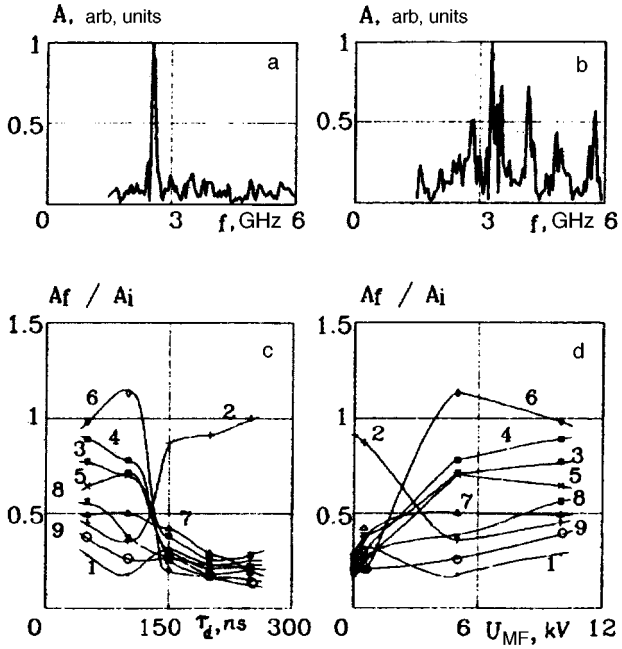

FIG. 2. Characteristics of the output signal measured at $B = 0.12$ T and $U_a = 13.5$ kV. a — spectrum without control signal; b — spectrum with maximum multifrequency signal $U_{MF} = 10$ kV; c, d — dependences of the average values of A_f / A_i on the delay τ_d (c) and the amplitude U_{MF} (d) of the multifrequency signal for a series of frequency intervals 500 MHz wide in the range between 1.5 and 6.0 GHz: *1* — 1.5–2.0 GHz, *2* — 2.0–2.5 GHz, *3* — 2.5–3.0 GHz, *4* — 3.0–3.5 GHz, *5* — 3.5–4.0 GHz, *6* — 4.0–4.5 GHz, *7* — 4.5–5.0 GHz, *8* — 5.0–5.5 GHz, and *9* — 5.5–6.0 GHz.

Under these conditions, the electronic efficiency of an amplitron with a multifrequency output signal was ~35%. Thus, these investigations indicate that the output power spectrum of the amplitron becomes substantially more complex and a large-amplitude multifrequency wide-band signal is efficiently formed under the action of the multifrequency signal. As far as we are aware, these data demonstrate for the first time that the nonautonomous electron-oscillator system of a device of the magnetron type becomes randomized under the action of a nonharmonic signal. These results are not only of purely scientific but also of practical interest, since they suggest possible ways of using this effect to develop high-power, broad-band sources of noise signals.

[1] G. G. Sominskiĭ, *Lectures on Microwave Electronics* (Fourth Winter School/Seminar for Engineers), Book 3, Saratov State University Press, Saratov (1978), pp. 119–138.
[2] S. A. Levchuk, G. G. Sominskiĭ, and S. V. Voskresenskiĭ, Pis'ma Zh. Tekh. Fiz. **14**, 1194 (1988) [Sov. Tech. Phys. Lett. **14**, 523 (1988)].
[3] S. A. Levchuk, and G. G. Sominskiĭ, Pis'ma Zh. Tekh. Fiz. **16**(10), 1 (1990) [Sov. Tech. Phys. Lett. **16**, 362 (1990)].
[4] A. V. Arkhipov, L. Yu. Bogdanov, S. V. Voskresenskiĭ, S. A. Levchuk, O. I. Luksha, and G. G. Sominskiĭ, Izv. Vyssh. Uchebn. Zaved. Prikl. Nelin. Dinam. **3**, Part 1, No. 4, 41; Part 2, No. 5, 35 (1995).

Translated by R. M. Durham
Edited by Steve Torstveit

Temperature dependence of the ion yield in electron-stimulated desorption

S. Yu. Davydov

A. F. Ioffe Physicotechnical Institute, Russian Academy of Sciences, St. Petersburg
(Submitted June 11, 1997)
Pis'ma Zh. Tekh. Fiz. **23**, 90–94 (October 12, 1997)

A relaxation model of electron-stimulated desorption is used to derive an analytical expression for the temperature coefficient of the yield of ions desorbed by a reverse-motion mechanism. An analysis is made of the thermal vibrations of adatoms with a temperature-dependent amplitude. The results of the calculations performed for the desorption of Na^+ ions from the surface of a silicon monolayer deposited on a tungsten substrate show good agreement with experimental results. © *1997 American Institute of Physics.* [S1063-7850(97)01710-2]

The influence of the temperature T on the ion yield q in electron-stimulated desorption has been examined in relatively few publications,[1] and the mechanism responsible for the dependence $q(T)$ remains unclear. In a series of experimental studies,[2–4] the authors examined the role of temperature effects in the electron-stimulated desorption of positive ions of alkali metals ($M^+ = Li^+, Na^+$) from the surface of tungsten and iridium ribbons coated with a silicon monolayer (M–Si/W,Ir). The experiments demonstrated that the ion yield only exhibits a strong temperature dependence when reverse motion of the desorbed ion in the direction of the substrate (Antonevich mechanism[5]) is observed at the first stage of desorption. Then, the temperature coefficient of the ion yield in electron-stimulated desorption, defined as

$$\gamma \equiv \frac{\partial \ln q}{\partial T}, \tag{1}$$

has a value in excess of 10^{-3} K^{-1}, which is an order of magnitude higher than the value of γ without this reverse motion. A theory of the temperature dependence of the ion yield in electron-stimulated desorption was developed by the author in Refs. 6 and 7 using a previously proposed relaxation model (or a local field model).[1] It was proposed that the temperature influences the amplitude of the adatom vibrations, which was equated to the rms displacement of the adatom $\sqrt{(\Delta r)^2} \propto \sqrt{T}$. The results of the calculations agreed satisfactorily with the experimental data for both direct (with no reverse) and reverse-motion desorption.

The expressions for $q(T)$ and γ obtained in Refs. 6 and 7 are extremely cumbersome and are not very convenient for immediate use, even though they only allow for changes in the length of the alkali metal–silicon adsorption bond and assume the charge at the silicon atom to be fixed. This last condition is not usually obvious: for instance when copper group metals (and also nickel and palladium) are adsorbed on the (110) surface of tungsten,[8] the temperature coefficient of the adatom dipole moment $C = p^{-1}(\partial p/\partial T)$ is of the order of 10^{-4} K^{-1}, mainly as a result of a change in the adatom charge.[9] Allowance for this factor in the theory of the temperature dependence of the electron-stimulated desorption ion yield, although not fundamentally difficult, makes the formulas even more complex. We shall proceed differently, allowing only for effects with a temperature coefficient $\geqslant 10^{-4}$ K^{-1}, i.e., we shall only analyze reverse-motion desorption. To be specific, we shall discuss the Na–Si/W system.

From the point of view of the theory,[6,7] reverse-motion desorption only differs from the direct process in having a nonzero initial velocity $v_0 = \sqrt{2B/M}$ acquired at the reverse stage and produced as a result of the short-lived repulsion of the electron shells of silicon and sodium ions $V_{rep} = B \exp[-p(r-r_0)/r_0]$, where M is the mass of a Na ion, r_0 is its equilibrium position relative to the surface of the silicon film, $p = br_0$, and b is the characteristic reciprocal length of the Born–Meyer potential. In the limit of low initial velocities $Mv_0^2 < V$, $Mv_0^2 \ll W(2W-V)/2V$, the probability $\tilde{f}(E)$ of observing a desorbed sodium ion of energy E has the form[7]

$$\tilde{f}(E) = f(E) \cdot K,$$

$$f(E) = \exp\left[-\frac{r_0}{\tau} \sqrt{\frac{2M(V+2E)}{W(2W-V)}} \right],$$

$$K = \exp\left[\frac{r_0}{\tau} \cdot \frac{2Mv_0}{2W-V} \right]. \tag{2}$$

Here $W = 4z_1 z_2 e^2 d/r_0^2$ is twice the repulsion energy of a Na^+ ion with the charge $z_2 = 1$ on one side of a dipole formed by a Si ion with the charge $z_1 > 0$ and its image in the metal, $V = z_2^2 e^2/2r_0$ is twice the energy of attraction (with the opposite sign) of a Na^+ ion to its image, and τ is the characteristic lifetime of a two-hole state at a silicon ion ($\cong 10^{-14}$ s). Note that the expression given for the function $f(E)$ is strictly speaking only valid for energies $E \to E_{min} = 0$ (this equality is only satisfied for $Mv_0^2 < V$ (Ref. 7) although it may be used for approximate calculations of the ion yield $\tilde{q}$ in electron-stimulated desorption. (Here and subsequently, the tilde indicates values referring to the case $v_0 = 0$). The ion yield $\tilde{q}$, defined as

$$\tilde{q} = \int_{E_{min}}^{E_{max}} dE \cdot (E - E_{min})^{1/2} \tilde{f}(E), \tag{3}$$

has the form

$$\tilde{q} = qK, \tag{4}$$

 1063-7850/97/100773-02$10.00 © 1997 American Institute of Physics

where the cofactor q corresponding to the ion yield in electron-stimulated desorption for $v_0=0$ is not important to determine the temperature coefficient γ (see formula (1)). The maximum kinetic energy achieved by a desorbed atom is $E_{\max}=(Mv_0^2+W-V)/2$, which follows directly from the relevant conservation law.

If we now take into account the vibrations of the adsorption system associated with the change in length of the silicon–sodium bond in the period preceding desorption, then, as discussed in detail in Ref. 7, the initial velocity v_0 varies as: $v_0 \rightarrow v_0(1+\frac{1}{2}p\xi\cos\delta)$, where $\xi=\Delta r_0/r_0$ is the relative amplitude of the Na^+ ion vibrations, and δ is the random phase of the vibrations. Averaging $K(\delta)$ over δ, i.e., performing the integration

$$\langle K\rangle=(1/2\pi)\int_0^{2\pi} d\delta\cdot K(\delta), \tag{5}$$

and substituting the resulting expression into formula (4), we obtain

$$\tilde{q}=q\cdot K\cdot I_0(ap\xi),$$

$$a\equiv M\frac{v_0 r_0}{\tau(2W-V)}. \tag{6}$$

Here I_0 is a zeroth-order Bessel function of an imaginary argument.[10] It was shown in Ref. 6 that the parameter ξ may be estimated using the formula $\xi^2=3(k_BT/E_{\text{des}})$, where E_{des} is the desorption energy of a sodium ion and k_B is Boltzmann's constant. We then have a simple formula for the temperature coefficient γ of the ion yield in electron-stimulated desorption:

$$\gamma=(ap)\cdot\left(\frac{3k_B}{E_{\text{des}}T}\right)^{1/2}\cdot\frac{I_1(ap\xi)}{I_0(ap\xi)}, \tag{7}$$

where I_1 is a first-order Bessel function of an imaginary argument.[10] Assuming as in Refs. 6 and 7 that $d=1.17$ Å, $r_0=3.26$ Å, $z_1=1$, we obtain $W=6.34$ eV and $V=2.21$ eV. Taking the value $E_{\max}=2.5$ eV from the experiment[3] and using the energy conservation law, we obtain $v_0=0.19\times10^6$ cm/s (note that the inequalities determining the low velocity regime for Eq. (2) are valid since $Mv_0^2=0.87$ eV, $V=2.21$ eV, and the right-hand side of the second of the three inequalities is 15 eV). Taking $\tau=10^{-14}$ s and $E_{\text{des}}=2.53$ eV (Refs. 11 and 12), we obtain $a=3.18$. Taking a typical p value of 5 (in molecules[13] and solids[14] p varies between 3 and 10), we obtain the average $\gamma\cong3.16$ which is almost the same as the experimental value.[3] However, it should be noted that as the temperature increases from 300 to 600 K, the theoretical value of γ decreases approximately by 20%. In the experiments[2,3] the temperature variation of the M^+ ion yield was approximated by a straight line. We propose that further experimental investigations are required on this point.

To conclude, we note that for high initial velocities satisfying the condition $Mv_0^2>V$, the ion yield does not depend on v_0 since all the ions go to infinity. This is accompanied by a sharp drop in the temperature coefficient of the ion yield, which has values of $\gamma\cong10^{-4}$ K^{-1} typical of direct desorption. Thus, there is a maximum of γ for a certain initial velocity. However, it is unclear whether there are systems where the ion acquires a velocity satisfying the above inequality at the reverse desorption stage. The difficulty here is that the reverse desorption stage cannot be investigated experimentally.

This work was carried out under the program ''Surface Atomic Structures.''

[1] V. N. Ageev, O. P. Burmistrova, and Yu. A. Kuznetsov, Usp. Fiz. Nauk. **158**, 389 (1989) [Sov. Phys. Usp. **32**, 588 (1989)].
[2] V. N. Ageev, O. P. Burmistrova, A. M. Magomedov, and B. V. Yakshinskiĭ, Fiz. Tverd. Tela (Leningrad) **32**, 801 (1990) [Sov. Phys. Solid State **32**, 472 (1990)].
[3] V. N. Ageev, A. M. Magomedov, and B. V. Yakshinskiĭ, Fiz. Tverd. Tela (Leningrad) **33**, 158 (1991) [Sov. Phys. Solid State **33**, 91 (1991)].
[4] V. N. Ageev and B. V. Yakshinskiĭ, Fiz. Tverd. Tela (St. Petersburg) **37**, 483 (1995) [Phys. Solid State **37**, 261 (1995)].
[5] P. R. Antoniewicz, Phys. Rev. B **21**, 3811 (1980).
[6] S. Yu. Davydov, Zh. Tekh. Fiz. **67**(5), 109 (1997) [Tech. Phys. **42**, 555 (1997)].
[7] S. Yu. Davydov, Zh. Tekh. Fiz. (in press).
[8] J. Kolaczkiewicz and E. Bauer, Surf. Sci. **160**, 1 (1985).
[9] S. Yu. Davydov, Surf. Sci. **364**, 477 (1996).
[10] E. Jahnke, F. Emde, and F. Lösch, *Tables of Higher Functions*, 6th ed. (McGraw-Hill, New York, 1960) [Russ. transl., Nauka, Moscow, 1977].
[11] E. G. Nazarov and U. Kh. Rasulev, *Nonsteady-State Surface Ionization Processes* [in Russian], Fan, Tashkent (1991).
[12] V. N. Ageev and B. V. Yakshinskiĭ, Fiz. Tverd. Tela (Leningrad) **27**, 99 (1985) [Sov. Phys. Solid State **27**, 57 (1985)].
[13] S. Flügge, *Practical Quantum Mechanics* (Springer-Verlag, Berlin, 1971; Mir, Moscow, 1974).
[14] C. Kittel, *Introduction to Solid State Physics*, 5th ed. (Wiley, New York, 1976; Nauka, Moscow, 1978).

Translated by R. M. Durham
Edited by Steve Torstveit

Thin-film electroluminescent structures on substrates with a diffuse-scattering emitting surface

N. T. Gurin and O. Yu. Sabitov

Ulyanovsk State University
(Submitted 12 March 1997)
Pis'ma Zh. Tekh. Fiz. **23**, 1–7 (October 26, 1997)

Results are obtained to demonstrate the significant brightness enhancement (by a factor of 3.5–5.6) of the output of thin-film ac electroluminescent emitters on glass substrates with a diffuse-scattering emitting surface as compared with the conventional designs of such emitters on ''smooth'' glass substrates. In principle, this advantage can help to solve the problem of insufficient brightness of electroluminescent emitters for certain light colors, creating a promising outlook for the fabrication of full-color, thin-film electroluminescent panel displays with a high data capacity. © *1997 American Institute of Physics.* [S1063-7850(97)01810-7]

One of the basic problems in the design of full-color, thin-film, electroluminescence panel displays is still inadequate brightness of the output from the red-light source (approximately 1/2 to 1/3 of the required brightness) and especially the blue-light source (approximately 1/5 to 1/7 of the required luminance) in the luminescence of thin-film electroluminescent emitters.[1,2] We have shown earlier that one way to enhance the brightness of thin-film electroluminescent emitters, with the potential for approximately doubling the luminance, is to use glass substrates with a roughened inner surface, on which the thin-film electroluminescent structure is deposited.[3,4] The brightness is enhanced by reducing the radiation losses associated with total internal reflection and the waveguide effect attending the lateral propagation of radiation along the thin-film electroluminescent structure, and also with the increased output of radiation from the structure due to the microlensing effect.[3,4] On the other hand, a well-known technique for increasing the radiation output from light-emitting diode (LED) structures is to use a semiconductor crystal with a diffuse-scattering emitting surface.[5]

Accordingly, the objective of the present study is to investigate the feasibility of enhancing the brightness and radiation output of a thin-film electroluminescent structure on a glass substrate with a diffuse-scattering (rough) outer surface.

To solve this problem, experiments have been conducted on thin-film electroluminescent structures in the form of metal–insulator–semiconductor–insulator–metal (MISIM), metal–insulator–semiconductor–metal (MISM), and metal–semiconductor–insulator–metal (MSIM) structures, where M is the transparent first electrode, based on SnO_2 with a thickness of 0.2 μm and deposited on a glass substrate of thickness 2 mm, plus an opaque, Al-based second thin-film electrode of thickness 0.15 μm; S is a ZnS:Mn electroluminescent layer of thickness 0.80–0.85 μm; I is a $ZrO_2 \times Y_2O_3$ (13 mass %) insulator layer of thickness 0.2–0.3 μm, all deposited on a smooth substrate, on a substrate with a rough inner surface and a smooth outer surface, on a substrate with a rough outer surface and a smooth inner surface, and on a substrate rough on both surfaces. A transparent electrode was formed on the SnO_2 by stannic chloride hydrolysis. The luminophor layer was deposited by thermovacuum evaporation, and the thin-film insulator layers were prepared by electron-beam evaporation. The rough substrates were prepared by chemical etching of the smooth substrate in hydrofluoric acid. Two series of samples of the indicated structures were investigated; all identical layers of the investigated structures in each series were produced in a common processing cycle. The two series differed in the way the structures were formed, one by photolithography (series 1) and the other by the mask technique (series 2), and also in their substrate etching regimes. According to the results of measurements using an MII-4 microscope, the rough substrates had microasperities distributed uniformly over the surface with heights and linear dimensions of the order of $(0.8–1.5)\mu$m on the outer surface and $(0.6–1.0)\mu$m on the outer surface of the glass substrate. The surface resistivities of the transparent electrode on the substrates were 250 $\Omega \cdot$m/□ for the substrate with the smooth inner surface and 400 $\Omega \cdot$m/□ for the substrate with the rough inner surface.

The luminance–voltage $B–V$ curves of the investigated structures were determined by exciting them with a sinusoidal voltage at frequency 400 Hz, 1 kHz, and 5 kHz from a GZ-56/1 audio oscillator source. The luminance was measured by means of a YaRM-3 luminance/illuminance meter within 8% measurement error limits. A G5M goniometer was used to measure the radiation directivity pattern.

A comparison of the $B–V$ curves of the MISIM structures of series 2 (Fig. 1) indicates that the maximum luminance in the saturation range of the $B–V$ curves (at a voltage of 160 V) at all frequencies using a substrate with a rough outer surface is approximately 2.1 times higher than for the structure on a substrate with both sides smooth and 2.9 times higher than for the structure on a substrate with a rough inner surface. The overall increase in the luminance of the structure on a substrate with both surfaces roughened in comparison with the structure on a substrate with both surfaces smooth is 3.5-fold. For samples of the first series the corresponding factors by which the luminance increases are 4.1, 4, and 5.6. Close values of these luminance ratios are also obtained for the MISM and MSIM structures in the corresponding series of samples. Here the absolute values of the

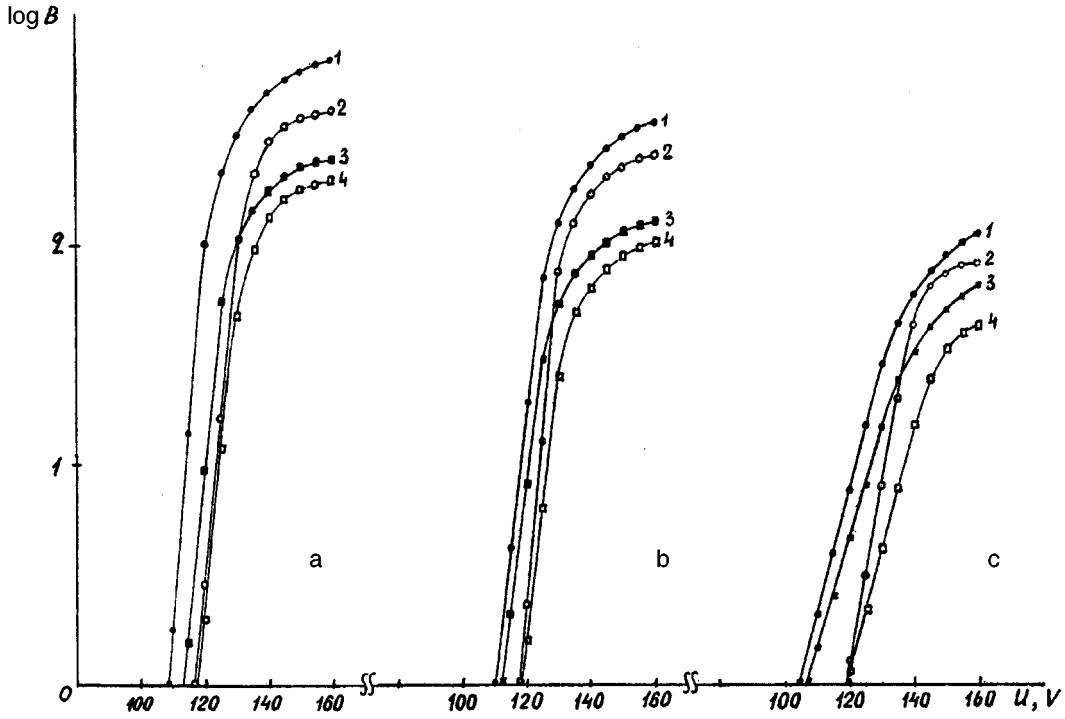

FIG. 1. Luminance-voltage curves of a MISIM structure at various frequencies and on various substrate types. a—5 kHz; b—1 kHz; c—400 Hz; *1,2*—substrates with a rough outer surface; *3,4*—with a smooth outer surface; *1,3*—with a rough inner surface; *2,4*—with a smooth inner surface.

maximum luminance of these structures is 1.2–1.4 times lower than the luminance values for an MISIM structure at the corresponding frequencies, consistent with published data.

The threshold voltages corresponding to the onset of luminescence at a luminance $B=1$ kd/m^2 for structures on substrates with a rough inner surface are 10–15 V lower in every case than for structures on substrates with a smooth inner surface.

The abrupt rise of the characteristic curves for samples of series 2 on substrates with a smooth inner surface have the largest slope, approximated by a power law with exponent $n=19$–26, in comparison with structures on substrates having a rough inner surface ($n=12$–18); these results differ somewhat from those obtained previously.[3,4] The slope of the steep segment depends slightly on the type of structure.

The curves of the luminance B as a function of the frequency f of the exciting voltage, measured in the frequency range 400 Hz–5 kHz, become straight lines in log–log coordinates $\log B(\log f)$ for all the investigated structures with their various types of substrates. In the saturation range of the B–V curves the values of the exponent α of the indicated laws for all the investigated structures are close to one another and fall within the limits $\alpha=0.65$–0.75, consistent with Ref. 4. On the other hand, where the B–V curves rise abruptly α is a maximum ($\alpha\approx 0.64$) for structures on a substrate with two smooth surfaces and decreases for a structure on a substrate with a rough inner surface and a smooth outer surface ($\alpha\approx 0.43$), in agreement with earlier results for MSIM structures.[4]. Structures on substrates with a smooth inner surface and a rough outer surface have $\alpha=0.32$, and structures on substrates with both surfaces roughened have the lowest value of the exponent, $\alpha=0.23$. These results indicate the significant influence of multiple reflections of radiation in the substrate on the final output of radiation emitted from the structure.

The radiation patterns of MISIM structures of series 1 and 2 (Fig. 2) broaden considerably in transition from structures on a substrate with a smooth outer surface (the angle of view, measured from the point where the luminance begins to drop, is equal to $\gamma_1=76$–$90°$ for structures on a substrate with a smooth inner surface and $\gamma_2=86$–$100°$ for structures on substrates with a rough inner surface) to structures on substrates with a rough outer surface ($\gamma_3=104$–$128°$). The analogous angles of view estimated at the half-maximum luminance level are $\gamma_1=144$–$156°$, $\gamma_2=158$–$164°$ and $\gamma_3=170$–$177°$. The shape of the radiation patterns corresponds to the diffuse transmission of light through a transparent substrate with one or two scattering surfaces.[6]

Other results can be explained as follows.

The significant increase in the maximum luminance of structures on substrates with a rough outer surface most likely admits an interpretation similar to that for structures on substrates with a rough inner surface,[4] being attributable to abatement of the radiation losses associated with total inner reflection and to microlensing, which has the effect of increasing the radiation output from the substrate. The lowering of the threshold voltage of structures on substrates with a rough inner surface at a fixed threshold luminance ($B=1$ kd/m^2) is caused both by an increase in the electric field in the luminophor layer at the sites of microasperities projecting above the inner surface of the substrate and by increased radiation output from the substrate. The decrease in the slope of the steeper part of the B–V curves for struc-

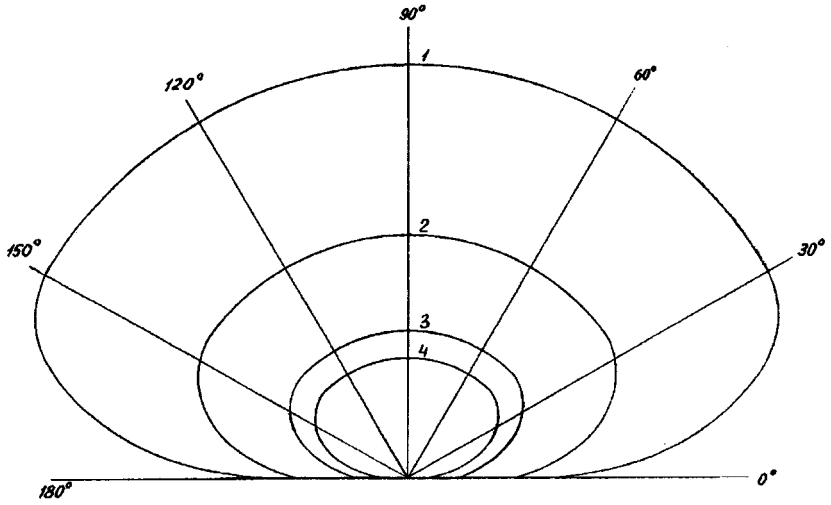

FIG. 2. Radiation patterns of MISIM structures in series 2 at a frequency of 5 kHz. *1,2*—substrates with a rough outer surface; *3,4*—with a smooth outer surface; *1,3*—with a rough inner surface; *2,4*—with a smooth inner surface.

tures on substrates with a rough inner surface is attributable to the scatter of the $B–V$ curves of individual microscopic zones of the luminescing surface of the emitters due to the scatter of the microasperity dimensions. The same cause accounts for the milder slopes of the luminance-frequency curves for structures on substrates with a rough inner surface. On the other hand, the maximum luminances in the saturation range of the B-V curves for all the structures have identical frequency dependences and are governed by saturation of the density of excited luminescence centers in the luminophor.

In summary, the application of substrates with diffuse-scattering emitter surfaces in electroluminescent emitters significantly enhances (by a factor of 3.5–5.6) the radiation output and the brightness of electroluminescent emitters, particularly in combination with substrates having a rough inner surface and, in principle, solves the problem of insufficient brightness of individual colors in the output of electroluminescent emitters, affording new prospects for the fabrication of full-color, thin-film electroluminescent panels with a high data capacity.

[1] S. Tanaka, H. Deguchi, Y. Mikami *et al.*, in *1986 SID International Symposium, San Diego, Calif., Digest of Technical Papers*, Nos. 6–8 (New York, 1986), pp. 29–32.
[2] N. A. Vlasenko, *Electroluminescent Data Logging Devices* [in Russian] (Obsch. Znanie, Ukraine, 1991).
[3] N. T. Gurin, O. Yu. Sabitov, and I. Yu. Brigadnov, Pis'ma Zh. Tekh. Fiz. **23**(15), 7 (1997) [Tech. Phys. Lett. **23**, 577 (1997)].
[4] N. T. Gurin, O. Yu. Sabitov, and V. V. Uryadnikov, in *Proceedings of the Third International Scientific-Technical Conference on Critical Problems in Electronic Instrumentation, APÉP-96* [in Russian], Vol. 1, No. 11 (Novosibirsk, 1996), pp. 20–22.
[5] D. Z. Garbuzov, N. A. Tunitskaya, V. G. Agafonov *et al.*, Fiz. Tekh. Poluprovodn. **15**, 1498 (1981) [Sov. Phys. Semicond. **15**, 868 (1981)].
[6] M. I. Krivosheev and A. K. Kustarev, *Color Measurements* [in Russian] (Énergoatomizdat, Moscow, 1990).

Translated by James S. Wood
Edited by David L. Books

Influence of transient behavior on the determination of the energy confinement time in a tokamak

M. V. Andreĭko, L. G. Askinazi, V. E. Golant, V. A. Kornev, S. V. Lebedev, L. S. Levin, and A. S. Tukachinskiĭ

A. F. Ioffe Physicotechnical Institute, Russian Academy of Sciences, St. Petersburg
(Submitted 10 June 1997)
Pis'ma Zh. Tekh. Fiz. **23**, 8–13 (October 26, 1997)

The disregard of fast processes (e.g., the L–H transition) in a tokamak plasma can lead to large errors in the determination of the energy confinement time τ_E. A major upgrade in the electromagnetic diagnostic system for the analysis of plasma parameters and in the collection system has made it possible to take into account the influence of the transient character of the radial profile and the value of the plasma current I_P as well as the stored energy W on the determination of τ_E from diamagnetic measurements and to investigate fast processes involved in the L–H transition. The energy confinement time τ_E is calculated from the equation $\tau_E = W/[U_P I_P - d/dt(LI_P^2/2) - dW/dt]$, where U_P is the plasma loop voltage (V), I_P is the plasma current (A), and L is the total internal inductance (H). The total inductance L of the plasma column has been determined from measurements of the quantity $\beta_J + I_i/2$, where β_J is the ratio between the gas-kinetic pressure and the pressure of the poloidal magnetic field, and I_i is the internal inductance. The inclusion of transient behavior in the determination of τ_E from diamagnetic measurements gives a correction of up to 50%. © *1997 American Institute of Physics.* [S1063-7850(97)01910-1]

The failure to allow for fast processes (e.g., variations in the energy content, current, or inductance of the plasma loop) can lead to sizable errors in the determination of the energy confinement time τ_E in a tokamak. The correct treatment of all the derivatives is not a simple problem, owing to the difficulty of accurately computing all the necessary quantities.

The objective of the present study of the TUMAN-3M tokamak is to determine τ_E with allowance for the transient character of the kinetic and magnetic energies in a regime with transition to the ohmic H mode and to compare with the calculation of τ_E on the assumption that these energies are time-invariant.

When the magnetic energy of the current-carrying loop and the thermal energy of the plasma are taken into account, the energy confinement time is determined from the equation[1]

$$\tau_{E3} = \frac{W}{P_{\text{input}} - d/dt(LI_P^2/2) - dW/dt}, \tag{1}$$

where W is the thermal energy stored in the plasma, P_{input} is the power input to the plasma from all external sources (without auxiliary heating methods $P_{\text{input}} = I_P U_P$, L is the inductance of the plasma loop, I_P is the plasma current, and U_P is the voltage on the sensing loop. When the variation of the magnetic energy can be disregarded $[d/dt(LI_P^2/2 = 0]$, the energy confinement time is given by the equation

$$\tau_{E2} = \frac{W}{U_P I_P - dW/dt}. \tag{2}$$

Finally, in the quasisteady-state case $[d/dt(LI_P^2/2) = 2$, $dW/dt = 0]$ Eq. (1) reduces to

$$\tau_{E1} = \frac{W}{P_{\text{input}}}. \tag{3}$$

Upgrades of the electromagnetic diagnostics and collection system and the processing of experimental data[2] have made it possible to assess the influence of the transient behavior of the radial profile of the plasma current density, the current, and the stored energy on the determination of τ_E from diamagnetic measurements, and also to investigate fast processes attending the L–H transition.

Measurements of the diamagnetic effect are used to determine W and dW/dt in Eqs. 1)–(3). The total inductance L of the plasma filament is calculated form the equation

$$L = \mu_0 R\left[\ln\left(8\frac{R}{b}\right) - \frac{3}{2} + \ln\left(\frac{b}{a}\right) + \frac{l_i}{2}\right], \tag{4}$$

where $\mu_0 = 1.26 \times 10^{-6}$ H/m, R is the large radius of the plasma filament, a is the small radius of the plasma filament, b is the distance from the sensor to the center of the plasma filament, and l_i is the internal inductance. The internal inductance is determined from measurements of the equilibrium parameter $\beta_I + l_i/2$ (Ref. 3) on the basis of the relation $\beta_I = (4/3)\mu_0\langle W\rangle/B_p^2(a)$. The signals from the Rogowski loop, the diamagnetic loops, the flux loops, and the gradient sensors, all of which are necessary for determining these quantities, are recorded and processed by the data collection system.

The measurements are performed in discharges with transition to the ohmic H mode,[4] which is characterized by fast variations of W and l_i. Figure 1 shows the time variations of the main plasma parameters in the transition to the ohmic H mode on the TUMAN-3M tokamak. Figure 2 shows the time variations of various terms in the denominator of Eq. (1) (heating power and the derivatives of the mag-

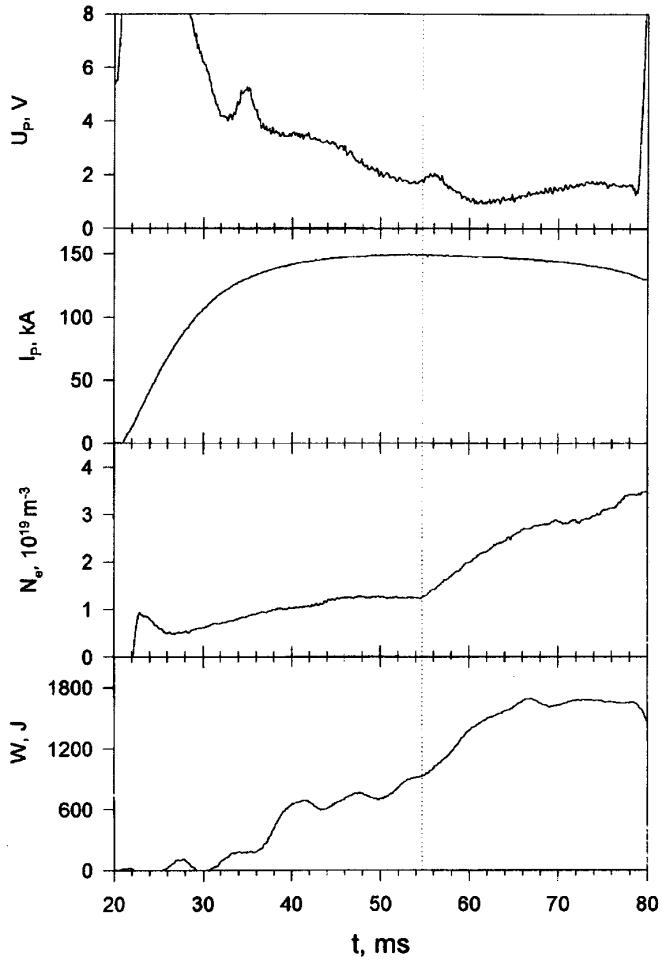

FIG. 1. Time variations of the plasma parameters in the TUMAN-3M tokamak: plasma loop voltage U_P, current in the plasma I_P, chord-averaged electron density N_e, and stored energy W. The transition to the ohmic H mode takes place at the time $t=55$ ms.

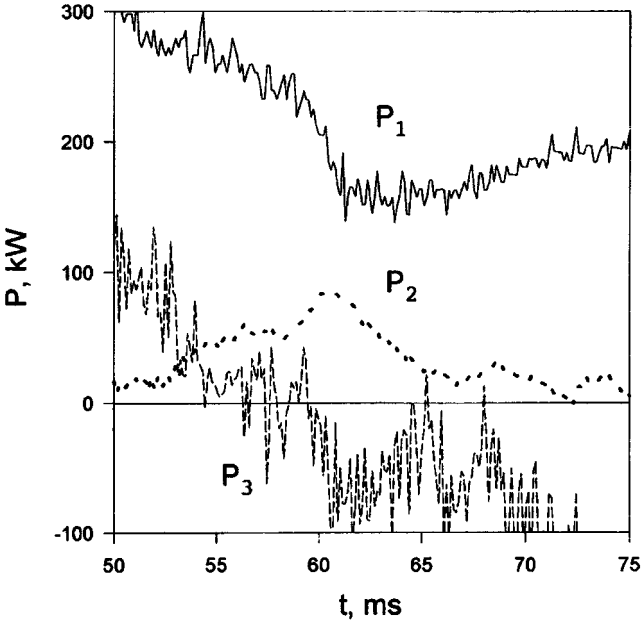

FIG. 2. Time variations of various components of the magnetic heating and derivative of the stored energy in the discharge with transition to the ohmic H mode: $P_1=U_P\cdot I_P$; $P_2=dW/dt$; $P_3=d/dt(LI_P^2/2)$.

netic and stored energies). Clearly, after transition to the ohmic H mode ($t\approx 62$ ms) none of the terms can be ignored. Figure 3 shows calculated curves of the energy confinement times. The first curve (τ_{E1}) is calculated without regard for transient behavior [according to Eq. (3)]. The second curve (τ_{E2}) is calculated with allowance for the time variation of the stored energy W [according to Eq. (2)]. The τ_{E3} curve is plotted with allowance for both dW/dt and the variation of the magnetic energy $d/dt(LI_P^2/2)$. Before the transition to the ohmic H mode ($t\leqslant 55$ ms) the main factor contributing to the disparity of the calculated energy confinement times is the variation of the magnetic energy due to the increasing plasma current. After the transition to the ohmic H mode ($t\approx 62$ ms) the energy content rises abruptly at a fixed plasma current and, accordingly, τ_{E2} differs considerably from τ_{E1}. However, allowance for the variation of the magnetic energy due to variation of the internal inductance cancels the influence of dW/dt, and $\tau_{E1}\approx\tau_{E3}$. After 62 ms the differences between τ_{E1}, τ_{E2}, and τ_3 are attributable to the variation of $d/dt(LI_P^2/2)$ as a result of the decay of the plasma current, and τ_{E3} becomes smaller than τ_{E1} and τ_{E2}.

The reported measurements and calculations have thus shown that the inclusion of transient behavior in the determination of the energy confinement time τ_E from diamagnetic measurements in various stages of the discharge can yield a correction up to 50%.

We have observed that the variation of the magnetic energy as a result of the reshaping of the current profile can significantly influence the energy confinement time. In par-

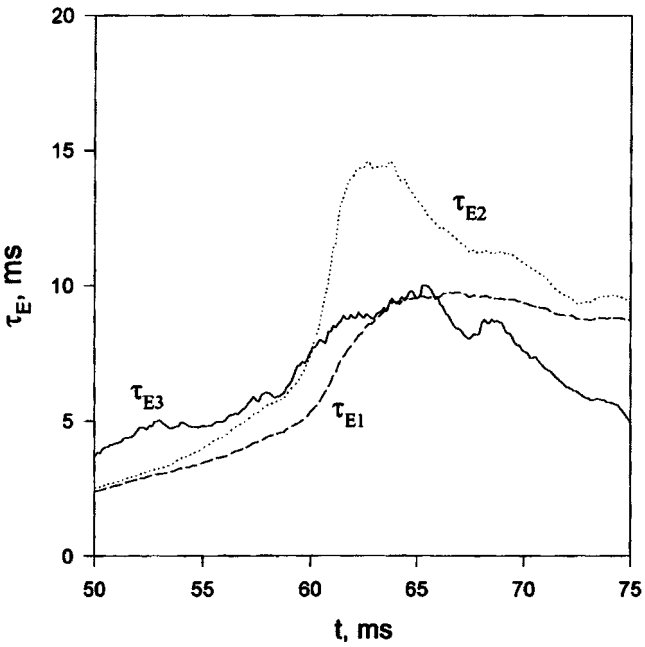

FIG. 3. Calculated energy confinement times in the discharge with transition to the ohmic H mode: $\tau_{E1}=(W/P_{\text{input}})$, $\tau_{E2}=(W/U_P\cdot I_P-dW/dt)$, $\tau_{E3}=(W/P_{\text{input}}-d/dt(LI_P^2/2)-dW/dt)$.

ticular, after transition to the ohmic *H* mode the reduction of the magnetic energy due to the decrease in the internal inductance (flattening of the radial distribution of the current density) substantially increases the power input. This phenomenon must be taken into account in determining the energy confinement time in processes accompanying the reconfiguration of the current profile.

This work has received financial support from the Russian Fund for Fundamental Research (Grant No. 97-02-18107), the Ministry of Science of Russia (TUMAN-3M Tokamak, Registration No. 01-06), and the U.S. Civilian Research and Development Foundation for the Independent States of the Former Soviet Union (CRDF Project No. RPI-197).

[1] S. V. Mirnov, *Physical Processes in a Tokamak Plasma* [in Russian] (Moscow, 1985).
[2] M. V. Andreĭko, L. G. Askinazi, V. E. Golant *et al.*, Pis'ma Zh. Tekh. Fiz. **21**(4), 65 (1995) [Tech. Phys. Lett. **21**, 159 (1995)].
[3] V. S. Mukhovatov and V. D. Shafranov, Nucl. Fusion **11**, 605 (1971).
[4] A. I. Arbuzov *et al.*, in *Proceedings of the 17th European Physical Society (EPS) Conference*, Vol. 1 (Amsterdam, 1990), p. 299.

Translated by James S. Wood
Edited by David L. Book

Fiber-optic detector using a mid-infrared diode laser and an acoustooptic modulator

N. V. Zotova, S. A. Karandashev, L. A. Kulakova, B. A. Matveev, B. T. Melekh, N. M. Stus', and G. N. Talalakin

A. F. Ioffe Physicotechnical Institute, Russian Academy of Sciences, St. Petersburg
(Submitted 10 June 1997)
Pis'ma Zh. Tekh. Fiz. **23**, 14–18 (October 26, 1997)

Data are given for an infrared detector based on a semiconductor injection laser, which operates at a wavelength of 3.3 μm and is coupled by a chalcogenide optical fiber to an acoustooptic modulator made from an amorphous Si–Te alloy. The beam modulation coefficient reaches 70% for a pulse duration $\gtrsim 0.3$ μs, making the detector well suited to gas-analysis applications.
© *1997 American Institute of Physics.* [S1063-7850(97)02010-7]

The detection of gases by optical and acoustical spectroscopic methods is most efficient in the middle infrared region of the spectrum (3–5 μm), which encompasses the absorption bands of many substances and for which injection lasers and light-emitting diodes (LED's) have now been developed with sufficiently high power output and long service life. However, the inventory of optical signal modulating devices for the middle IR region is limited, and this consideration attaches special importance to data on high-speed amplitude modulators and sensors with potential applications in the frequency band normally used for the optoacoustical analysis of gaseous media.

The radiation source is a diode laser with a broad, 1000×150 μm contact utilizing an InGaAsSb/InAsSbP double heterostructure prepared by liquid-phase epitaxy on a highly plastic InAs substrate.[1]

The power–current curves of the investigated layers have the usual profile for double-heterostructure lasers, where the differential quantum efficiency at 77 K attains 30%, and the external quantum yield is ~20%. The radiated power attains 0.25 W in pulsed operation at $I=10I_{th}$ (multimode regime) and 6 mW in continuous-wave (CW) operation at $I=2I_{th}$.

The measurement apparatus includes a cryostat with a built-in laser, which operates at a wavelength of 3.3 μm and is coupled to an As_2S_3 fiber of diameter 500 μm, an acoustooptic modulator, a gas cell, and a cooled InSb photodiode with a sensing area of 0.5×0.5 mm. The fiber was produced at the Institute of High-Purity Materials of the Russian Academy of Sciences and has losses at the 50-dB level. For a fiber 1 m in length the power of the light pulse ($\tau=5$ μs) at the output end is ~40 mW. The analogous laser is tunable in the wavelength interval 3.28–3.34 μm without any appreciable fluctuation of the radiated power, and we have used it previously for the detection of hydrocarbons.[2] The transmission spectra obtained by means of the laser for methane–nitrogen mixtures (1% and 2% Ch_4) have a minimum in the vicinity of the fundamental absorption band at $n=3018.9$ cm^{-1}, providing a means for the discrimination of methane from other substances.

An acoustooptic modulator of our own design using an amorphous Si–Te alloy is used to modulate the laser beam. A piezoelectric transducer transmits an acoustic wave into a cell of dimensions $\sim 5\times 5\times 5$ mm. The optical radiation is modulated as a result of Bragg diffraction by an ultrasonic wave. In earlier work[3] we have obtained unprecedented results using this modulator in conjunction with a CO gas laser. Here we use an He–Ne laser to investigate the acoustooptical properties of this alloy at wavelengths in the vicinity of $\lambda=3.39$ μm. The measured acoustooptical Q of the material in the investigated range is slightly lower than at $\lambda=10.6$ μm. For this reason the percentage modulation of the He–Ne laser reaches ~90% at an acoustic power of just 0.85 W.

Our investigations have shown that the Si–Te alloy acoustooptic modulator is also highly effective for the control of a semiconductor laser in spite of its pronounced beam spreading. This asset is a consequence of the high refractive index of the Si–Te alloy ($n=3.3$), which significantly reduces the beam spreading in the acoustooptic cell and enhances the efficiency of interaction. The latter quality in combination with optimum dimensions of the acoustic cell (2×3 mm) and an optimum acoustic frequency (41 Hz) has

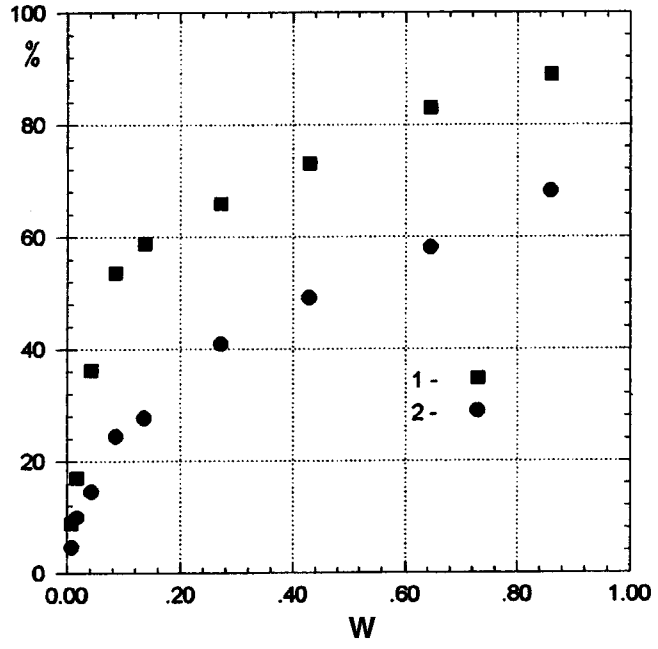

FIG. 1. Percentage modulation of two laser beams vs acoustic power. 1—Gas laser; 2—semiconductor laser.

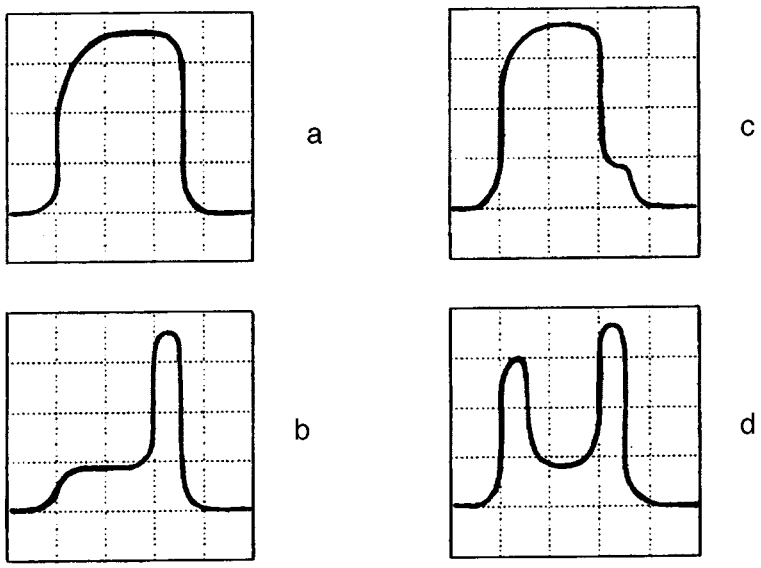

FIG. 2. Profiles of the light pulse for various acoustic pulse durations τ_{ac} and delay times τ_r of the acoustic pulse relative to the light pulse: a—$\tau_{ac}=0$ μs, $\tau_r=0$ μs; b—$\tau_{ac}=4$ μs, $\tau_r=0$ μs; c—$\tau_{ac}=1$ μs, $\tau_r=4$ μs; d—$\tau_{ac}=3$ μs, $\tau_r=1$ μs. The grid spacing corresponds to 2 μs.

enabled us to attain acoustooptic modulator parameters close to those obtained in the operation of this modulator with the highly directional He–Ne laser, as is evident from Fig. 1, without the application of additional focusing optics.

Measurements performed at laser currents of 0.6–1 A and repetition rates of 60–100 Hz have shown that the propagation of an acoustic wave into the acoustooptic modulator substantially lowers the level of the output radiation, as is evident from Fig. 2. The duration of the leading edge of the modulation pulse is $\tau=0.3$ μs, which permits the generation of relatively short light pulses with durations as short as 1 μs.

The required time interval can be defined by varying the delay time of the acoustic pulse relative to the light pulse (see Fig. 2). This feature is important at high injection currents, when the radiation wavelength varies within the limits of the pulse as a result of current-induced heating of the laser. A short ''monochromatic'' radiation signal of the required wavelength within the limits dictated by pulsed heating of the laser can be segregated by using the acoustooptic modulator for additional modulation.

In some cases the same laser can have wavelength tuning of opposite signs in pulsed and CW operation. In this event the modulator described above can be used to extend the spectral range for the analysis of substances.

The detector described here can be used to detect methane and other hydrocarbons having an absorption peak at 3.3 μm. The advantage over optical[4] and acoustic[5] hydrocarbon detectors using IR LED's is the high radiated power output of the source and the high efficiency with which the light beam is coupled into the fiber in both pulsed and CW operation of the source.

To summarize, we have demonstrated the efficient modulation of a light beam at a wavelength of 3.3 μm diverging from the end of an optical fiber; this effect can be exploited in the design of fiber-optic detectors using diode lasers and acoustic or photon signal receivers to detect substances whose absorption bands lie in the middle IR region of the spectrum.

In closing, the authors are indebted to M. Aĭdaraliev for assisting with the fabrication of the lasers and to M. F. Churbanov for furnishing the fiber sample.

This work has been supported by the Ministry of Scientific and Technical Instruction (MNTP) ''Optics and Laser Physics'' Program.

[1] T. S. Argunova, R. N. Kyutt, B. A. Matveev *et al.*, Fiz. Tverd. Tela (St. Petersburg) **36**, 3071 (1994) [Phys. Solid State **36**, 1633 (1994)].
[2] M. Aidaraliev, N. V. Zotova, S. A. Karandashov *et al.*, Infrared Phys. Technol. **37**, 83 (1996).
[3] Yu. V. Ilisavskiĭ, L. A. Kulakova, B. T. Melekh, and É. Z. Yakhkind, Akust. Zh. **40**, 307 (1994) [Acoust. Phys. **40**, 279 (1994)].
[4] S. McCabe and B. D. MacCraith, Electron. Lett. **29**, 1719 (1993).
[5] J. W. Chey, P. Sultan, and H. J. Gerritsen, Appl. Opt. **26**, 3192 (1987).

Translated by James S. Wood
Edited by David L. Books

1.94-μm light-emitting diodes for moisture-content measurements

A. A. Popov, V. V. Sherstnev, and Yu. P. Yakovlev

A. F. Ioffe Physicotechnical Institute, Russian Academy of Sciences, St. Petersburg
(Submitted 6 March 1997)
Pis'ma Zh. Tekh. Fiz. **23**, 19–25 (October 26, 1997)

High-power light-emitting diodes are demonstrated; they are characterized by a quantum efficiency of 5.5%, utilize a symmetric GaAlAsSb/GaInAsSb/GaAlAsSb double heterostructure, have a spontaneous-emission maximum at a wavelength of 1.94 μm, and operate in the temperature range from -80°C to $+60$°C. A continuous-wave optical power of 3.7 mW and a peak optical power of 90 mW in pulsed operation ($\tau\sim 1-5$ ms, $f=1$ kHz) are attained at room temperature. The principal electrical and emission characteristics are given. © *1997 American Institute of Physics.* [S1063-7850(97)02110-1]

The wavelength interval 1.8–2.0 μm is very attractive for applications in the detection and measurement of moisture content in various substances.[1] Devices employing spectral detection methods and emitting in the given interval are promising for the construction of portable analyzers and mobile, fast-monitoring industrial instruments.[2,3] In particular, instruments can be designed for the detection of moisture content in transparent and opaque materials such as paper, wood, sawdust, various sheet materials, and food products. Their radiation sources can be semiconductor emitters (light-emitting diodes — LEDs), whose spectral power density and efficiency surpass the analogous indices of thermal radiation sources. Semiconductor LEDs with their narrower emission line than thermal sources and the capability of direct electrical modulation can be used to fabricate compact analyzers distinguished by the absence of auxiliary optical filters and mechanical modulators. In the spectral interval 1.8–2.0 μm such LEDs are constructed from heterostructures using strained layers of the compounds InGaAs/GaAs (Ref. 4) and InGaAsP/InP, as well as GaInAsSb/GaSb solid solutions.[5,6] The latter constitute the most attractive material, because they rely on the strict isoperiodicity of heterostructures with a low density of misfit dislocations and are distinguished by a heightened resistance to degradation.

In the present note we report the construction of high-power LEDs with a spontaneous emission maximum at a wavelength of 1.94 μm. They operate at room temperature or higher, and we have tested them in both continuous-wave (CW) and pulsed operation. In view of the outstanding future potential of high-power LEDs for practical applications, our primary concern lies in the characteristics of pulse-driven LEDs, which are capable of attaining a high peak power in the middle infrared range at room temperature.

The LEDs comprise a symmetric GaAlAsSb/ GaInAsSb/ GaAlAsSb double heterostructure grown by liquid-phase epitaxy on an *n*-GaSb(100) substrate. The structure consists of four epitaxial layers, with the active *n*-GaInAsSb layer (of thickness 0.7 μm) contained between two *N*- and *P*-GaAlAsSb wide-gap emitters. All the layers are matched by lattice period with the GaSb substrate. The active GaInAsSb layer is characterized by an indium content of 0.08 ($E_g=0.64$ eV) and are doped with Te to a concentration of $(1-2)\times 10^{17}$ cm^{-3}. The GaAlAsSb wide-gap confining layers are grown with an Al content of 0.50 ($E_g=1.11$ eV) and are doped with Te and Ge to concentrations of $(2-4)\times 10^{18}$ cm^{-3} and $(6-8)\times 10^{18}$ cm^{-3} for the *N*-type and *P*-type layers, respectively.

We have investigated circular mesa diodes prepared by photolithography and deep chemical etching into the substrate. The total dimensions of the crystal of a single LED is 500×500 μm. The mesa diameter (300 μm) determines the area of the emitting surface ($S=7\times 10^{-4}$ cm^2). The semiconductor crystal is mounted on a standard TO-18 casing. A parabolic reflector is mounted on the TO-18 casing in such a way that the emitting crystal is positioned at the focus of the parabola, permitting the radiation from the diode to be collimated in a (10–12)° angle. The overall dimensions of the LED with the parabolic reflector are 9 mm in diameter and 5.5 mm in length.

The electrical and spectral characteristics of the diodes have been investigated by means of an apparatus assembled from a standard synchronous detection circuit, an MDR-2 monochromator, and a GaInAsSb-based photodiode. The optical power is recorded by an IMO-2M instrument.

The LED current-voltage curves exhibit typical diode behavior with a cutoff voltage of 0.50 V at room temperature ($T=300$ K) and 0.75 V at liquid nitrogen temperature ($T=77$ K). The reverse leakage current is 0.8 mA at a voltage of 1 V. The reverse breakdown voltage is temperature-sensitive and increases from 1.3 V at room temperature to 1.9 V at liquid nitrogen temperature. The series resistance with forward bias is less than $\sim 2.4\ \Omega$.

The spectral and power characteristics of the diodes have been tested with pumping in both the CW and the pulsed regime. The LED spectral characteristics at room temperature are shown in Fig. 1. At room temperature the spectrum contains one emission band ($\lambda=1.94$ μm, $T=300$ K), whose position corresponds to the width of the band gap of the active zone ($E_g=0.64$ eV). The maximum of the emission spectrum depends weakly on the injection current. The shift of the emission maximum toward longer wavelengths can be roughly described by a rate of 0.05 nm/mA. The full width at half height (FWHM) of the emission spectrum is 0.12 μm. The width of the spectrum increases slightly with the pump current (from 0.12 μm at 30 mA to 0.14 μm at 150 mA). The emission quantum efficiency is 5.5%.

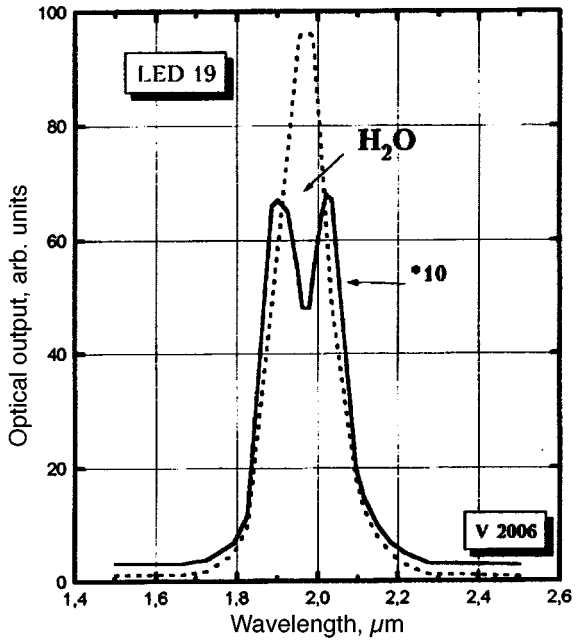

FIG. 1. Spectrum of the absorption of LED radiation by a water layer of thickness 5 μm and CW spectrum of the LED (dashed curve) at room temperature. For both spectra the FWHM of the emitted radiation is 0.12 μm, and the FWHM of the water absorption band is 0.03 μm. The injection current is 50 mA (CW).

The minority-carrier lifetime is estimated from the rise and decay times of the radiation when the pump current is switched. At room temperature it is of order $\sim$20–25 ns. We note that this is sufficient for the majority of applications, because it admits modulation at frequencies exceeding thermal noise (5–10 MHz). On the whole, the spectral and electrical characteristics are consistent with recombination in the bulk of the active zone.

Upon cooldown to liquid-nitrogen temperature, the position of the maximum of the emission spectrum shifts by 0.19 μm toward the short-wavelength end, in good agreement with the temperature dependence of the band gap of the active zone. As the temperature is lowered, the lifetime increases slightly at first, but then decreases once again.

In CW operation the optical power output of the LED increases in the range of pump currents up to 150 mA. The maximum CW power of 3.7 mW is attained for an injection current of 150 mA. At high CW currents the power-current curve goes to saturation, owing to current heating of the active zone. Our previous investigations[7] in the vicinity of 2.3 μm have shown that heating sets in at currents above 50 mA. Heating also plays a role in short-wavelength LEDs, but its influence is manifested at higher pump currents. The temperature behavior of the power-current curves has been investigated in the range from -80°C to $+60$°C. An analysis of the power-current curves in this temperature range reveals an exponential temperature dependence of the optical power output. As the temperature is lowered the power output increases, with a characteristic temperature of 80 K, and the position of the emission maximum in this case shifts toward shorter wavelengths at an average rate of the order of 0.28 nm/K. It is important to note that over the entire range

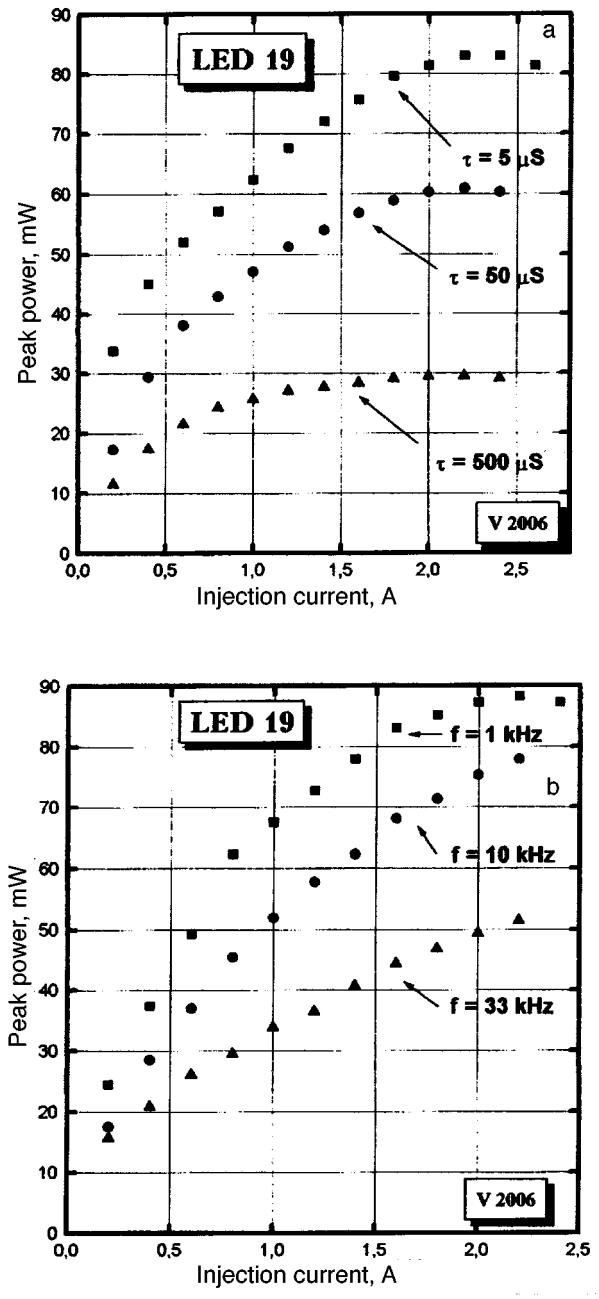

FIG. 2. Power-current curves of an LED at room temperature. a — Peak power vs repetition rate for pulses of fixed duration (τ=1 μs); b — peak power vs pulse duration for pulses with a fixed repetition rate (f=1 kHz). The curve for a pulse duration of 500 ns and repetition rate of 1 kHz corresponds to the maximum off-duty cycle. The highest peak power is attained at an off-duty cycle $\sim 10^{-3}$.

from room temperature to nitrogen temperature the emission peak shifts toward blue by 0.19 μm, which corresponds to the temperature dependence of the band gap of GaInAsSb.

To diminish the influence of heating at currents above 150 mA, investigations have been carried out in the pulsed pump regime. To investigate the pump regimes for which the maximum pulsed radiated power is attained, the required quantities have been measured as functions of both the repetition rate and the pulse duration. Figure 2a shows the current dependence of the peak power at a fixed repetition rate for various current pulse durations. The measurements show

that the power–current curves of GaInAsSb LEDs at high pumping levels saturate for current pulses with durations greater than 50–100 μs. For shorter pulses the power output of the diode increases as the current is increased up to 2 A. In this current range the slope of the power–current curves begins to change for any pulse durations and depends on the current amplitude. To maximize the peak power, we have investigated the dependence of the power output on the repetition rate at a fixed pulse duration of 1 μs. The results are shown in Fig. 2b. The investigations show that saturation begins to set in at frequencies of the order of 20–30 kHz. The attained maximum optical power is 90 mW at 2 A, 1 μs, and 1 kHz. The illustrated power characteristics exhibit the strong dependence of the optical power output of LEDs made from narrow-gap compounds on the off-duty cycle (relative time between pulses) of the injection current and the parameters of the pump pulse. We note that the GaAlAsSb/GaInAsSb/GaAlAsSb semiconductor heterostructure is characterized by large discontinuities of the conduction band, their magnitude being comparable with the width of the band gap of the active zone. Consequently, as has been shown previously,[7] the parameters of the injection current in such heterostructures must depend strongly on the current heating of the active zone. The actual temperature of the active zone is a decisive factor in the acceleration of nonradiative recombination processes in LEDs utilizing them and limits the attainable power.

We have thus created LEDs with 5.5% quantum efficiency emitting at a wavelength of 1.94 μm with spectra having a FWHM of 0.12 μm for moisture measurement applications. A CW optical power of 3.7 mW has been attained for diodes utilizing a GaAlAsSb/GaInAsSb/GaAlAsSb double heterostructure. At room temperature it has been shown that a maximum peak optical power of 90 mW can be attained by pumping with pulses of duration $\sim 1-5$ ms and a repetition rate of 1 kHz. We have given the principal electrical and emitting characteristics and optimized them from the standpoint of spectral applications.

[1] L. S. Rothman, R. R. Gamache, R. H. Tipping, C. P. Rinsland, M. A. H. Smith, D. C. Benner, V. Malathy Devi, J.-M. Flaud, C. Camy-Peyret, A. Goldman, S. T. Massie, L. R. Brown, and R. A. Toth, J. Quant. Spectrosc. Radiat. Transfer **48**, 469 (1992).

[2] A. N. Baranov, Yu. P. Yakovlev, A. N. Imenkov, M. P. Mikhailova, A. L. Klementenok, and V. Shutov, Paper Ind. **8**, 20 (1989).

[3] J. P. Cravder, S. D. Smith, T. Ashley, and C. C. Philips, in *Abstracts of the International Conference on Mid-Infrared Optoelectronics, Materials and Devices* (Lancaster, UK, 1996).

[4] M. R. Murti, B. Grietens, C. Van Hoof, and G. J. Borghs, J. Appl. Phys. **78**, 578 (1995).

[5] A. A. Andaspaeva, A. N. Baranov, A. Guseĭnov, A. N. Imenkov, N. M. Kolchanova, E. A. Sidorenkova, and Yu. P. Yakovlev, Pis'ma Zh. Tekh. Fiz. **15**(18), 71 (1989) [Sov. Tech. Phys. Lett. **15**, 734 (1989)].

[6] A. Popov, V. Sherstnev, Yu. Yakovlev, A. Baranov, and C. Alibert, Electron. Lett. **30**, 86 (1997).

[7] N. M. Kolchanova, A. A. Popov, G. A. Sukach, and A. B. Bogoslovskaya, Semiconductors **28**, 1137 (1994).

Translated by James S. Wood

Edited by David L. Book

Long-range effects in ion-implanted silicon–silicon-dioxide structures

A. P. Baraban and L. V. Malyavka

Scientific-Research Institute of Physics at the St. Petersburg State University
(Submitted 4 April 1997)
Pis'ma Zh. Tekh. Fiz. **23**, 26–31 (October 26, 1997)

The properties of electrically active centers formed in $Si–SiO_2$ structures as a result of argon ion implantation in the oxide layer are investigated, along with the processes of defect formation in the ion-implanted structures due to subsequent, less-energetic, external (e.g., field) influences. The investigations are carried out by electrophysical and electroluminescence methods in an electrolyte–insulator–semiconductor system at room temperature. It is established that argon ion implantation in the bulk of the oxide layer leads to the formation of electrically active centers outside the zone of localization of the implanted argon ions, and a model of their formation is proposed. © *1997 American Institute of Physics.* [S1063-7850(97)02210-6]

Ion implantation is of major interest both in regard to its utilization for fundamental research on amorphous materials and from the viewpoint of its broad technological applications in modern microelectronics. However, despite myriad investigations using a diversity of techniques,[1–3] there are still many vague issues surrounding the nature and properties of defects encountered in $Si–SiO_2$ structures as a result of ion implantation. The objective of the present study is to investigate the properties of electrically active centers formed in $Si–SiO_2$ structures as a result of argon implantation in the oxide layer. We have investigated electrically active centers formed in the structures by ion implantation, along with the processes of defect formation in ion-implanted structures as a result of subsequent, less-energetic, external (e.g., field) influences.

The objects of investigation were $Si–SiO_2$ structures prepared by the thermal oxidation of KÉF-5 (100) silicon in moist oxygen at a temperature of 950°C. The oxide layer had a thickness of 250 nm. Argon implantation (dosage interval $D=10^{13}$–3.2×10^{17} cm^{-2}) was carried out on an Eaton Nova 4206 apparatus with cooling and a low beam density to avoid heating of the target. The ion energy was chosen so that the maximum of the distribution of implanted ions would occur in the middle of the oxide layer; the value of the maximum was 130 keV. The properties of the electrically active centers were investigated by means of an electrolyte–insulator–semiconductor system and procedures specially developed for it: the electroluminescence method and electrophysical methods — field cycling and layer profiling — based on measurements of the rf capacitance–voltage curves in the electrolyte–insulator–semiconductor system.[4,5] All the measurements were carried out at room temperature.

Figure 1 shows the electroluminescence spectra of a comparison control structure and the ion-implanted $Si–SiO_2$ structures. It is evident that ion implantation produces a strong electroluminescence band at 2.7 eV, which has been shown previously to be associated with the existence of unsaturated Si–O bonds in the bulk of the oxide layer.[4] In addition, there is an observable increase in the intensity of the electroluminescence band at 1.9 eV, whose presence in the spectrum is attributable to the existence of silane groups in the oxide layer.[4] An analysis of the spectra shows that the intensities of these electroluminescence bands increase as the argon implantation dose is increased to 10^{15} cm^{-2} and then remains constant up to a dose of 10^{17} cm^{-2}. It is important to note in this connection that etching of the oxide layer to a thickness of 120 nm does not bring about any appreciable reduction in the intensity of the 2.7-eV electroluminescence band, indicating that the luminescence centers responsible for it are localized in an oxide layer of the corresponding thickness.

The investigations of the ion-implanted structures on the basis of the capacitance–voltage curves show that argon implantation ($D=10^{13}$ cm^{-2}) leads to the formation of an effective (without regard for the centroid) positive charge in the bulk of the oxide layer and increases the total density of surface states in the band gap of silicon due to the increased density of the continuous spectrum and to the emergence of a discrete density-of-states maximum located at 0.30 ± 0.05 eV from the bottom of the silicon conduction band. An increase in the implantation dose tends to decrease the effective charge and further increase the density of surface states, particularly in the vicinity of the discrete maximum.

The layer profiling technique, based on the evaluation of the flat-band potential (V_{fb}) as a function of the thickness of the oxide layer (Fig. 2), enables us to determine the true values of the charges formed in the bulk of the oxide layer and to establish their localization zone and the positions of the centroids. The deviations of V_{fb} as a function of the thickness of the oxide layer from a linear dependence in its outer part are due to the charging of ''biographical'' (preexisting) electron traps. It is evident from Fig. 2 that significant variations in the charge state of the ion-implanted structures occur in an oxide layer closer to the $Si–SiO_2$ boundary than the zone of localization of the implanted argon. An increase in the implantation dose together with a decrease in the total positive charge causes the centroid of the latter to shift deeper into the oxide layer. Subsequent field effects acting on the ion-implanted structures in the electrolyte–insulator–semiconductor system (field cycling method[5]) show that the charge states of structures with $D=10^{13}$ cm^{-2} are essentially completely stable and that a substantial positive charge forms in the bulk of the oxide layer for structures with

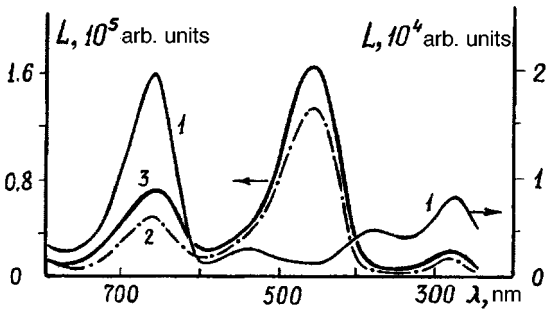

FIG. 1. Electroluminescence spectra of $Si–SiO_2$ structures. *1* — In the native state; *2, 3* — after implantation at doses of 10^{13} cm^{-2} and 10^{14} cm^{-2}, respectively.

$D=10^{14}$ cm^{-2} or higher (Fig. 2). The kinetics of the buildup of this charge and the influence of low-temperature annealing ($T=200°C$, $t=1$ h), which almost totally eradicates it, suggest that it is related to the charging of neutral hole traps, which form under the influence of ion implantation and are similar in their properties and basic nature to the biographical hole traps in $Si–SiO_2$ structures.[4]

These results lead to the conclusion that ion implantation produces significant changes in the properties of $Si–SiO_2$ structures and that these changes occur outside the zone of localization of implanted argon due to long-range effects. The slowing of argon ions is accompanied by their discharge

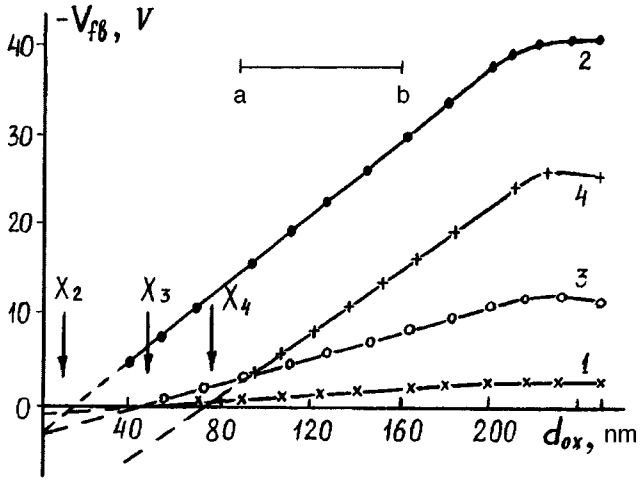

FIG. 2. Flat-band potential V_{fb} vs thickness of the oxide layer for $Si–SiO_2$ structures. *1* — Native structure; *2* — after implantation at a dose 10^{13} cm^{-2}; *3* — the same, at 10^{14} cm^{-2}; *4* — after implantation at 10^{14} cm^{-2} with subsequent field profiling; X_2, X_3, X_4 — centroids of the positive charges for curves *2–4*, respectively; [*ab*] denotes the zone of localization of the implanted argon.

and the migration of atomic and electronic excitations into the depth of the oxide layer. The resulting changes observed in the charge state of the structures as the implantation dose is increased can be attributed to the emergence of charges of both signs occupying different positions in space and having different dependences of their magnitudes on the implantation dose. At low implantation doses a positive charge is formed, its magnitude increasing with the dose and reaching saturation at doses of 10^{14} cm^{-2}. This behavior of the given charge correlates with the behavior of the intensity of the 2.7-eV electroluminescence band, indicating that its formation can be tied in with the formation near the $Si–SiO_2$ boundary of a SiO_x ($x>2$) layer saturated with positively charged $Si–O^+$ defects. We note that this hypothesis is consistent with Fourier infrared-spectroscopy data[3] on the change due to ion-implantation in the concentration of broken Si–O bonds. At doses above 10^{13} cm^{-2} the above-described process is augmented by the formation of a negative charge with two components: a charge at the discrete level of surface states and a change in the bulk of the oxide layer. The formation of the bulk negative charge is accompanied by the formation of neutral hole traps and appears to be associated with the ion-implantation-induced formation of a SiO_x ($x<2$) layer localized at a large distance from the silicon in comparison with the excess-oxygen layer, as shown in Ref. 1. In this case the appearance of the negative charge and neutral hole traps can be associated with the formation of silicon clusters characterized by the presence of unsaturated silicon bonds at their boundary with the oxide layer. Such defects lead to the formation of amphoteric states, which are capable of existing in various charge states, as shown in Ref. 6.

The proposed model can be used to explain the observed changes in the total charge, the position of its centroid, and the influence of subsequent field effects as the implantation dose is increased. However, further research will be needed before the nature of the defects and the long-range mechanisms involved in the ion implantation of argon in oxide layers on silicon can be definitively established.

[1] C. Dominguez, B. Garrido, J. Montserrat *et al.*, Nucl. Instrum. Methods Phys. Res. B **80/81**, 1367 (1993).
[2] B. Garrido, J. Samitier, J. R. Morante *et al.*, Phys. Rev. B **49**, 14845 (1994).
[3] B. Garrido, J. Samitier, S. Bota *et al.*, J. Non-Cryst. Solids **187**, 101 (1995).
[4] A. P. Baraban, V. V. Bulavinov, and P. P. Konorov, *Electronics of SiO_2 Layers on Silicon* [in Russian] (Izd. LGU, Leningrad, 1988).
[5] A. P. Baraban, V. V. Bulavinov, and A. G. Groshikhin, Pis'ma Zh. Tekh. Fiz. **19**(18), 27 (1993) [Tech. Phys. Lett. **19**, 577 (1993)].
[6] C. T. White and K. L. Ngai, J. Vac. Sci. Technol. **16**, 1412 (1979).

Translated by James S. Wood
Edited by David L. Book

MHD instabilities and the generation of ultrahigh magnetic fields

P. I. Zubkov and K. A. Ten

M. A. Lavrent'ev Institute of Hydrodynamics, Siberian Branch of the Russian Academy of Sciences, Novosibirsk

(Submitted 6 February 1997)
Pis'ma Zh. Tekh. Fiz. **23**, 32–36 (October 26, 1997)

Methods are proposed for generating magnetic fields in connection with the intentional generation and development of force instabilities of a current-carrying plasma channel. © *1997 American Institute of Physics.* [S1063-7850(97)02310-0]

The feasibility of generating high-intensity electrical pulses in the excitation of magnetohydrodynamic (MHD), or force, instabilities of a current-carrying plasma column has been discussed previously.[1] It was shown that the maximum emf of electromagnetic induction, which greatly exceeds the initial voltage in the storage device, is bounded in the generation of screw instabilities. The emf of the electromagnetic induction is unbounded in the generation of kinks in a noncylindrical *Z*-pinch.

It has been shown[2] that kink generation can be achieved by the specification of certain initial and boundary conditions. The generation of helical instabilities can be implemented analogously.

Figure 1 shows an experimental arrangement in which the excitation and development of a helical instability has resulted in the formation of a plasma solenoid. A helical filament *2* is formed from the inner surface of the plastic cylinder *1*. A solid fluoroplast (Teflon-like) rod *3*, with aluminum foil *4* deposited on it, is tightly fitted into this cylinder. The whole unit is placed in a conducting cylinder *5*, which serves as a reverse-current conductor. The cylinder *5* is split lengthwise to prevent azimuthal currents from being generated in it. The current in the circuit and the derivative of the magnetic field induction are measured by the sensor *6* placed on the axis of the fluoroplast rod.

Figure 2 shows an oscillogram of the discharge, where the upper trace represents the current in the circuit (amplitude 180 kA, sweep rate 10 μs/interval), and the lower trace represents the derivative of the magnetic induction in the center of the rod. The discharge is initially cylindrically symmetric, and no axial magnetic field exists on the discharge axis. When the foil explodes under the influence of the flowing current, a plasma channel is formed. It is unstable against an increase in the inductance, and a helical instability develops in it, inducing an axial magnetic field, which shows up on the lower trace. The current and the magnetic field change form, and a plasma solenoid is formed with an axial magnetic field generated along its axis. The wavelength λ of the helical instability can be predetermined by the boundary conditions. In the reported experiments λ was specified by the pitch of the helical channel.

We now estimate possible values of the generated magnetic fields during the evolution of force instabilities of the plasma column. The term *force instabilities* nicely characterizes the physics of the phenomenon and is borrowed from Aleksandrov and Rukhadze.[3] We consider the plasma to be ideally conducting. This assumption is valid when the characteristic time of evolution of the instabilities is much shorter than the discharge period, as is generally the case. Here the current in the circuit I at the instant when the inductance of the plasma channel becomes equal to L owing to the development of force instabilities, can be determined from the conservation of magnetic flux:

$$L_0 I_0 = (L_0 + L) I,$$

where L_0 and I_0 are the inductance and the maximum current in the undeformed loop. The initial inductance of the plasma column is much lower than L_0 and can therefore be disregarded.

By trial and error it is always possible to achieve the onset of instabilities at near-maximum current, as observed experimentally (Fig. 2).

When a plasma solenoid is formed, the induction of the axial magnetic field B at a helical-instability wavelength λ much shorter than the distance l between electrodes is given by the expression

$$B \approx \frac{4\pi}{c} \frac{I}{\lambda}.$$

The inductance L in this approximation is

$$L \approx \frac{4\pi^2 r^2 l}{\lambda^2},$$

where r is the initial radius of the discharge channel. For the magnetic induction B we then obtain the expression

$$B \approx \frac{4\pi}{c} L_0 I_0 \frac{\lambda}{L_0 \lambda^2 + 4\pi^2 r^2 l},$$

which has a maximum at $\lambda = (\pi^2 r^2 l / L_0)^{1/2}$. The channel inductance in this case is $L = L_0$.

The maximum induction $B_{\max}$ can be written in the form $B_{\max} = \frac{1}{2} B_0 \sqrt{L_0 / l} = B_0 \pi r / \lambda$, where B_0 is the induction of the azimuthal magnetic field on the surface of the cylinder before the onset of the helical instability at the maximum current. if $L_0 \gg l$ or $r \gg \lambda$, we have $B_{\max} \gg B_0$.

When kinks form in a noncylindrical *Z*-pinch, following Ref. 4, we simplify the calculation of the inductance L of the plasma column by assuming that it is a step function. We consider a plasma column of length λ equal to the wavelength of the perturbation. The radius of the kink at a distance $\lambda/2$ from the top of the column is equal to $r - \delta$, where

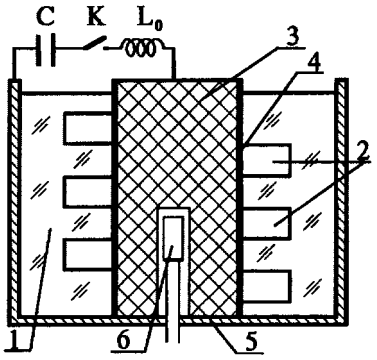

FIG. 1.

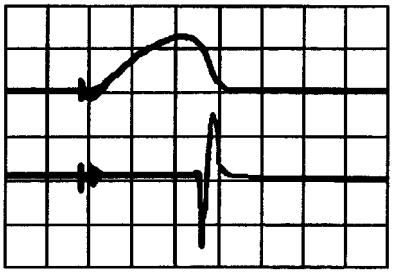

FIG. 2.

r is the equilibrium radius, and δ is a perturbation. In the lower half of the column the radius of the kink is $r+\delta$. In this approximation the external inductance of a plasma column of length λ is

$$L=\lambda \ln \frac{R^2}{r^2-\delta^2},$$

where R is the radius of the outer current conductor. We obtain the following equation for the induction of the magnetic field in the kink:

$$B=\frac{2I}{c(r-\delta)}=\frac{2L_0I_0}{c(r-\delta)}\left(L_0+\lambda \ln \frac{R^2}{r^2-\delta^2}\right)^{-1}.$$

The constriction in the kink is unbounded in the MHD approximation,[2,5] and the above equation therefore has the formal implication that $B\to\infty$ in the limit $\delta\to r$. Consequently, the magnetic induction can be unbounded in the kink. In regard to the space in which a strong magnetic field is generated, we have shown[2] that it can be fixed by the initial and boundary conditions.

For a cylindrical Z-pinch, when it is possible for a train of heteropolar, high-intensity electrical pulses to be generated,[6] a train of magnetic field pulses can be generated as well. In this case

$$B_{\max}=B_0 \frac{RL_0}{r_0(L_0+l \ln(R/r_0))}\approx B_0 \frac{R}{r_0},$$

where r_0 is the stopping radius of the cylindrical Z-pinch. For $R\gg r_0$ the maximum induction $B_{\max}$ can be much higher than B_0.

These estimates show that force instabilities can be used to generate strong and ultrastrong magnetic fields; in other words they are not always harmful and can even be useful.

This work has received partial financial support from the Russian Fund for Fundamental Research, Grant No. 95-02-04411.

[1] P. I. Zubkov, Prikl. Mekh. Tekh. Fiz., No. 4, 24 (1993).
[2] P. I. Zubkov, S. M. Ishchenko, and K. A. Ten, in *Proceedings of the Seventh International Conference on the Generation of Megagauss Magnetic Fields and Related Experiments* [in Russian] (Sarov, Arzamas Province, 1996), pp. 41–42.
[3] A. F. Aleksandrov and A. A. Rukhadze, *Physics of High-Current Electrical-Discharge Light Sources* [in Russian] (Atomizdat, Moscow, 1976).
[4] V. V. Vikhrev and S. I. Braginskiĭ, in *Reviews of Plasma Physics*, Vol. 10, edited by M. A. Leontovich (Consultants Bureau, New York, 1986) [Russ. original, Atomizdat, Moscow, 1980], pp. 243–248.
[5] V. F. D'yachenko and V. G. Imshennik, in *Reviews of Plasma Physics*, Vol. 8, edited by M. A. Leontovich (Consultants Bureau, New York, 1980) [Russ. original, Atomizdat, Moscow, 1974], pp. 164–176.
[6] P. I. Zubkov, D. Yu. Golubenko, and K. A. Ten, in *Proceedings of the Seventh International Conference on the Generation of Megagauss Magnetic Fields and Related Experiments* [in Russian] (Sarov, Arzamas Province, 1996), p. 42.

Translated by James S. Wood
Edited by David L. Book

Dual-wavelength superfluorescent fiber emitter

É. I. Alekseev, E. N. Bazarov, Yu. A. Barannikov, V. P. Gapontsev, V. P. Gubin, I. E. Samartsev, and N. I. Starostin

Institute of Radio Engineering and Electronics, Russian Academy of Sciences, Fryazino
(Submitted 15 April 1997)
Pis'ma Zh. Tekh. Fiz. **23**, 37–42 (October 26, 1997)

The feasibility of constructing a dual-wavelength, spatially single-mode, superfluorescent fiber emitter on the basis of erbium optical fibers with pumping by multimode semiconductor lasers is demonstrated. The emitter is fabricated by all-fiber technology and has a power output in excess of 10 mW, an average emission wavelength of 1.54 μm, and a spectral resolution of 27.5 nm at component linewidths of 3 nm and 9 nm. The depolarization of the radiation from the emitter as it propagates in an anisotropic, single-mode fiber waveguide is investigated.
© *1997 American Institute of Physics.* [S1063-7850(97)02410-5]

Single-mode superfluorescent fiber emitters enjoy widespread applications in fiber-optic communications, fiber-optic sensors, low-coherence interferometry, and other areas of present-day optoelectronics.[1,2] Until recently, attention has been focused primarily on the development and investigation of superfluorescent fiber emitters with a single broad emission line. Equally interesting, however, are superfluorescent fiber emitters that emit two (or more) broad, well-resolved lines. Such superfluorescent fiber emitters are required, for example, for communication lines with spectral separation of the channels, for multiwavelength, low-coherence sensors,[3] for low-coherence, high-resolution spectrometry,[4] and other applications.

Today the problem of multiwavelength, low-coherence radiation emitters is solved mainly by a judicious combination of several multimode semiconductor lasers.[4] This approach, however, has a number of inherent shortcomings due to the multimode structure of the radiation from the synthesized emitters, along with the low stability of their parameters. Consequently, the development of multiwavelength superfluorescent fiber emitters, which boast several advantages over combination semiconductor laser sources (high power output, higher temperature stability of their parameters, simplicity of coupling with single-mode optical fibers, etc.), has become a crucial problem in recent times. In particular, Wang *et al.*[5] have reported the development of a dual-wavelength superfluorescent radiation emitter utilizing a fiber doped with samarium ions and emitting in the visible wavelength range.

Here we demonstrate the possibility of constructing a dual-wavelength superfluorescent fiber emitter using quartz fibers doped with erbium and ytterbium ions, with a power output of the order of 10 mW and an emission spectrum lying in the 1.55-μm range and consisting of two well-resolved lines of width 3 nm and 9 nm, their maxima separated by a distance of approximately 27.5 nm. The dual-wavelength superfluorescent fiber emitter is designed on the basis of the dependence of the superfluorescent spectrum at the output of the activated fiber segment on its length, the concentration of erbium ions, the pump wavelength, and the distribution of the pump power along the length of the activated fiber segment. By varying these parameters it is possible to adjust the relative sizes of the maxima in the superfluorescent spectrum of the erbium ions in the vicinity of 1.535 μm, 1.543 μm, and 1.565 μm.

The optical schematic of the dual-wavelength superfluorescent fiber emitter is shown in Fig. 1 and essentially consists of two superfluorescent fiber emitters SFE1 and SFE2 consolidated into a unit whole, their emission spectra having maxima near 1.535 μm and 1.565 μm, respectively. The emission line with its maximum in the vicinity of 1.535 μm is formed by SFE1, which is fabricated from an activated fiber segment AF1 of length 3 m, and the line with its maximum at a wavelength of 1.565 μm is emitted by SFE2, which is fabricated from segments AF2 and AF3 with a total length of 15 m. To create a more uniform distribution of the pump power along the length of AF2 and AF3, two laser diodes (LD2 and LD3) are used for the pump.

The phosphate-silicate activated fiber used to construct the superfluorescent fiber emitters has a single-mode core doped with erbium and ytterbium ions at concentrations of 0.1 wt.% and 2 wt. %, respectively. The cutoff wavelength of the highest mode is 1.1 μm.

The activated fibers are pumped by multimode laser diodes with a wavelength of 965 nm through directional coupler multiplexers (DCM). The selected pump wavelength corresponds to the mildly sloping part of the absorption spectrum of ytterbium ions, substantially reducing the temperature dependence of the emitter output parameters. Optical isolators (OI) are used to diminish the influence of optical feedback on the parameters of the superfluorescent fiber emitters.

The radiation from SFE1 and SFE2 are summed at the common output by means of a single-mode directional coupler (DC). To achieve more complete resolution of the lines and filtering out of the spectral component at 1.543 μm, the radiation from SFE1 passes through a spectral filter (SF), which in this case is a single-mode directional coupler.

The emission spectrum of the dual-wavelength superfluorescent fiber emitter is shown in Fig. 2. The maxima of the lines correspond to wavelengths $\lambda_{01}=1535.2$ nm and $\lambda_{02}=1562.7$ nm, so that the distance between them is $\Delta\lambda_{12}=27.5$ nm. The widths of the lines at the half-maximum are $\Delta\lambda_1\simeq 3$ nm and $\Delta\lambda_2\simeq 9$ nm, respectively. The average

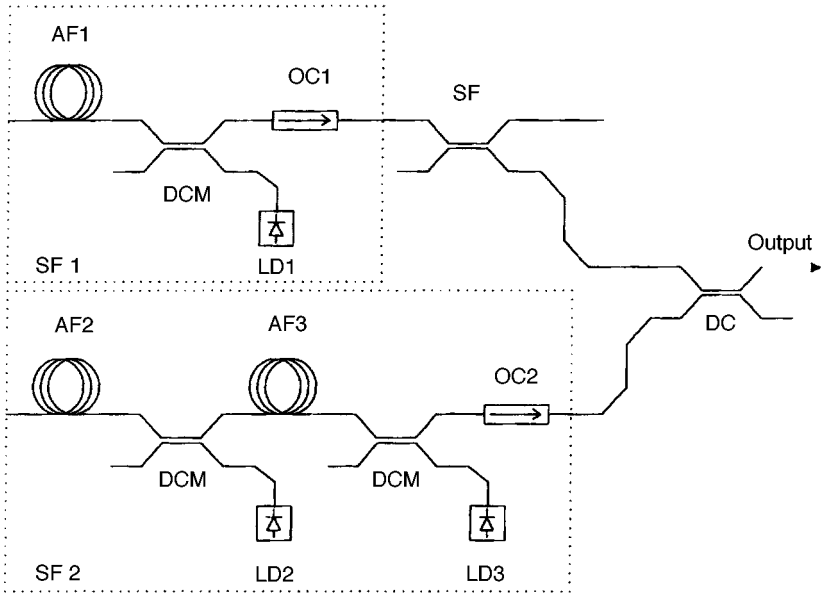

FIG. 1. Schematic of the dual-wavelength superfluorescent fiber emitter.

power outputs measured with SFE1 and SFE2 activated in succession are $P_1=5$ mW and $P_2\simeq 15$ mW. The emitter parameters can be varied within wide limits by varying the operating regimes of the laser diodes and the characteristics of the directional coupler and the directional coupler multiplexers. The residual degree of polarization of the radiation from the given dual-wavelength superfluorescent fiber emitter is determined by the polarization characteristics of the optical isolator, the spectral filter, and the directional coupler; in our case it does not exceed 5%.

We have investigated the salient characteristics of the depolarization of radiation from the dual-wavelength superfluorescent fiber emitter as it propagates along an anisotropic, single-mode optical fiber; this information has important bearing on fiber gyroscopes, low-coherence interferometry, and several other applications. The procedure of Ref. 6 was used to measure the degree of polarization $p(L)$ of the radiation at the output of a segment of the anisotropic, single-mode optical fiber of length L when radiation from the dual-wavelength superfluorescent fiber emitter, linearly polarized at a 45° angle with the birefringence axes of the anisotropic, single-mode optical fiber, is coupled into the latter. The graph of $p(L)$ is shown in Fig. 3. The dashed curve in this figure corresponds to the empirical relation

$$p(L)=\frac{1}{1+\varepsilon}\exp(-L/L_d)[1+\varepsilon\cos(2\pi L/L_{12})] \qquad (1)$$

with parameters $\varepsilon=0.6$, $L_d=50$ cm, and $L_{12}=25$ cm. An analysis of the results shows that $L_{12}=L_p\Delta\lambda_{12}/\lambda_0$, where $L_p=4.4$ mm is the length of the polarization beats of the

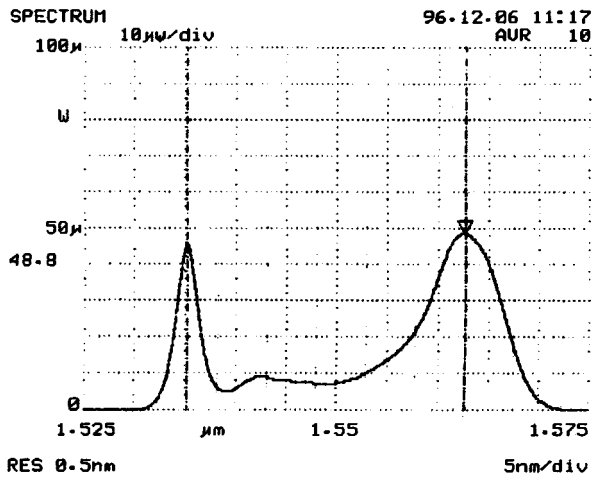

FIG. 2. Emission spectrum of the dual-wavelength superfluorescent fiber emitter (power output in μW vs wavelength in μm). Resolution of the spectrum analyzer, 0.5 nm.

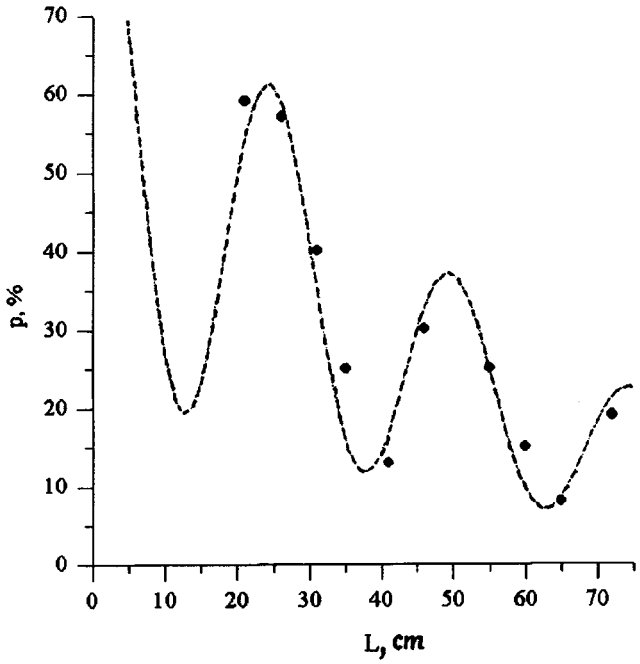

FIG. 3. Degree of polarization of radiation from the dual-wavelength superfluorescent fiber emitter vs length of the segment of the anisotropic, single-mode optical fiber (the dashed curve represents the calculated dependence).

anisotropic, single-mode optical fiber, and $\lambda_0=(\lambda_{01}+\lambda_{02})/2$. The quantity $L_d \simeq kL_p\Delta\lambda/\lambda_0$ corresponds to the depolarization length in the given anisotropic, single-mode optical fiber of radiation with a single Gaussian line of width $\Delta\lambda$, where $\Delta\lambda=(\Delta\lambda_1+\Delta\lambda_2)/2$, and the coefficient $k\simeq 0.44$. Consequently, the degree of polarization of the radiation from the dual-wavelength superfluorescent fiber emitter in the anisotropic, single-mode optical fiber exhibits an oscillatory behavior.

In closing, we point out that estimates based on equations in Ref. 4 show that the given dual-wavelength superfluorescent fiber emitter can be used in white-light interferometers to improve their resolving power by roughly an order of magnitude.

The authors are indebted to V. V. Fomin for assistance and valuable discussions.

This work has received partial support from the State Scientific-Technical Committee Fund, Project No. 2.4 on Optics and Laser Physics.

[1] P. F Wysocki, M. J. F. Digonnet, V. J. Kim, and H. J. Shaw, J. Lightwave Technol. **LT-12**, 550 (1994).
[2] É. I. Alekseev, E. N. Bazarov, V. P. Gapontsev *et al.*, Radiotekh. Élektron. **41**, 759 (1996).
[3] A. D. Kersey *et al.*, Proc. SPIE **719**, 135 (1986).
[4] D. N. Wang, Y. N. Ning, K. T. V. Grattan *et al.*, Appl. Opt. **33**, 7326 (1994).
[5] D. N. Wang, B. T. Meggitt, A. W. Palmer *et al.*, IEEE Photonics Technol. Lett. **PTL-7**, 620 (1994).
[6] É. I. Alekseev, E. N. Bazarov, G. A. Gerasimov *et al.*, Pis'ma Zh. Tekh. Fiz. **21**(23), 89 (1995) [Tech. Phys. Lett. **21**, 990 (1995)].

Translated by James S. Wood
Edited by David L. Book

Hydrogen-pellet injector using a screw extruder

I. V. Vinyar, S. V. Skoblikov, and P. Yu. Koblents

St. Petersburg State Technical University
(Submitted 14 May 1997)
Pis'ma Zh. Tekh. Fiz. **23**, 43–46 (October 26, 1997)

The first injector design capable of injecting an unlimited supply of fuel pellets into a fusion reactor plasma in prolonged, continuous operation is reported. More than a thousand pellets 2 mm in diameter are formed without interruption from the screw extruder at frequencies of 1 Hz and 2 Hz and are accelerated to 0.8 km/s. © *1997 American Institute of Physics.* [S1063-7850(97)02510-X]

The fusion reaction in thermonuclear devices is maintained by fuel injectors, which shoot pellets of solid hydrogen isotopes into the plasma at frequencies from 1 Hz to 40 Hz (Refs. 1 and 2). The continuous operation of these injectors lasts only a few seconds, being limited by the supply of solid hydrogen prefrozen in the extruder of the injector. Using two or more extruders for continuous injection or increasing the fuel supply in the extruder is discouraged by safety considerations, particularly when working with tritium.

The first injector design capable of sustaining the prolonged and continuous generation and acceleration of fuel pellets is based on the familiar screw extruder used in the plastics industry.[3] A gas is fed into the extruder of the fuel injector; the temperature of the latter is approximately 10 K, and as the gas progresses along the screw channel, it is converted initially into liquid and then to ice. This process is feasible because the temperature interval between the liquid and solid plastic state of the hydrogen isotopes is only 5–10 K. However, the possibility of the screw squeezing the solid hydrogen in a stable regime to the (5–20) MPa level required for extrusion[1,2,4] calls for experimental verification. We have constructed an injector for this purpose, which is shown schematically in Fig. 1. Its main components are the high-vacuum chamber *1* housing the extruder *2* with the open-cycle heat exchanger *3* and the screw *4*, which are connected outside the chamber to the motor *5*, the accelerating-gas feed valve *6*, the electromagnetic drive *7* used to transfer the pellets into the barrel *8*, and the diagnostic chamber *9*. Connected to the exit orifice of the extruder is the transparent chamber *10*, which is equipped with a vacuum pump *11* and a linear scale for visually observing and measuring the length of the solid-hydrogen rod. The extruder has a length of 150 mm and consists of a cylindrical chamber with an inside diameter of 12 mm; a helical heat-exchanger channel is cut into its outer surface. Two semiconductor temperature sensors are mounted in the upper and lower parts of the extruder. A 30-W heating coil is wound around the length of the extruder.

The primary concern in the first stage of the experimental work was to obtain a stable extrusion regime. The extruder temperature was held constant in the interval 10–13 K by regulating the helium flow and the heater power. Prior to the start of extrusion, hydrogen at a pressure below 0.1 MPa was pumped into the extruder, in which it was then frozen. The screw was rotated either by the motor or manually at a rate of 10–80 rpm. After 2–10 s from the start of rotation of the screw the solid-hydrogen rod was located inside the viewing chamber, where it was photographed and video-recorded. The transparency of the solid-hydrogen rod attested to its high quality.

The extrusion rate was calculated from the speed at which the end of the rod traversed a scale of length 6 cm with five-millimeter divisions, attached to the wall of the viewing chamber. The maintenance of the extrusion regime was most stable when the screw was rotated at a speed of 15 rpm. The dependence of the extrusion rate on the temperature of the hydrogen rod for this regime is shown in Fig. 2. The hydrogen was extruded continuously at a rate of approximately 20 mm/s and temperature of 11 K for more than 30 min, until the solid hydrogen filled up the volume of the viewing chamber. After evacuation of the latter, extrusion was immediately resumed by starting up the rotation of the screw. The total extrusion period yielded a hydrogen rod more than 50 m in length, from which more than 12,000 pellets having a characteristic length of 2 mm were formed exclusive of waste allowance at the cuts. At no time did the amount of solid hydrogen in the extruder exceed 5 cm^3. This fact bears witness to the high efficiency and attractiveness of such an injector for continuously maintained reactor fueling, because the mass of tritium in the injector would be less than 2 g.

The objective of the second experimental stage was to demonstrate the feasibility of producing and accelerating pellets indestructibly in a continuous frequency regime, and also to photograph them. Once the rod had appeared in the viewing chamber, the electromagnetic drive rapidly pushed a thin-walled tube toward the rod and, thereby cutting off part of the rod, transferred the newly formed pellet in the barrel of diameter 2.4 mm. Next, compressed helium at a pressure of 2–4 MPa was delivered from the pulse-actuated valve and accelerated the pellet in the barrel. At 0.05 s after the shot, the drive returned the tube to its starting position, and the hydrogen rod continued to be forced into the viewing chamber without any visible delay or degradation of the ice. We were thus able to confirm that the driving gas has almost scarcely any influence on the stability or rate of extrusion. In the first experiments shots were fired at frequencies of 1 Hz and 2 Hz. More than a thousand pellets were formed and accelerated up to 0.6–0.8 km/s without interruption. None of

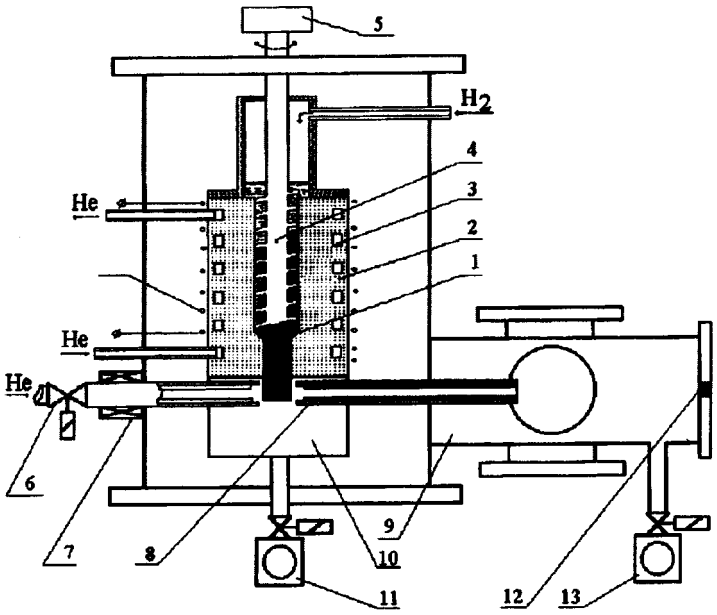

FIG. 1. Schematic of the fuel-pellet injector with screw extruder.

the photographed pellets showed any traces of damage in the photographs. Experiments are currently being set up to test the injection of pellets at frequencies up to 10 Hz from a deuterium-hydrogen mixture.

The proposed and experimentally tested method of producing fuel pellets by means of a screw extruder has the hypothetical capability for solving the problem of building a reliable system for the prolonged, continuous fueling of fusion reactor plasmas. One extruder of this type meets all present-day fuel-injection system requirements for reactors of the ITER (International Thermonuclear Experimental Reactor) class in regard to pellet forming and is distinguished by its exceptional simplicity and reliability, as well as the small reserve of hydrogen isotopes in the injector. An increase in the extrusion rate can be expected following the completion of ongoing mathematical modeling and experiments.

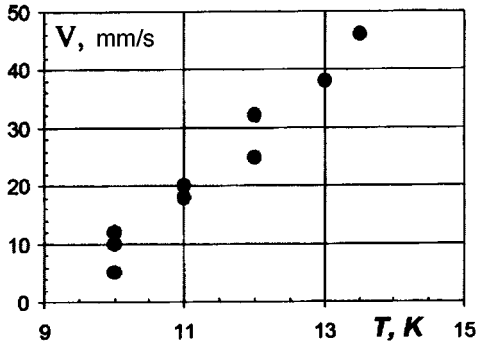

FIG. 2. Extrusion rate V vs temperature of the hydrogen rod T at a screw rotation speed of 15 rpm.

[1] S. L. Milora, W. A. Houlberg, L. L. Lenguel, and V. Mertens, Nucl. Fusion **35**, 657 (1995).
[2] S. K. Combs, Rev. Sci. Instrum., **64**, No. 1679 (1993).
[3] D. D. Ryabinin and Yu. E. Lukach, *Screw Machines for the Processing of Plastics and Rubber Mixtures* [in Russian] (Mashinostroenie, Moscow, 1965).
[4] I. V. Vinyar, B. V. Kuteev, S. V. Skoblikov *et al.*, Zh. Tekh. Fiz. **65**(7), 167 (1995) [Tech. Phys. **40**, 723 (1995)].

Translated by James S. Wood
Edited by David L. Book

Multinozzle gas-dynamic molecular-beam source

V. V. Yashchuk, V. F. Ezhov, G. B. Krygin, and V. L. Ryabov

St. Petersburg Nuclear Physics Institute, Gatchina, Russia
(Submitted 6 March 1997)
Pis'ma Zh. Tekh. Fiz. **23**, 47–54 (October 26, 1997)

The results of an experimental investigation of a multinozzle gas-dynamic molecular-beam source, in which the working material is introduced directly into a supersonic jet of a buffer gas, are presented. The source is designed to create slow cold beams of atoms and molecules. Time-of-flight profiles of the beams of the N_2 buffer gas and the working material SF_6 formed by a source with six nozzles are presented. The measured parameters of the flow field of the buffer gas are compared with the results of calculations for an axisymmetric nozzle with an inner body having an annular critical cross section. The results obtained show that multinozzle designs can be used, in principle, in molecular-beam sources instead of axisymmetric nozzles with an inner body. This permits relaxation of the requirements placed on the accuracy needed in fabricating such sources, reduction of the buffer gas flow rate, and the employment of fairly simple schemes for recycling the buffer gas. © *1997 American Institute of Physics.* [S1063-7850(97)02610-4]

One of the most effective methods for obtaining cold beams of nonvolatile molecules and radicals is based on the technique of reducing the phase volume of an atomic beam.[1] The idea behind this method is to introduce a vapor of the working material directly into a supersonic jet of a buffer gas. During thermalization of the vapor of the working material and the buffer gas, which cools as a result of supersonic expansion, their translational velocities and temperatures become equal, reaching the values determined by the large quantity of the buffer gas. The temperatures corresponding to the internal, i.e., vibrational and rotational, degrees of freedom decrease simultaneously. As a result, there is narrowing not only of the velocity and angular distributions of the molecules in the beam emitted, but also of their distribution among quantum states.

The first and, as yet, the only molecular-beam source that implements the method described was constructed in the St. Petersburg Nuclear Physics Institute of the Russian Academy of Sciences in 1986 to obtain a beam of PbI radicals.[2] In that source a supersonic flow of the buffer gas (nitrogen) is formed by an axisymmetric Laval nozzle with an inner body. The critical cross section of the nozzle has the form of a ring with a gap measuring about 0.1 mm. The vapor of the working material is introduced into the supersonic nitrogen flow in the heated capillary tube through a hollow inner body.

A significant shortcoming of the design of this source was discovered already during the tests that confirmed the efficiency of the method. The fact is that it is practically impossible to achieve a uniform gap in the critical cross section when the nozzle is fabricated. The nonuniformity of the gap leads to problems in aligning the source, since its optical and gas-dynamic axes do not coincide. In addition, when the critical cross section has an annular shape, the possibilities for optimizing the source by profiling the nozzle are restricted because of the increase in the radius of the critical cross section.[3] At a fixed gap this leads to an unjustified increase in the total buffer gas flow rate through the nozzle and, consequently, makes the already stringent requirements placed on the vacuum system of the source even harder to meet. It is especially important to minimize the total flow rate in work with an expensive gas, such as, for example, xenon,[4,5] where the buffer gas must be collected, purified, and recycled.

To solve the problems just indicated, in Ref. 6 we proposed using a multinozzle design of a source consisting of a set of nozzles evenly spaced around the circumference of the critical cross section. The total buffer gas flow rate in this case is determined by the number of nozzles and the critical cross section of each individual nozzle. The advantages of the proposed scheme are obvious.

The main purpose of the present work is to demonstrate the possibility, in principal, of using multinozzle sources to form molecular beams. The results of an experimental investigation of a source with six axisymmetric Laval nozzles, which is depicted schematically in Fig. 1, are presented below.

The experiments were performed on the molecular-beam generator facility of the St. Petersburg Nuclear Physics Institute using a cross-correlation time-of-flight (TOF) spectrometer.[7,8]

The source under investigation is installed in the molecular-beam generator on a five-coordinate alignment stage in a vacuum chamber with a diameter of 90 cm. Three NVBM-15 booster pumps with a total throughput of 4×10^4 to 5×10^4 l/s at a residual pressure of $0.1-1$ Pa provide for the continuous operation of the source with buffer gas flow rates up to 4×10^4 Pa·l/s. A beam consisting of a mixture of the buffer gas and the working material is formed from the near-axial part of the flow by two skimmers and two diaphragms arranged in succession with a differential pumping system between them. A monopole mass spectrometer with electron-impact ionization serves as the detector.

The alignment stage is intended for automated displacement of the source along the three Cartesian coordinates and two angular coordinates and is used to find the optimum position of the source relative to the skimmer, i.e., the posi-

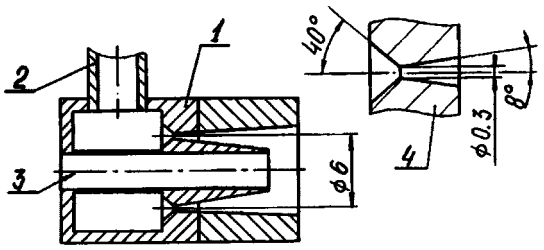

FIG. 1. Six-nozzle molecular-beam source: *1* — body of a nozzle with an inner body, *2* — connecting pipe for supplying the buffer gas, *3* — channel in the inner body for supplying the working material, *4* — configuration of one of the six nozzles.

tion corresponding to the intensity maximum of the beam formed. In addition, measurements of the spatial distributions of the parameters of the flow containing the buffer gas and the working material were performed using the alignment stage.

Time-of-flight profiles were measured in the experiment for the beams of the N_2 and Xe buffer gases and the working material SF_6 formed by the six-nozzle source. The dependence of the principal parameters of the beams on such formation conditions as the pressure in the nozzle reservoir (the backing pressure) P_0, the working pressure of SF_6 at the entrance to the capillary tube of the inner body, and the spatial position and angular orientation of the source relative to the first skimmer was investigated. The purpose of these investigations was to determine the optimum formation conditions. Figure 2 presents typical TOF profiles for this source. The similarity between the profiles for the beams of SF_6 and the buffer gas corresponding to it is a result of the thermalization process. A comparison of these profiles with the TOF profile for a SF_6 beam obtained in the absence of a buffer gas also graphically demonstrates the effectiveness of the source. We note that the working pressure of SF_6 in this source is chosen in the range $10-100$ Pa. At such pressures

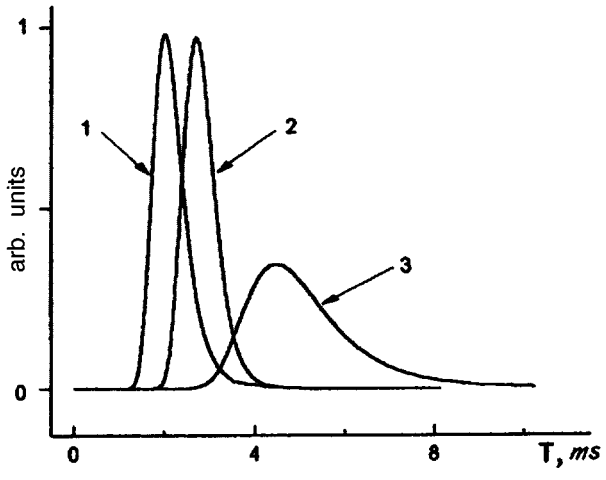

FIG. 2. Time-of-flight profiles of beams of the N_2 buffer gas $[P_0(N_2)=1\times10^4$ Pa] (*1*) and of the working material SF_6 $[P_0(SF_6)=1\times10^2$ Pa] (*2*). Time-of-flight profile of a SF_6 beam obtained in the absence of a buffer gas (*3*). Profiles *1*, *2*, and *3* are described by a Maxwellian velocity distribution with velocity ratios $S=V/\alpha$ equal to 3.7, 5.4, and 2.4, respectively.

it is impossible to create a SF_6 beam with a velocity ratio $S=V/\alpha$ significantly greater than unity without a buffer gas (here V is the translational velocity and α is the thermal velocity spread). The pressure must be raised to values of 10^3 Pa or more, which are common in gas-dynamic sources in which supersonic expansion of the working material is employed. However, this technique is not applicable to SF_6, because condensation appears.

The question of the equivalence of the design depicted in Fig. 1 and an axisymmetric nozzle with a continuous annular critical cross section was specially investigated within the present work. For this purpose the experimentally obtained parameters of the supersonic flow of the buffer gas were compared with the results of gas-dynamic calculations for a model nozzle of similar configuration that has a continuous annular critical cross section with an area equal to the sum of the critical cross sections of the nozzles in the multinozzle source.

Such a comparison must be made with some caution.

Time-of-flight measurements are known to provide unequivocal information regarding the parameters of beams formed by gas-dynamic sources.[9] However, the experimentally determined parameters of a beam can be related to the parameters of the supersonic flow in the region of the tip of the skimmer only if the distortions caused by the interaction of the flow with the skimmer and by scattering on the background gas and the gas reflected from the skimmer surface are eliminated (or, at least, can be taken into account).

Under conditions where the theories of gas-dynamically continuous media are applicable, the finite size of the tip edge leads to the appearance of a diverging shock wave. As it passes, the parameters of the flow, viz., its pressure, density, velocity, and temperature, undergo abrupt and unpredictable changes. The total gas flux through the skimmer, whose value is proportional (to within the constancy of the pumping speed) to the pressure in the chamber beyond the skimmer P_{sk}, remains unperturbed. Therefore, plots of the dependence of P_{sk} on R, i.e., the position of the source in the plane perpendicular to the skimmer axis, were measured to compare the calculations with experiment. Series of such plots corresponding to different formation conditions in terms of the pressure P_0 and the distance along Z between the nozzle and the skimmer were obtained. A typical measured dependence of P_{sk} on R and the corresponding calculated curve are presented in Fig. 3a.

In flow regimes corresponding to the transition to free molecular flow, even a slight change in the direction of motion of particles as a result of collisions causes them to leave the beam. This is reflected directly in the intensity of the beam and, to a lesser degree, in its TOF spectrum. In this case the Mach number extracted from TOF spectra of the buffer-gas beam (Fig. 3b) can serve as a criterion of the equivalence between experimental data and the results of gas-dynamic calculations.

The flow field of the buffer gas escaping from the model axisymmetric nozzle was calculated using the familiar large-particle method, which is described in detail in Ref. 10. In the large-particle method the state of the medium is described by a system of Euler equations in conservative form,

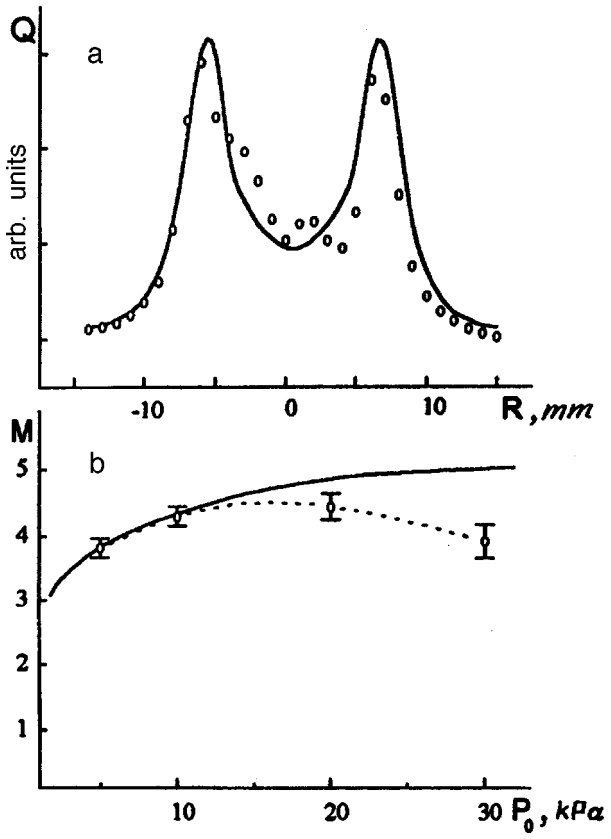

FIG. 3. Comparison of the flow fields of the N_2 buffer gas formed by the six-nozzle source and calculated for the model nozzle; a — transverse distribution of the buffer gas flow rate [$P_0(N_2)=1\times10^4$ Pa] through the skimmer; b — dependence of the limiting value of the Mach number at the source axis on $P_0(N_2)$.

which is closed by the equation of state of an ideal gas. The system of equations is approximated by a first-order difference scheme, which provides stable solutions without introducing an artificial viscosity. It should be stressed here that, although the Euler equations for a nonviscous gas are taken initially, the difference scheme used in the calculation is capable of reproducing viscosity effects. The number of operations needed to solve this time-dependent system can be reduced significantly by splitting it into physical processes and thereby constructing numerical models for the Euler, Navier–Stokes, and Boltzmann equations.[11]

The calculations were performed in a cylindrical coordinate system using a uniform grid (1000 points in R and 300 points in Z). Solid-wall conditions prescribed on the surface of the nozzle and the skimmer, i.e., the velocity component normal to the surface is set equal to zero. The initial conditions are ordinary: the velocity components are assumed to be equal to zero over the entire calculation region. The gas pressure in the subsonic part of the nozzle is equal to the prescribed back pressure P_0. In the remaining space the pressure is close to the value of the residual pressure in the source chamber: $P_1=1$ Pa. A zeroth-order extrapolation is performed on the open boundaries of the integration region, in which the values of the parameters are transferred from the calculated layer adjacent to the boundary to a fictitious layer.

As we see from Fig. 3, the calculations of the escape of the buffer gas from the model nozzle describe the results of the experiments on the six-nozzle design quite well.

Thus, the results obtained show that multinozzle designs can be employed, in principle, instead of axisymmetric nozzles with an inner body in molecular-beam sources. This relaxes the requirements placed on the accuracy needed in fabricating such sources and permits reduction of the buffer gas flow rate and, consequently, the employment of fairly simple schemes for recycling the buffer gas.

In addition, the positive answer obtained regarding the equivalence between the multinozzle design depicted in Fig. 1 and an axisymmetric nozzle with a continuous annular critical cross section permits significant simplification of the gas-dynamic calculations aimed at optimizing the geometry of the source, since it is sufficient to consider the two-dimensional problem instead of the three-dimensional one.

This work was performed as part of the preparations for an experimental search for effects of the violation of T invariance in molecules, supported by Grant No. 97-02-16908 of the Russian Fund for Fundamental Research.

[1] V. L. Varentsov and V. V. Yashchuk, Pis'ma Zh. Tekh. Fiz. **9**, 147 (1983) [Sov. Tech. Phys. Lett. **9**, 65 (1983)].
[2] V. L. Varentsov, V. F. Ezhov, V. A. Knyaz'kov *et al.*, Zh. Tekh. Fiz. **57**, 755 (1987) [Sov. Phys. Tech. Phys. **32**, 457 (1987)].
[3] U. G. Pirumov and G. S. Roslyakov, *Gas Flow in Nozzles*, Springer, New York (1986).
[4] B. N. Ashkinadzi, M. N. Groshev, V. F. Ezhov *et al.*, Preprint No. LNPI-1801, Leningrad Nuclear Physics Institute (1992).
[5] M. G. Kozlov and V. V. Yashchuk, Pis'ma Zh. Éksp. Teor. Fiz. **64**, 659 (1996) [JETP Lett. **64**, 709 (1996)].
[6] V. V. Yashchuk, Candidate's Dissertation, Leningrad (1994).
[7] B. N. Ashkinadzi, V. F. Ezhov, and M. N. Groshev *et al.*, Preprint No. PIYaF-2127, St. Petersburg Nuclear Physics Institute (1996).
[8] V. V. Yashchuk, B. N. Ashkinadzi, and V. F. Ezhov *et al.*, Prib. Tekh. Éksp. (1997) (in press).
[9] D. J. Auerbach, in *Atomic and Molecular Beam Methods*, G. Scoles (ed.), Oxford University Press, New York (1988), Vol. 1, p. 362.
[10] O. M. Belotserkovskiĭ and Yu. M. Davydov, *The Particle-in-Cell Method in Gas Dynamics* [in Russian], Nauka, Moscow (1982).
[11] O. M. Belotserkovskiĭ, *Numerical Methods in Liquid Dynamics* [in Russian], Mir, Moscow (1981), p. 348.

Translated by P. Shelnitz
Edited by David L. Book

Deep surface states on the interface between SiC and its native thermal oxide

P. A. Ivanov, K. I. Ignat'ev, V. N. Panteleev, and T. P. Samsonova

A. F. Ioffe Physicotechnical Institute, Russian Academy of Sciences, St. Petersburg, Russia
(Submitted 9 June 1997)
Pis'ma Zh. Tekh. Fiz. **23**, 55–60 (October 26, 1997)

Deep surface states are discovered on the interface between 6H-SiC and its native thermal oxide by analyzing the $C-V$ characteristics of metal-oxide-semiconductor structures measured at a high temperature (600 K). The maximum of the density of states distributed according to energy ($D_{tm}=2\times10^{12}$ cm$^{-2}\cdot$eV^{-1}) is at an energy about 1.2 eV below the bottom of the conduction band of SiC. It is postulated that the states discovered are similar in nature to the P_b centers observed in the SiO_2/Si system. © *1997 American Institute of Physics.* [S1063-7850(97)02710-9]

The surface states on the interface between silicon carbide and its native thermal oxide (SiO_2) have been investigated in several studies by analyzing the $C-V$ and $G-V$ characteristics of metal–oxide–semiconductor (MOS) structures. In the case of n-type SiC the $C-V$ characteristics measured at room temperature were found to be nearly ideal in many studies;[1–3] however, it should still not be concluded from this that the density of surface states is small. The fact is that the $C-V$ characteristic of an MOS structure based on such a wide-gap semiconductor as SiC at room temperature should be nonequilibrium with respect to the filling of the deep surface states,[1] so that it is impossible to reveal them in this case. In fact, let us estimate the relaxation time (τ) of energy-distributed surface states from the formula

$$\tau=(\sigma\nu n_s)^{-1}=\frac{\exp(\Delta E_t/kT)}{\sigma\nu N_c}, \tag{1}$$

where σ is the cross section for the trapping of majority carriers by surface states, ν is the thermal velocity of the carriers, n_s is the carrier concentration on the surface when the energy level of the surface states and the Fermi level on the surface coincide, ΔE_t is the depth of the surface states in the band gap of SiC, and N_c is the effective density of states in the allowed band of SiC. For the estimates we set $\sigma=10^{-15}$ cm^2, $\nu=10^7$ cm/s, $N_c=10^{19}$ cm^{-3}, and $T=300$ K. Then, for $\Delta E_t>0.6$ eV we obtain $\tau>10$ s. Typical gate voltage sweep times during measurements of $C-V$ characteristics usually range from a few seconds to tens of seconds, i.e., in this case the filling of surface states with energies $\Delta E_t>0.6$ eV will not follow the variation of the surface potential as the gate voltage is increased. In the present work, to reveal the deep surface states on the SiO_2/6H$-$SiC interface, the $C-V$ characteristics of the MOS structures were measured at 600 K, and they were analyzed by Terman's differential method, which is sensitive to the slow charge transfer between surface states (see, for example, Ref. 4).

The samples oxidized were n-type 6H-SiC films with a concentration of uncompensated donors ranging from 1.5×10^{15} to 2×10^{15} cm^{-3}, which were grown by chemical vapor deposition on the misoriented Si(0001) surface of Lely crystals. Before oxidation, the wafers with the epilayers were treated in trichlorethylene and a peroxide-ammonia solution and then washed in deionized water. The oxidation was carried out by the ''moist'' method at 1100°C for 5 h. The field-effect electrode was made from molybdenum, and the ohmic contact on the n-type substrate was composed of nickel. The $C-V$ characteristics were measured by an automated method at a frequency of 1 MHz.

Typical $C-V$ and $G-V$ characteristics measured at $T=600$ K are shown in Fig. 1 (the figure also presents the theoretical $C-V$ curve corresponding to an ideal MOS structure, which is needed for the Terman analysis). As we see, the experimental $C-V$ characteristic has a shoulder in the depletion region, which attests to the presence of surface states with a fairly high density and the occurrence of charge transfer between them. For the Terman analysis to be correct, two conditions must be satisfied in the range of variation of the gate voltage considered. First, the criterion for a high-frequency $C-V$ characteristic, $\omega\tau\gg1$ (ω is the circular frequency of the measuring signal), must be satisfied. As we see from Fig. 1, the MOS conductivity peak (which corresponds to the condition $\omega\tau=1$) is observed at gate voltages of small absolute value (it is associated with charge transfer between shallower surface states at the frequency of the test signal), so that the criterion for high-frequency behavior is clearly satisfied in the region of the shoulder. Second, the condition of quasiequilibrium filling of the surface states in response to changes in the controlling gate voltage must be fulfilled. Fulfillment of this criterion is indirectly evidenced by the fact that an inversion layer due to the thermal generation of pairs at $T=600$ K formed within a few seconds.

At an assigned surface potential the experimental high-frequency MOS capacitance coincides with the theoretical value, so that the dependence of the density of surface states (D_t^*) on the surface potential (ψ_s) can be determined from the expression

$$qD_t^*(\psi_s)=C_{\rm ox}\left(\frac{dV_{\rm exp}}{d\psi_s}-1\right)-C_s(\psi_s), \tag{2}$$

where q is the electron charge, $V_{\rm exp}$ is the experimental value of the gate voltage corresponding to the surface potential ψ_s, $C_{\rm ox}$ is the specific capacitance of the oxide, and C_s is the specific capacitance of the space-charge region of the semiconductor. We utilize the obvious relations for an ideal MOS structure: $V_{\rm theor}=V_{\rm ox}+\psi_s$ and $1/C=1/C_{\rm ox}+1/C_s$, where $V_{\rm theor}$ and $V_{\rm ox}$ are the calculated values of the gate voltage

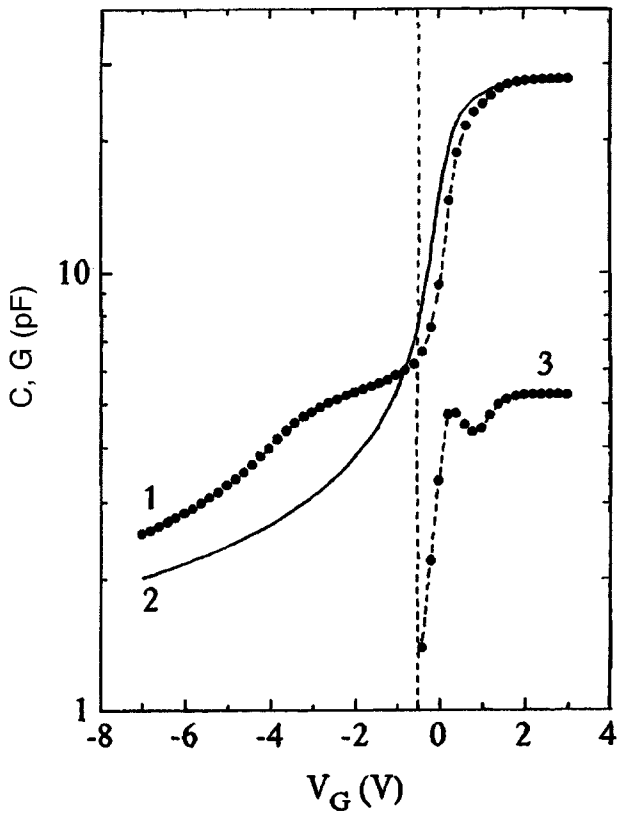

FIG. 1. *1* — Experimental $C-V$ characteristic of an MOS structure based on 6H–SiC ($T=600$ K, $f=1$ MHz), *2* — corresponding theoretical $C-V$ characteristic (in the absence of surface states), *3* — experimental dependence of the MOS conductivity on the gate voltage normalized to the frequency of the measuring signal.

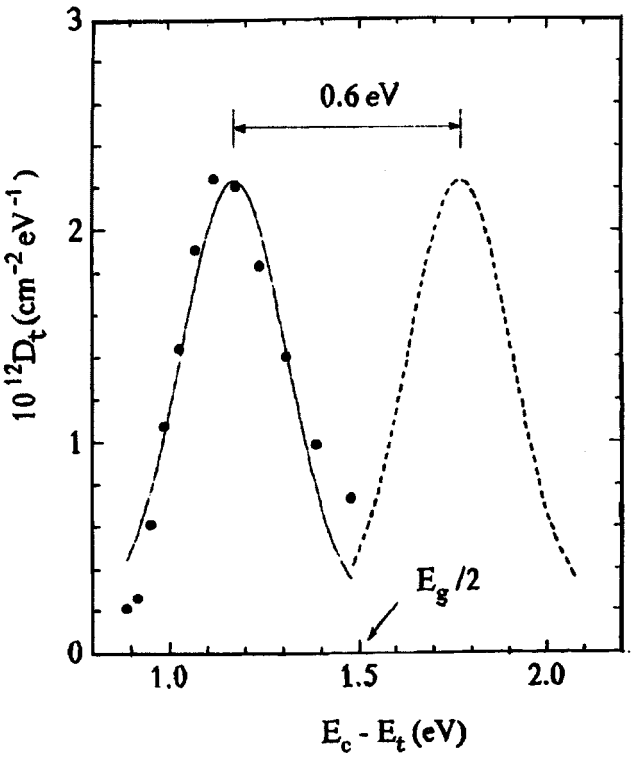

FIG. 2. Distribution of the density of surface states according to their energy in the 6H–SiC band gap. Points — Terman analysis of $C-V$ characteristics, solid line — approximation of the experimental data by a Gaussian distribution, dotted line — hypothetical peak of the density of donor states in the lower half of the 6H–SiC band gap.

and the voltage drop in the oxide (which also correspond to ψ_s). In addition, let us assign an energy $\Delta E_t = q\psi_s + \Delta E_{F_0}$ to each value of ψ_s, where ΔE_{F_0} is the position of the Fermi level in the neutral region relative to the conduction band. Then Eq. (2) can be brought into a form that is more graphic and more convenient for the analysis, i.e., into the form of a distribution of the density of surface states according to their energy in the band gap of the semiconductor:

$$qD_t(\Delta E_t) = C_{\text{ox}} \frac{d(V_{\text{exp}} - V_{\text{theor}})}{d(q\psi_s + E_{F_0})}. \tag{3}$$

The distribution of the density of states on the $SiO_2/H-SiC$ interface calculated using Eq. (3) is shown in Fig. 2. We note that it is approximated well by a Gaussian distribution with a maximum $D_{tm} = 2\times 10^{12}$ cm$^{-2}\cdot$eV^{-1} at $E_c - E_t \approx 1.2$ eV. The estimates based on Eq. (1) give low values for the electron trapping cross section, indicating the acceptor nature of the states discovered. The data obtained do not contradict the results of other studies, which were performed at lower temperatures than in the present work. For example, in our previous work[5] we detected an increase in the density of acceptor states in the energy range 0.4–0.7 eV below the bottom of the conduction band. An increase in the density of surface states was also subsequently discovered in Ref. 3, but it was observed down to 1 eV from the conduction band.

This raises the question of the nature of the surface states discovered. As many researchers have noted, the charge properties of the SiO_2/SiC system are similar in many respects to the properties of the SiO_2/Si system. As for the latter, it was reliably established by recent investigations that the main contribution to the density of surface states on the SiO_2/Si interface is made by paramagnetic P_b centers in the form of ''oxidation defects,'' i.e., centers of the $\bullet Si\equiv Si_3$ type with dangling bonds.[6] These centers have an amphoteric character, and the density of states associated with them has two peaks in the silicon band gap that are positioned nearly symmetrically relative to the middle of the gap: acceptor states (which correspond to minus$\rightarrow$0 electron transitions) in the upper half of the band (with a maximum at $E_v + 0.85$ eV) and donor states (which correspond to 0$\rightarrow$plus electron transitions) in the lower half of the band (with a maximum at $E_v + 0.25$ eV). The difference between the detachment energies of the first and second electrons (the so-called correlation energy) amounts to about 0.6 eV. If we presume the existence of a symmetric peak of surface states in the lower half of the band gap in the case of SiO_2/SiC [which is indicated indirectly by data from investigations of MOS structures based on p-type SiC (Ref. 2)], the correlation energy also amounts to about 0.6 eV. This suggests that the surface states on the SiO_2/SiC interface are similar in nature to the P_b centers in the SiO_2/Si system.

We thank A. Yu. Maksimov, A. A. Mal'tsev, and N. K. Yushin for the SiC crystals with epitaxial films provided for this research.

[1] P. A. Ivanov, A. O Konstantinov, V. N. Panteleev, T. P. Samsonova, and V. E. Chelnokov, Semiconductors **28**, 668 (1994).
[2] D. M. Brown, M. Ghezzo, J. Kretchmer, E. Downey, E. Pimbley, and J. Palmour, IEEE Trans. Electron Devices **ED-41**, 618 (1994).
[3] S. Sridevan, V. Mistra, P. K. McLarty, B. J. Baliga, and J. J. Wortmann, in *Silicon Carbide and Related Materials 1995 (Institute of Physics Conference Series No. 142)*, S. Nakashima, H. Matsunami, S. Yishida, and H. Harima (eds.), Institute of Physics, Bristol–Philadelphia (1996), pp. 645–648.
[4] S. M. Sze, *Physics of Semiconductor Devices*, 2nd ed., Wiley-Interscience, New York (1969); Mir, Moscow (1984), Vol. 1.
[5] P. A. Ivanov, V. N. Panteleev, T. P. Samsonova, and V. E. Chelnokov, Semiconductors **29**, 135 (1995).
[6] G. J. Geardi, E. H. Poindexter, and P. J. Caplan, Appl Phys. Lett. **49**, 348 (1986).

Translated by P. Shelnitz
Edited by David L. Books

Influence of the spectral characteristics of gas lasers on the signals of fiber-optic interferometers

O. I. Kotov, L. B. Liokumovich, V. M. Nikolaev, V. Yu. Petrun'kin, and B. Zekhraui

St. Petersburg State Technical University, St. Petersburg, Russia
(Submitted 18 April 1997)
Pis'ma Zh. Tekh. Fiz. **23**, 61–69 (October 1997)

The fading of the signal amplitude of an unbalanced interference system in response to changes in the emission spectrum of the optical source is investigated. The condition for stability of the signal amplitude of fiber-optic interferometers in systems with gas lasers that are not frequency-stabilized is found. © *1997 American Institute of Physics.* [S1063-7850(97)02810-3]

Both balanced and unbalanced interferometer systems are employed in fiber-optic phase sensors.[1,2] As a rule, an effort is made to use balanced systems (Sagnac interferometers and equal-arm Mach–Zehnder and Michelson interferometers) in which the output signal of the interferometer is practically insensitive to changes in the emission spectrum of the optical source. However, in some cases (in single-fiber systems and remote sensors with a passive interferometer[3,4]) it is convenient or necessary to use unbalanced interference systems (unequal-arm Mach–Zehnder and Michelson interferometers, single-fiber Fabry–Pérot and ring interferometers). In such cases the behavior of the output signal depends significantly on the spectral characteristics of the light source and their stability. In this case changes in the emission spectrum of the laser lead to the following phenomena.

1. A shift in the laser frequency causes a change in the optical length of the interferometer and corresponding shifts in the output interference signal. This factor is a direct nuisance in interferometric measurements, but it can be eliminated in most cases, because the drift of the laser spectrum is much slower than the effects being measured.[1,2]

2. Signals from different components of the source spectrum can cancel one another with resultant fading of the interference contrast (fading of the interferometer signal amplitude), which is an irremovable nuisance in measurements.

In the present work we studied the latter phenomenon, viz., the fading of the signal amplitude (contrast) of an unbalanced interference system in response to changes in the emission spectrum of the optical source. The purpose of the investigation was to find the conditions for stability of the signal amplitude of fiber-optic interferometers in systems with gas lasers that are not frequency-stabilized. The known publications addressing these issues[5–7] do not provide a complete explanation for all the phenomena in laser-interferometer systems when fiber-optic light guides of different types, viz., single-mode light guides and multimode light guides of different shapes, are used.

A standard miniature LG-207 helium–neon laser ($\lambda = 0.63$ μm) with a cavity length of the order of $l = 20$ cm and a low-Q traveling-wave ring interferometer were used in the experiments (Fig. 1).

The emission spectrum of the gas laser was thoroughly studied using a scanning Fabry–Pérot interferometer (not shown in Fig. 1). The dependence of the amplitudes of the modes generated on the relative detuning of the laser cavity has the form of a fairly complicated curve (Fig. 2a), which reflects the mode competition processes ($\Gamma = c/2l$ is the intermode spacing of the cavity). In the narrow central tuning region the laser generated one mode (position *1* in Fig. 2a). The retuning of its frequency to position *2* (solid line) resulted in the appearance of a second mode (*2′*, dashed line). Further retuning of the modes to positions *3–4–5–6* and *3′–4′–5′–6′* caused significant variation of their amplitudes with small changes in the total radiated intensity of the laser (the latter were less than 3%). The following important features of the behavior of the emission spectrum of the laser can be noted as a result.

1. The laser emits both in a single-mode or nearly single-mode regime (the second mode is small compared with the fundamental mode) and in a two-mode regime with nearly equal mode amplitudes (position *4–4′*). When the frequency is retuned in the two-mode regime, the intermode spacing $\Gamma = \pi c/l$ remains unchanged.

2. An increase in the amplitude of one mode is accompanied by a decrease in the amplitude of the other mode. This leads to the high stability of the total output power of the laser.

3. The asymmetry of the curve in Fig. 2a is attributable, in our opinion, to operation of the laser in the natural mixture of neon isotopes, which is characterized by asymmetry of the gain line.

In the experimental setup (Fig. 1) for investigating the interferometer signal amplitude upon retuning of the spectrum of laser *1*, the light-dividing plate *3* had a reflection coefficient of ~10%. For work with a variable signal (which is convenient for measuring and monitoring the signals) the setup included the generator *7* and modulator *6*, which provided for phase modulation of the light in fiber *5* with an index greater than 2π (for observing several interference maxima). The signal from photodetector *2* was observed on oscillograph *11* and fed into spectrum analyzer *8*. A signal proportional to the amplitude of the first harmonic of the photodetector signal was transmitted from the output of the spectrum analyzer detector to the Y input of recorder *9*. A low-frequency sawtooth voltage from generator *10* was supplied to the X input of the recorder (the timed sweep was of the order of 1000 s). The gas laser was retuned using Peltier elements *12*, which alter the temperature of the protective housing of the laser. The interferometer length L was varied by cutting the fiber. The layout of the traveling-wave ring

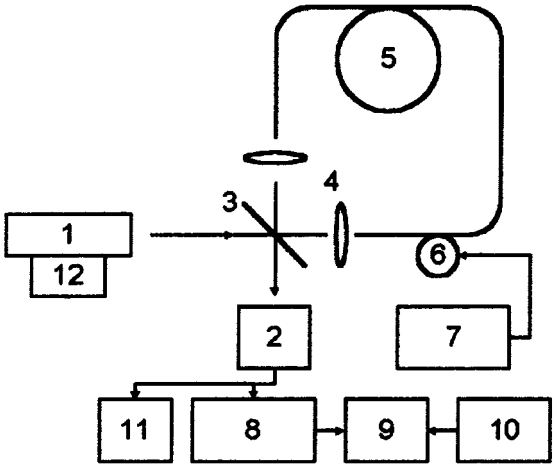

FIG. 1. Schematic representation of the experimental setup for measuring the signal amplitude of a ring interferometer in response to frequency retuning of a gas laser.

interferometer was chosen so as to weaken the influence of feedback light and the quality of the cut ends on the measurement results.

The interferometer signal in the single-mode fiber depends on the retuning of the spectrum and the length of the ring cavity (Figs. 2b and 2c). The fast signal fluctuations are ordinary interference oscillations with a period c/Ln due to variation of the optical length of the fiber (variation of the phase difference between the interfering beams). The fluctuations of the envelope (amplitude) reflect the fading of the interference contrast.

When the optical length of the fiber was an odd multiple of the laser cavity length, there were contrast minima of the signal amplitude (Fig. 2b), which correspond to two-frequency lasing with symmetric tuning relative to the center of the line (Fig. 2a, position *4–4′*). When the optical length of the ring interferometer was an even multiple of the laser cavity length, these minima were absent (Fig. 2c), and the signal amplitude scarcely depended on the retuning of the laser spectrum.

The relative height of the signal minimum ($U_{\min}/U_{\max}$) depends on the interferometer length according to a periodic law close to $|\cos(nL/2l)|$ (Fig. 3a), where n is the refractive index of the fiber core). These dependences were observed for short ($L\sim 1$ m) and long ($L\sim 500$ m) bases of the fiber-optic interferometer.

An interferometer with a multimode graded-index fiber-optic light guide was also investigated (the diameter of the core was 50 μm, and the numerical aperture was 0.17). Dependences completely analogous to those for the single-mode interferometer were observed at short light guide lengths (Figs. 2b, 2c, and 3a). At large light guide lengths ($L\sim 700$ m) variation of the interferometer length caused random variation relative to the interference contrast minimum (Fig. 3b). As before, when the emission spectrum of the laser was retuned, minima of the signal amplitude were observed in the two-frequency lasing regime (Fig. 2d). The value of $U_{\min}/U_{\max}$ also depended on the mode excitation conditions in the fiber.

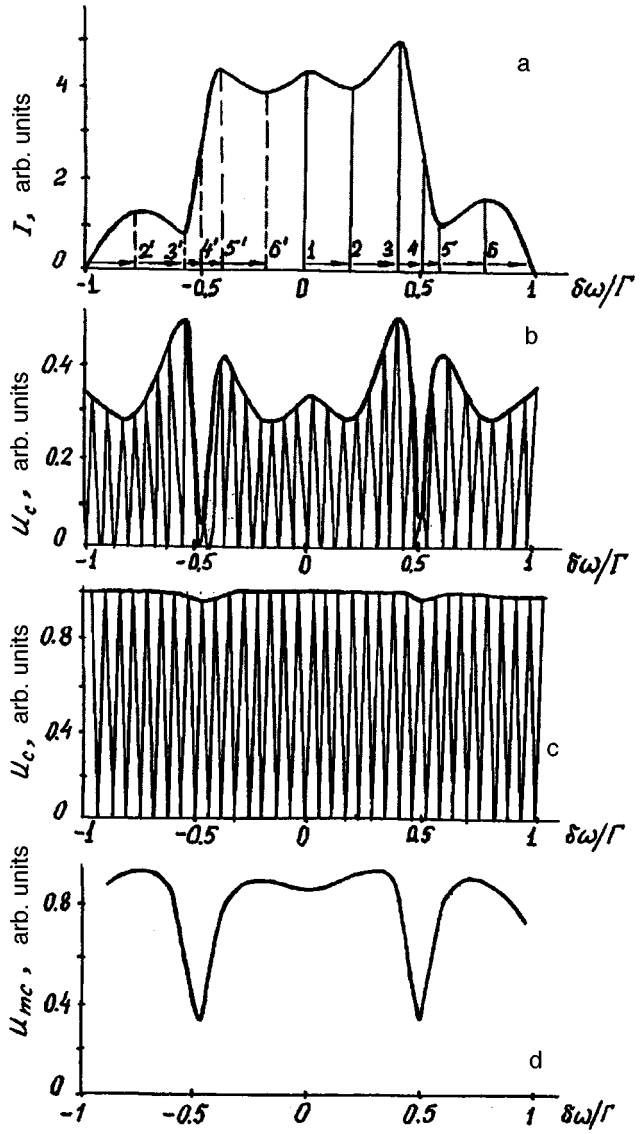

FIG. 2. Observed dependences of the amplitudes of the modes of the gas laser (a) and the interferometer signal (b, c, d) when the laser cavity is retuned.

The results of the experiments for the single-mode fiber-optic interferometer are easily explained using coherence functions. The interference term in the optical intensity at the exit from a ring fiber-optic interferometer is proportional to the coherence function $\gamma(\tau)$:[8,9]

$$I_{\sim}=A\cdot|\gamma(\tau)|\cos(\beta L), \tag{1}$$

where A is a constant, which is determined by the mirror and the input optical intensity, β is the light propagation constant in the fiber at the central frequency of the laser emission line, and τ is the time delay between the interfering waves.

The variation of $\gamma(\tau)$ upon retuning of the laser emission spectrum causes variation of the interference contrast (the interference signal amplitude). Central tuning (position *1* in Fig. 2a) corresponds to a single-frequency lasing regime and $\gamma(\tau)=1$. Here and below we shall assume that the width of the emission line of an individual mode in the laser spectrum (of the order of 10 kHz) is negligibly small and the

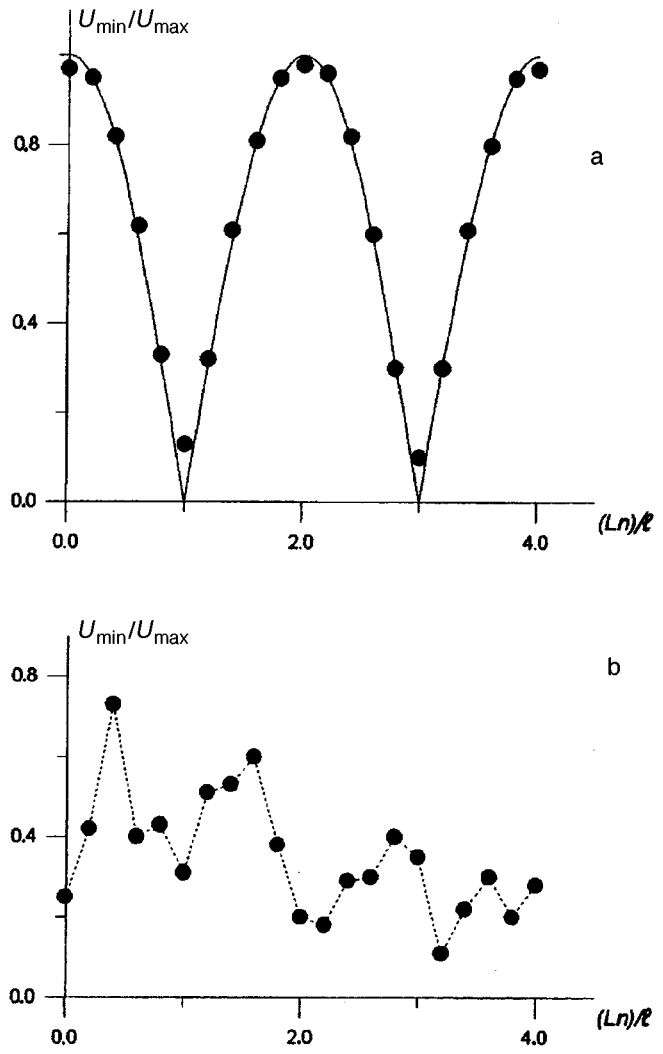

FIG. 3. Dependence of the relative height of the minima of the signal of a ring interferometer on the length of the fiber-optic light guide: a — single-mode light guide, b — multimode light guide, $L \sim 300$ m.

emission can be considered monochromatic. Transition to a two-frequency lasing regime can reduce $\gamma(\tau)$. The point of symmetric tuning (position *4–4′* in Fig. 2a) with equal mode amplitudes corresponds to the coherence function:[8,10]

$$|\gamma(\tau)| = |\cos(\Gamma\tau/2)|. \tag{2}$$

Hence it follows that the relative height of the minima of the interferometer signal amplitude depends on the interferometer length according to a cosinusoidal law: $(U_{min}/U_{max}) \sim |\cos(\Gamma\tau/2)| = |\cos(nL/2l)|$ (Fig. 3a).

The decrease in the interference contrast can be explained in another way: the interference patterns of the individual laser modes under the condition $nL = (2k+1)l$, where k is an integer, are shifted by π, i.e., the minimum of one is at the maximum of the other. The total (summed) interference signal can cancel out (Fig. 2b). When $nL = 2kl$, the interference signals of the laser modes are in phase, and the interferometer signal amplitude does not depend on their retuning (Fig. 2c).

The signal of a multimode interferometer can be represented in the form

$$I_{\sim} = A \cdot \sum_{m=1}^{M} C_m^2 \cdot \cos(\beta_m \cdot L + \varphi_m) \cdot |\gamma(\tau_m)|, \tag{3}$$

where C_m and β_m are the amplitude coefficient and the propagation constant of the mth mode of the fiber-optic light guide, and M is the number of modes propagating.

It was taken into account in Eq. (3) that the photodetector picks up all the output radiation of the interferometer and that the interference terms of the fiber modes with the same mode number make contributions to the signal because of the orthogonality of the modes.

At small values of the light guide length L the differences between the relative group delays of the individual modes are small:

$$\frac{|\tau_m - \tau_n|}{T} \ll 1, \quad \text{where } T = \frac{2\pi}{\Gamma}. \tag{4}$$

Under this condition we have $\gamma(\tau_m) \approx \gamma(\tau_n) = \gamma(\tau)$, and the coherence function does not depend on the mode number and can be taken out of the summation sign in Eq. (3):

$$I_{\sim} = A|\gamma(\tau_m)| \sum_{m-1}^{N} C_m^2 \cos(\beta_m L + \varphi_m). \tag{5}$$

Expression (5) shows that the behavior of the signal amplitude of short multimode interferometers in response to retuning of the laser spectrum is similar to the behavior of the amplitude of single-mode systems [Eq. (1)], since here, too, the multiplier in front of the interference signal is $\gamma(\tau)$. This was also observed in the experiments (Fig. 3a).

In long multimode interferometers, where the difference between the relative delays of the modes becomes large, i.e., $|\tau_m - \tau_n|/T \sim 1$, the quantity $|\gamma(\tau_m)|$ can take any value in the interval [0, 1] in the general case and varies as a function of the mode number m. Now $|\gamma(\tau_m)|$ can no longer be taken out of the summation sign in (3), and this results in the disappearance of the regular cosinusoidal dependence of U_{min}/U_{max} on the fiber length. In this case the dependence of the interference signal amplitude on the fiber length is specified by the sum of the terms in (3), whose cofactors are the cosinusoidal functions $\gamma(\tau_m) = \cos(\Gamma\tau_m/2)$ with significantly different arguments. This results in irregular variation of the signal contrast as a function of the interferometer length (Fig. 3b).

However, the chaotic character of this dependence does not rule out several laws in the behavior of the interferometer signal amplitude in response to retuning of the laser spectrum (Fig. 2d). Significant decreases in the signal amplitude (interference contrast) were observed for symmetric tuning of the laser modes (position *4–4′*, Fig. 2a). This is attributed to a decrease in the value of $\gamma(\tau)$ for such tuning of the laser cavity in comparison to region *1–2–3, 5′–6′*, in which $\gamma(\tau)$ is close to unity (as in the monochromatic regime).

The foregoing discussion referred mainly to systems with miniature gas lasers having a cavity length of the order of 20 cm (such as the LGN-207, LGN-105, LG-78, LG-52-3, and other such lasers) that operate in a regime with the fundamental transverse mode and one or two longitudinal

modes. However, the approaches described can be generalized to the case of lasers with a large number of modes.

The results of this investigation allow us to draw a conclusion regarding the optimum operating conditions of unbalanced interferometer systems. To eliminate amplitude fading in single-mode interferometers, a path difference between the interfering waves that is a multiple of the doubled length of the optical cavity of the laser must be provided. The same condition is optimal for short multimode interferometers. In the case of long multimode interferometers there are no optimum values for the light guide length, and stabilization of the emission frequency of the laser is necessary.

[1] M. M. Butusov, S. L. Galkin, S. P. Orobinskiĭ, and B.P. Pal, *Fiber Optics and Instrument Making* [in Russian], Mashinostroenie, Leningrad (1987).

[2] B. A. Krasyuk, O. G. Semenov, A. G. Sheremet'ev, and V. A. Shesterikov, *Light-Guide Sensors* [in Russian], Mashinostroenie, Moscow (1990).

[3] A. Dandrige, A. B. Tventen, and T. G. Giallorenzi, J. Quantum Electron. **QE-18**, 1647 (1982).

[4] G. Zhend, M. Campbell, P. A. Wallace, A. C. Holmes–Smith, and A. Sheila, in *Fiber Optic and Laser Sensors XIV (Proceedings of SPIE, Vol. 2839)*, The International Society for Optical Engineering (1996), pp. 272–276.

[5] Yu. A. Bykovskiĭ, Yu. N. Kul'tin, and O. B. Vitrik, Izv. Vyssh. Uchebn. Zaved., Radiofiz. **33**, 1301 (1990).

[6] I. S. Volkov, A. V. Voler, L. M. Kuchekyan, M. E. Kondakov, and V. N. Savchenko, Zh. Prikl. Spektrosk. **47**, 393 (1987).

[7] V. I. Borisov and V. I. Lebedev, Zh. Prikl. Spektrosk. **50**, 90 (1989).

[8] J. W. Goodman, *Statistical Optics*, Wiley, New York (1985); Mir, Moscow (1983).

[9] P. Hlubina, J. Mod. Opt. **41**, 2209 (1994).

[10] P. Hlubina, in *Interferometry '94: Interferometric Fiber Sensing (Proceedings of SPIE, Vol. 2341)*, The International Society for Optical Engineering (1994), pp. 182–191.

[11] O. I. Kotov, S. A. Kuzubov, A. V. Medvedev, V. M. Nikolaev, and V. N. Filippov, Opt. Spektrosk. **73**, 1021 (1992) [Opt. Spectrosc. (USSR) **73**, 612 (1992)].

Translated by P. Shelnitz
Edited by David L. Book

Investigation of the properties of CdO films

A. M. Baranov, Yu. A. Malov, S. A. Teryoshin, and V. O. Val'dner

S. A. Vekshinskiĭ State Scientific-Research Institute of Vacuum Technology
(Submitted 14 April 1997)
Pis'ma Zh. Tekh. Fiz. **23**, 70–74 (October 26, 1997)

Cadmium oxide films obtained by magnetron sputtering of a cadmium target in a nitrogen-oxygen mixture are investigated. It is established that these films have a lower resistivity than do films obtained by other methods. It is concluded that the practical utilization of CdO films as transparent electrodes would be worthwhile. © *1997 American Institute of Physics.* [S1063-7850(97)02910-8]

The interest in transparent, electrically conductive oxides rose in the mid-sixties and has not waned up until the present time. Transparent, electrically conductive oxides are employed as electrodes in liquid-crystal displays, photodiodes, solar batteries, and other devices.

The number of known current-conducting broad-band oxides is small.[1] The most widely known materials are indium oxide (In_2O_3) and stannic oxide (SnO_2). Both materials have *n*-type conduction and an optical gap width $E_g > 3$ eV. To obtain a low resistivity, In_2O_3 films must be grown at a temperature near 400°C, or subsequent annealing must be performed.[2] This is not always possible. Stannic oxide films have been obtained with the lowest resistivity at room temperature. However, the resistivity of SnO_2 films ($\approx 10^{-3}$ $\Omega \cdot$cm) is an order of magnitude higher than that of indium oxide films.[3] Therefore, the study of the properties of new transparent conductive coatings is of current interest. One such material is CdO.

Cadmium oxide (CdO) is a material that has scarcely been studied.[4,5] It is a broad-gap semiconductor of the A_2B_6 class, and its properties differ from the properties of the widely employed oxides In_2O_3 and SnO_2. It follows from Refs. 4 and 5 that this material can have *n*-type conduction, a low resistivity ($\approx 10^{-3}$ $\Omega \cdot$cm), and a fairly high transmission coefficient in the visible part of the spectrum. The optical gap width (E_g) of CdO varies from 2.3 to 2.7 eV.

The purpose of the present work was to create and investigate CdO thin films.

The CdO films were obtained by the magnetron sputtering of a cadmium target in a mixture of nitrogen (N_2) with oxygen (O_2). The pressure in the vacuum chamber was constant and amounted to 2.5×10^{-3} torr. The partial pressure of oxygen was varied from 3×10^{-4} to 12×10^{-4} torr. The films were deposited on quartz and silicon substrates at room temperature.

The optical and electrical properties of the films obtained were measured.

The transmission and reflection spectra of the CdO films obtained were measured on a Specord M40 double-beam spectrophotometer. These spectra are shown in Fig. 1a. In the range 500–900 nm the optical transmission coefficient (T) is greater than 60% and varies weakly as the wavelength of the incident light λ increases. For $\lambda < 500$ nm there is a sharp decrease in T, which is associated with the fundamental absorption of CdO. However, in the wavelength range from 200 to 400 nm the decrease in T slows as λ decreases. The figure also presents the dependence of the reflection coefficient on the wavelength. The values of the reflection coefficient R at different λ are not identical because of the interference of light in CdO films. The position of the maximum and the absolute value of the reflection coefficient at the maximum were used to determine the film thickness d and the refractive index n (at that wavelength).[6] The film thickness and n were equal to 600 A and 2.25, respectively. Then knowing d, we calculated the dependence of the refractive index on the wavelength $n = f(\lambda)$ from the transmission and reflection spectra (see Fig. 1b).[6] According to the absolute values of n, CdO films are fairly well suited for creating antireflection coatings on silicon in the wavelength range 500–900 nm.

Using the energy conservation condition, we found the optical absorption coefficient (A) of the film $A = 1-(R+T)$. It is seen that the dependence of $A = f(\lambda)$ for CdO can be separated into three regions. In the range 600–900 nm (region I) the absorption coefficient increases weakly, but does not exceed 10%. As the wavelength decreases from 600 to 400 nm (region II), the absorption coefficient increases sharply to 60%. Then, a smooth increase in absorption begins at $\lambda < 400$ nm (region III). Extrapolation of segments I and II of the plot of $A = f(\lambda)$ until they intersect gives the optical gap width $E_g = 2.5$ eV.

The resistivity (ρ) of the CdO films was measured by the four-point probe technique. The results obtained are presented in Table I.

It follows from Table I that the resistivity depends strongly on the partial pressure of oxygen in the chamber. The smallest resistivity value $\rho = 7\times10^{-4}$ $\Omega \cdot$cm corresponds to a value of the partial pressure of oxygen in the chamber $P = 5.2\times10^{-4}$ torr. Lowering the oxygen pressure

TABLE I.

Partial pressure of oxygen, torr	Resistivity, $\Omega \cdot$cm
3×10^{-4}	2.4×10^{-3}
4.5×10^{-4}	8.4×10^{-4}
5.2×10^{-4}	7×10^{-4}
7.6×10^{-4}	1×10^{-3}
1.2×10^{-3}	1.2

 1063-7850/97/100805-02$10.00 © 1997 American Institute of Physics

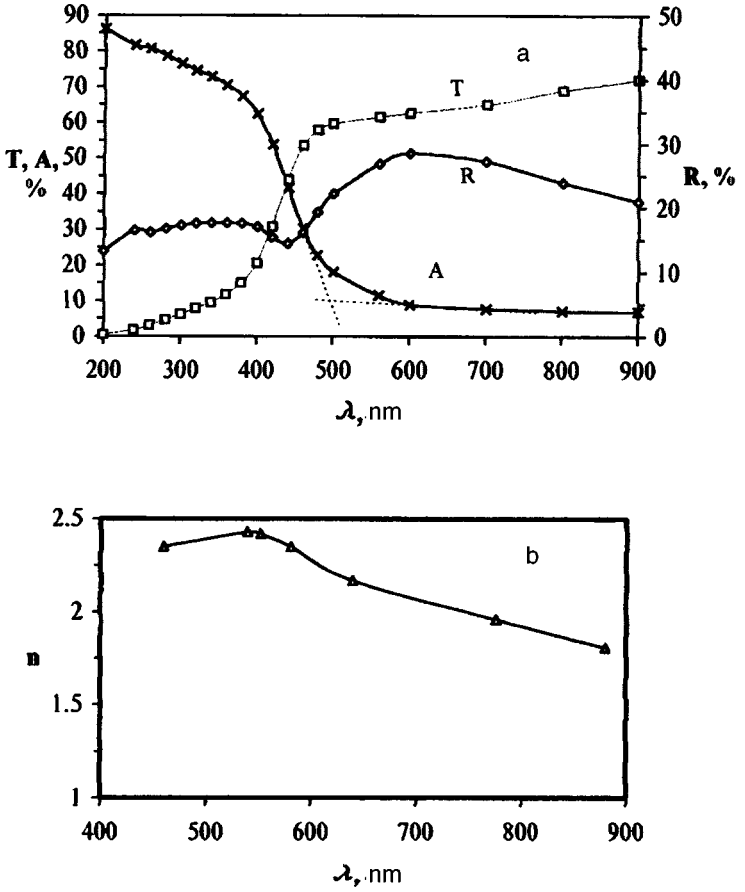

FIG. 1. Dependence of the transmission (T), reflection (R), and absorption (A) coefficients on the wavelength of the incident light λ (a) and dependence of $n=f(\lambda)$ (b).

to less than 4×10^{-5} torr leads to a sharp decrease in the transmission coefficient and an increase in the resistivity as a consequence of the presence of cadmium suboxide in the film. These films had a metallic color. The transmission coefficient and the values of E_g for the CdO films obtained at oxygen pressures greater than 4×10^{-5} torr do not depend on the values of the partial pressure. At the same time, ρ does not remain constant. An increase in the partial pressure of oxygen leads to a sharp increase in ρ.

Such behavior of ρ can be attributed to the fact that the conduction of electricity in CdO films is mediated by oxygen vacancies, which exist because of the oxygen deficiency in the films.[7] If there are not enough oxygen atoms to bond all the Cd atoms, a Cd atom that is not bonded can donate one or two of its electrons to the conduction band. If all the cadmium atoms are bonded to oxygen, the film will not be conductive.

Thus, the CdO films obtained in the present work have a lower resistivity not only in comparison with the previously obtained CdO films, but also in comparison with the widely employed SnO_2 films. As a whole, the results of this work allow us to conclude that the use of CdO films as transparent electrodes in various devices would be expedient, especially in solar cells based on Si, for which it is a very good antireflection coating.

[1] H. Hartnagel, A. L. Dawar, A. K. Jain *et al.*, *Semiconducting Transparent Thin Films*, Institute of Physics, Bristol–Philadelphia (1995), p. 358.
[2] S. P. Singh and A. K. Sharma, Thin Solid Films **105**, 131(1982).
[3] G. B. Webb and D. F. Williams, Appl. Phys. Lett. **39**, 640 (1981).
[4] T. L. Chu and S. S. Chu, J. Electron. Mater. **19** (9), (1990).
[5] C. Scavani and K. T. R. Reddy, J. Alloys Compd. **215**, 239 (1994).
[6] V. E. Kondrashov, *The Optics of Photocathodes* [in Russian], Nauka, Moscow (1976).
[7] F. A. Kröger, *The Chemistry of Imperfect Crystals*, North Holland, Amsterdam; Wiley, New York (1964); Mir, Moscow (1969).

Translated by P. Shelnitz
Edited by David L. Book

CdS–GaN heterostructure photodetector with switching and memory

A. G. Drizhuk, V. G. Sidorov, D. V. Sidorov, and M. D. Shagalov

Vologda Polytechnical Institute, Vologda, Russia
(Submitted 27 June 1997)
Pis'ma Zh. Tekh. Fiz. **23**, 75–78 (October 26, 1997)

A photodetector having two stable states is fabricated. Switching is effected by a light pulse from an external source. The states are stored until a voltage is supplied to the photodetector. The design and properties of the photodetector are presented. The basic device is an M$-i-n$-GaN light-emitting diode structure. © *1997 American Institute of Physics.*
[S1063-7850(97)03010-3]

Photosensitive semiconductor devices have found various applications in automation and optical communications systems, as well as in other areas of technology. Multifunctionality expands the possibilities for the utilization of such devices. The purpose of this paper is to present the structure and operating principle of a multifunctional photodetector based on a CdS–GaN heterostructure on sapphire.

The structure of the photodetector is shown in Fig. 1. A gallium nitride structure consisting of three layers was grown by vapor-phase epitaxy in a chloride–hydride system on a sapphire substrate oriented in the (1012) plane. A buffer layer of undoped, highly conductive n-GaN with a perfect crystal structure and a thickness of 10–20 μm provides for isolation from the substrate and crystal perfection of the higher-lying layers and simultaneously serves as an electrical contact with the high-resistivity i^+-GaN(Zn, O) layer following it. The second layer of gallium nitride is doped with zinc and oxygen. It has a resistivity of $10^3-10^5\ \Omega\cdot$cm and a thickness of 0.3–3 μm and produces effective luminescence in the blue region of the visible spectrum. The third, higher-resistivity layer has a resistivity of $10^5-10^7\ \Omega\cdot$cm and a thickness of 0.05–0.5 μm and is doped only with zinc. The ratio between the total resistances of the second and third layers is $\sim$1/10. This three-layer GaN structure is the blue light-emitting diode (LED) described in Ref. 1. Because of the asymmetric structure of the LED, blue electroluminescence is observed only when the potential in the i-GaN(Zn) layer is negative. Only in this case can the ''hot'' electrons accelerated by the electric field in the i-GaN(Zn) layer enter the next i^+-GaN(Zn, O) layer and excite the Zn-O emitting centers in it.

A photosensitive cadmium sulfide layer was deposited on the surface of the LED structure. The layer was formed by pulverizing an aqueous suspension of powdered CdS and then thermally sintering it at $\sim$580°C.[2] The CdS layer has good adhesion to GaN, and the properties of GaN remain unchanged at the annealing temperature. The emission spectrum of the M$-i-n$-GaN light-emitting diode has a maximum at an energy of 2.55 eV, which coincides almost ideally with the photosensitivity spectrum of CdS obtained by such a method. The gap width of CdS at 300 K equals 2.53 eV. The dark resistance of the CdS layer is at least an order of magnitude greater than the total resistance of the $i-n$-GaN structure. Then a transparent tin dioxide layer or a vacuum-sputtered aluminum thin film was deposited on the structure obtained. This electrode can also be continuous and opaque. Then radiation from an external source is directed through the substrate, since the GaN light-emitting diode structure is transparent up to photon energies $\sim$3.2 eV. An indium contact was formed on the n-GaN layer.

The operating principle of the photodetector is as follows. A negative potential from an external voltage source is supplied to the contact on the CdS layer, and a positive potential is supplied to the contact on the n-GaN layer. All of

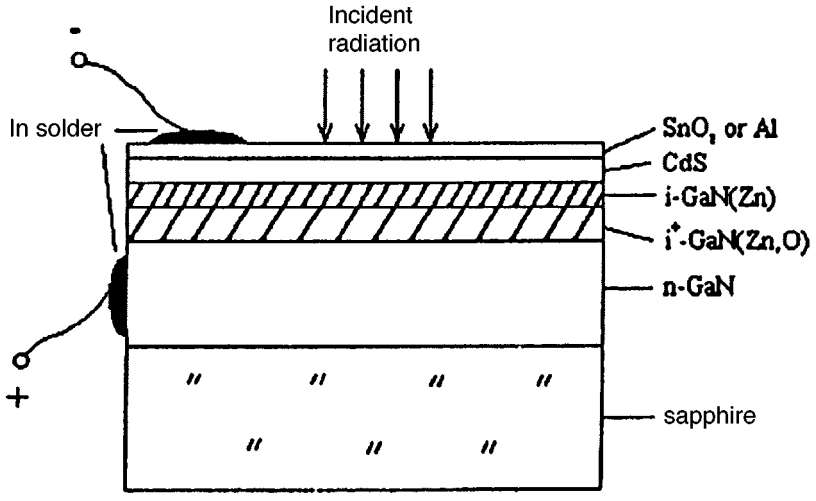

FIG. 1. Structure of the CdS–GaN photodetector.

 1063-7850/97/100807-02$10.00 © 1997 American Institute of Physics

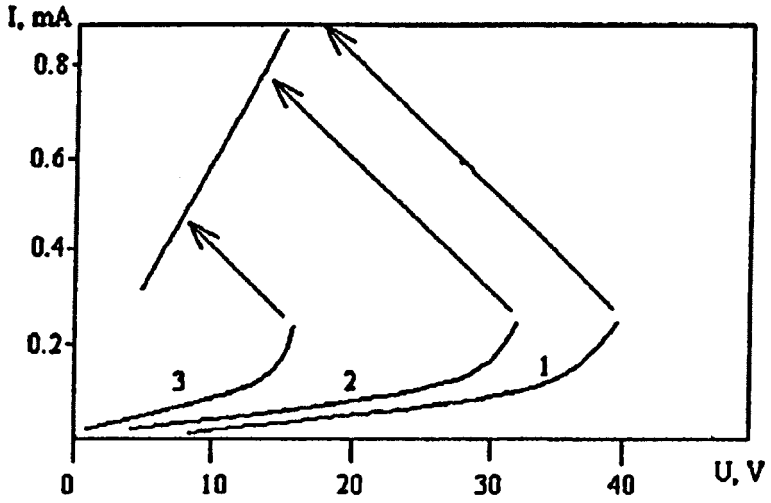

FIG. 2. Current-voltage characteristics of the photodetector for various intensities of the external illumination: $\Phi_1<\Phi_2<\Phi_3$.

the voltage applied to the photodetector falls on the photosensitive CdS layer. The photodetector is in the high-resistivity state. Illumination of the photodetector by a light pulse from the photosensitivity region of CdS excites photoconductivity in the CdS layer. The resistivity in the layer decreases. The voltage in the structure is redistributed in favor of the LED. The LED begins to glow. The photodetector is switched into the low-resistivity state. The switching mechanism is governed by the positive optical feedback appearing in the device between the photosensitive layer and the LED. The emission of the LED is absorbed in the CdS layer. The resistance of that layer and the entire structure decreases. The current through the LED increases. The electroluminescence intensity increases, causing a further decrease in the resistance of the CdS layer. This avalanche process leads to the appearance of a segment with a negative differential resistance and a sharp current increase on the current-voltage characteristic of the device (Fig. 2). Variation of the level of the external illumination significantly alters the switching voltage and has practically no influence on the switching current. The photoreceptor remains in the low-resistivity state until a voltage exceeding the emission threshold of the LED (5–7 V) is supplied to it, i.e., the device stores the luminous signal from the external source, although the source may no longer be present, and uses its blue emission to signal it. The switching time of the photodetector is determined by the properties of the CdS layer and falls somewhere in the range 2–100 μs, depending on the fabrication conditions. The speed of the LED is $\sim$100 ns. Other photosensitive materials with a gap width $<$2.5 eV can be used instead of CdS. Accordingly, the semiconductor material will determine the spectral sensitivity range of the photodetector. Gallium nitride light-emitting diode structures containing alternating electron-accelerating and luminescence-generating layers, for example, M–CdS–i^+-GaN(Zn,O)–i-GaN(Zn)–i^+-GaN(Zn, O)–n-GaN–M, can be used to provide for operation of the photodetector with voltages of either polarity on the heterostructure.[3]

The photodetector presented in this paper is actually a multifunctional optoelectronic device. It can be a photodetector, an emitter, a memory cell, an element with optical information output, an illumination indicator, i.e., a photorelay, an optical switch, etc.

This research was performed with partial support from the University of Arizona (U.S.A.).

[1] A. G. Drizhuk, M. V. Zaĭtsev, V. G. Sidorov, and D. V. Sidorov, Pis'ma Zh. Tekh. Fiz. **22** (6), 67 (1996) [Tech. Phys. Lett. **22**, 259 (1996)].
[2] A. M. Pavolets, G. A. Fedorus, and M. K. Sheĭnkman, Poluprovodn. Tekh. Mikroelektron. **12**, 71 (1973).
[3] A. G. Drizhuk, M. V. Zaĭtsev, V. G. Sidorov, and D. V. Sidorov, Pis'ma Zh. Tekh. Fiz. **22** (13), 33 (1996) [Tech. Phys. Lett. **22**, 533 (1996)].

Translated by P. Shelnitz
Edited by David L. Book

ZnTe–GaN heterostructure switching device

A. G. Drizhuk, V. G. Sidorov, D. V. Sidorov, and M. D. Shagalov

Vologda Polytechnical Institute, Vologda, Russia
(Submitted 27 June 1997)
Pis'ma Zh. Tekh. Fiz. **23**, 79–82 (October 26, 1997)

A bistable device, in which switching is effected by an external voltage pulse and the stable states are stored as the color of the light emitted, is fabricated on the basis of an M–$i-n$-GaN light-emitting diode structure by depositing a layer of ZnTe on it. The properties of the device and its operating principle are presented. © *1997 American Institute of Physics.* [S1063-7850(97)03110-8]

The principal elements in automation systems are probably switching devices and the devices which signal the state of these elements. The switch proposed in this paper combines these functions in a single device (Fig. 1). It consists of a three-layer gallium nitride structure grown on a sapphire substrate by vapor-phase epitaxy in a chloride–hydride system. A buffer layer of undoped n-GaN was grown at 1050°C and a growth rate of ~ 20 μm/h, which provided it and the higher-lying layers with high crystal perfection. The thickness of the layer was $10-20$ μm, and its conductivity was $\sim 10^3$ $\Omega^{-1}\cdot\mathrm{cm}^{-1}$. Then the following layers were grown successively at 950°C: a gallium nitride layer doped with both zinc and oxygen and a gallium nitride layer doped only with zinc. The layers had the following parameters: $0.3-3$ μm and 10^3-10^5 $\Omega\cdot$cm; $0.05-0.5$ μm and 10^5-10^7 $\Omega\cdot$cm, respectively. The total resistance was selected so that the resistance of the i-GaN(Zn) layer would be approximately an order of magnitude greater than the resistance of the i^+-GaN(Zn, O) layer.

Such an M–i-GaN(Zn)–i^+-GaN(Zn, O)–n-GaN structure is a light-emitting diode (LED) that emits blue light (the emission maximum lies at 2.55 eV), if a negative potential from a constant voltage source is supplied to the metallic contact on the i-GaN(Zn) layer.[1] With this polarity of the voltage, electrons are accelerated in the strong electric field of the i-GaN(Zn) layer to energies sufficient to excite the Zn–O centers located in the following i^+-GaN(Zn,O) layer.

To fabricate the switching device, a layer of high-resistivity zinc telluride was grown from the vapor phase on the surface of the i-GaN(Zn) layer of the LED structure in a quasiclosed chamber.[2] The thickness of the layer was $1-5$ μm, and the total resistance exceeded the total resistance of the i-GaN(Zn) layer by an order of magnitude or more. The contact on the ZnTe layer was made from vacuum-sputtered gold, and the contact on the n-GaN layer was made from indium.

The M–ZnTe–i-GaN(Zn)–i^+-GaN(Zn, O)–n-GaN–M heterostructure thus created can operate as a device with switching from a high-resistivity state to a low-resistivity state and retention of the stable states as the color of the light emitted. The operating principle is as follows. At a certain small working voltage the device is in the high-resistivity state. Almost all the voltage applied to the heterostructure falls on the higher-resistivity ZnTe layer, where orange electroluminescence with a maximum at ~ 2 eV is excited in a strong electric field. The band gap at 300 K is equal to 2.26 eV. An additional pulse, which increases the total voltage on the structure above the level corresponding to the threshold electric field strength in the ZnTe layer ($>10^5$ V/cm) causes reversible local electric breakdown in ZnTe. This leads to a decrease in the resistance of the ZnTe layer and, thus, in the resistance of the entire structure. The switching voltage equals 5–15 V and is determined by the electric and geometric parameters of the ZnTe layer. In the low-resistivity state the voltage in the structure is redistributed from the ZnTe layer to the i-GaN(Zn) layer. When the potential from the

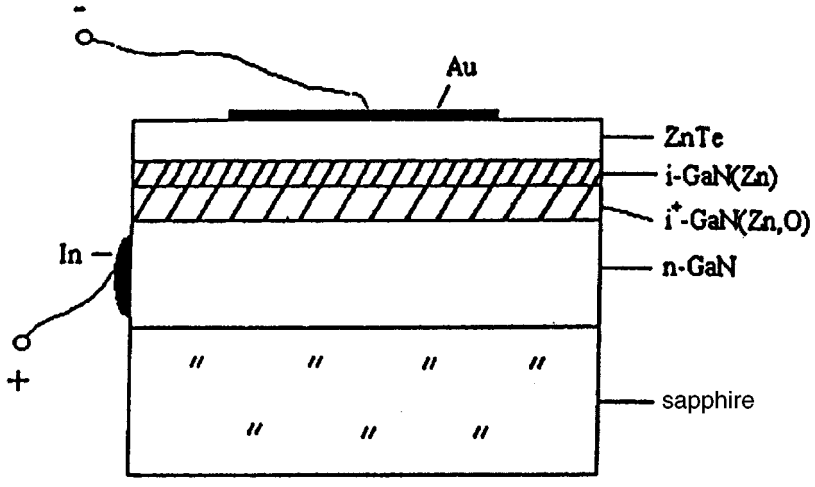

FIG. 1. Structure of the ZnTe–GaN switching device.

 1063-7850/97/100809-02$10.00 © 1997 American Institute of Physics

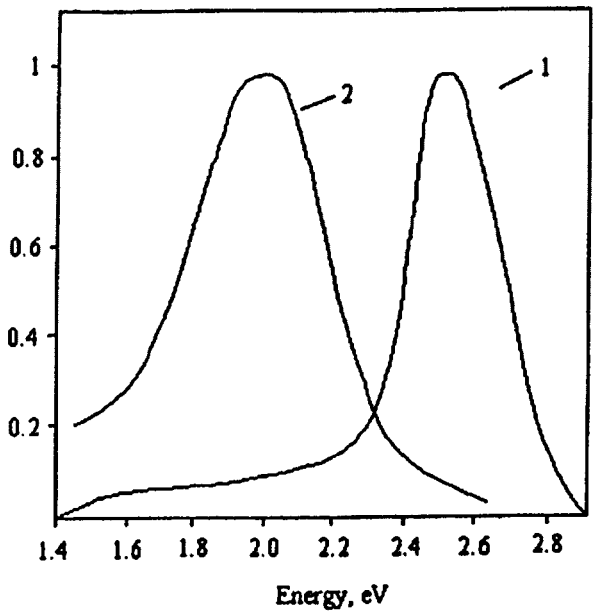

FIG. 2. Spectral characteristics of the electroluminescence of the ZnTe–GaN heterostructure in the low-resistivity (*1*) and high-resistivity (*2*) states. The spectra have been normalized to unity.

voltage source in the ZnTe layer is negative, the blue electroluminescence of the LED is ignited. The emission of the LED excites photoconductivity in the ZnTe layer and thereby further decreases its resistance. The positive feedback created leads to a sharp increase in the current through the LED, an increase in the electroluminescence intensity, and switching of the device into an even lower-resistivity state. The current-voltage characteristic is *S*-shaped. The spectral characteristics of the emission of the switching device in the low-resistivity and high-resistivity states are presented in Fig. 2. The intensity of the blue electroluminescence exceeds the intensity of the orange emission by an order of magnitude or more. When the voltage on the heterostructure has the opposite polarity (when the ''plus'' is on ZnTe), switching occurs only as a result of breakdown in the ZnTe layer, since the blue electroluminescence is not excited in the LED in this case. To create a switching device that operates under a voltage of either polarity, we can use any of the GaN LED structures proposed in Ref. 3. These LEDs consist of sequentially arranged i-GaN(Zn)–i^+-GaN (Zn,O)–i-GaN(Zn)–i^+GaN(Zn, O) layers and operate under voltages of either polarity.

The high-resistivity state of the device can be restored by switching off the external voltage. Under external illumination by white light the voltage needed to switch the device into the low-resistivity state decreases with increasing intensity. An increase in temperature has a similar effect. The switching time is $0.2-0.5$ μs under illumination and ~ 1 μs in the dark.

This research was performed with partial support from the University of Arizona (U.S.A.).

[1] A. G. Drizhuk, M. V. Zaĭtsev, V. G. Sidorov, and D. V. Sidorov, Pis'ma Zh. Tekh. Fiz. **22**(6), 67 (1996) [Tech. Phys. Lett. **22**, 259 (1996)].
[2] S. I. Radautsan, A. E. Tsurkan, and T. D. Shemyakova, in *Abstracts of Reports to the 4th Symposium on the Growth and Synthesis of Semiconductor Crystals and Films* [in Russian], Novosibirsk (1975), p. 93.
[3] A. G. Drizhuk, M. V. Zaĭtsev, V. G. Sidorov, and D. V. Sidorov, Pis'ma Zh. Tekh. Fiz. **22**(13), 33 (1996) [Tech. Phys. Lett. **22**, 533 (1996)].

Translated by P. Shelnitz
Edited by David L. Book

Possibility of analyzing deuterium–tritium gas mixtures using a time-of-flight mass spectrometer

N. N. Aruev, A. V. Kozlovskiĭ, I. L. Fedichkin, and G. L. Saksaganskiĭ

A. F. Ioffe Physicotechnical Institute, Russian Academy of Sciences, St. Petersburg, Russia;
Mettek Ltd., St. Petersburg, Russia;
D. V. Efremov Scientific-Research Institute of Electrophysical Apparatus, St. Petersburg, Russia
(Submitted 27 June 1997)
Pis'ma Zh. Tekh. Fiz. **23**, 83–87 (October 26, 1997)

The use of a time-of-flight mass spectrometer, whose ion source and detector operate in a synchronous regime, is proposed for the chemical and isotope analysis of gas mixtures containing radioactive tritium. The experiments performed confirm that the detector background current caused by tritium β electrons scarcely influences the signal-to-noise ratio and does not diminish the accuracy of analyses. © *1997 American Institute of Physics.* [S1063-7850(97)03210-2]

Mass-spectrometric methods are probably the most suitable for exact quantitative analyses of deuterium–tritium gas mixtures that will serve as fuels in thermonuclear reactors, particularly in the International Thermonuclear Experimental Reactor (ITER). Apart from the principal components D_2 and T_2, fuel mixtures can also contain such impurities as H_2, ^{3}He, ^{4}He, and O_2, oxides of various elements, hydrocarbons, N_2 and its compounds, etc., and the range of impurity concentrations can be very broad, extending from 10^{-5} to 5%. It follows from Ref. 1 that a mass spectrometer capable of performing complete isotope and chemical analyses of hydrogen-helium mixtures in the mass range $2-6$ u must have a high resolving power $R_{10\%}\approx 2500$ (the $^3He^+ - {}^3T^+$ doublet will still not be resolved) and high sensitivity.

Mass spectrometers of the quadrupole[2,3] or omegatron[4,6] types, as well as static magnetic instruments with double focusing,[7] are presently most often employed in the gas analysis of fuel mixtures in various thermonuclear facilities. One shared characteristic of these instruments is the fact that their ion sources and detectors operate in a continuous regime. The literature data[8] and the experience gained in working on magnetic resonance mass spectrometers[9,10] with gas mixtures containing small quantities of tritium show that the detector background currents caused by the β electrons formed as a result of the decay of tritium nuclei can increase by several orders of magnitude, if secondary-electron multipliers or microchannel plates operating in a continuous regime are employed in the detectors. This phenomenon precludes the measurement not only of the content of impurities in the gas mixture, but also the content of the principal components.

It has been theorized that a solution for the problem of analyzing tritium-containing gas mixtures can be achieved using a time-of-flight mass spectrometer of the mass reflectron type,[11] whose ion source and detector operate in a synchronous pulsed regime with the accumulation of ions during the time T of the pause between pulses. Since the temporal distribution of the noise caused by the β decay of tritium nuclei is uniform and since the noise current is proportional to the ratio τ/T (τ is the duration of the pulse which opens the detector), the shorter is τ, the smaller is the contribution of the noise current to the output signal.

An upper estimate of the principal component of the noise current can be obtained by assuming that for monolayer coverage there are $\sim 10^{15}$ tritium atoms on 1 cm^2 of the surface, for example, of a microchannel plate and that the active surface of a microchannel plate is ~ 10 cm^2. Taking into account that the half-life of tritium is $T_{1/2}\approx 4\times 10^8$ s, we find that the background current during the time of a working pulse $\tau\approx 2\times 10^{-8}$ s amounts to ~ 0.5 counts/s. At the same time, the ion packet (the useful signal) contains from a few to thousands of ions, depending on the sample composition, the pressure, the alignment, etc.

To test the hypothesis advanced we used a mass reflectron with a linear ion trajectory,[12] which was developed by Mettek Ltd.[13] and has the following characteristics: analyzer length, ~ 240 mm; ion trajectory length, $L\sim 180$ mm; resolving power in the mass range $2-4$ u, $R_{10\%}\approx 50-60$; sensitivity at a partial pressure of Ar$\sim 10^{-8}$ Pa; dynamic range, 10^6-10^7; range of measurable masses, $1-150$ u; time for the detection of 20 gas components, ~ 1 s. The vacuum chamber and all the internal assemblies and parts of the mass reflectron are made from stainless steel, and porcelain serves as an insulating material. The analyzer and the injection system specially made for these experiments are evacuated by oil-free pumps operating without cooling by water or liquid nitrogen. After preliminary alignment, the instrument operates in an automated regime.

The main objectives of the experiments performed were to record the $^3T_2^+$ molecular peak and to investigate the influence of the detector background current on the error in measurements of the intensities of the lines in the mass spectrum during prolonged operation of the instrument with tritium.

Before the main measurements, only the $^1H^+$, $^1H_2^+$, $^4He^+$, $^{14}N^+$, and $^{16}O^+$ lines were detected in the spectrum of the residual gas at $P_{\rm res}\approx 10^{-6}$ Pa. After injection of a tritium sample (at the starting time t_0) to a working pressure $P_{\rm work}\approx 10^{-4}$ Pa, the intensities of the peaks just indicated remained practically unchanged, and an unresolved $^3T^+ + {}^3He^+$ peak and a $^3T_2^+$ molecular peak appeared in the spectrum. Since the gas under investigation was injected into the analyzer from a small volumetric vessel with a volume of ~ 0.5 cm^3, during a prolonged operating period ($t_1 - t_0 \approx 40$

TABLE I.

Ions measured	Intensity of peaks at the time				Measurement error, %
	t_0	t_1	t_2	t_n	
$^1H^+$	15	17	20	23	0.2
$^1H_2^+$	174	204	214	203	0.2
$^3T^+ + ^3He^+$	1001	910	894	1045	0.4
$^4He^+$	44	40	39	51	0.1
$^3Te_2^+$	306	284	280	307	0.2
$^{14}N^+$	46	54	56	57	0.2
$^{16}O^+$	45	59	63	52	0.2

min, $t_2 - t_0 \approx 80$ min) the pressure in the volumetric vessel and, accordingly, the intensities of the $^3T^+ + ^3He^+$ and $^3T^+$ peaks decreased by about 10% from the their initial values. Restoration of the pressure in the volumetric vessel at t_n ($t_n - t_0 \approx 120$ min) led to restoration of the intensities of the tritium molecular peak and the unresolved $^3T^+ + ^3He^+$ peak. The mass lines were recorded automatically without any fine adjustment of the instrument.

The first results of an analysis of a gas mixture containing tritium on a time-of-flight mass spectrometer are presented in Table I. The intensities of the measured lines in the mass spectrum are given in arbitrary units.

The results obtained show that the intensity of the unresolved $^3T^+ + ^3He^+$ peak significantly exceeds the intensity of the $^3T_2^+$ molecular peak. This is attributed to the fact that the age of the tritium sample exceeded 20 years, and radiogenic ^3He became the main component in the sample. The presence of fairly intense $^{14}N^+$ and $^{16}O^+$ peaks in the spectrum attests to the insufficient degree of heating and degassing of the analyzer. We did not detect any influence of the background current caused by the β decay of tritium on the intensities of the measured peaks or on the error in the measurements of the gas components, although the measurements were continued for more than 2 h. The experience gained in working with a detector operating in a continuous regime[9,10] has revealed that the level of the background current caused by β electrons begins to increase immediately after the injection of tritium into the analyzer.

In our opinion, the experimental data obtained allow us to confidently assert that a time-of-flight mass spectrometer operating in a synchronous detection regime makes it possible to eliminate the influence of the background current caused by the β decay of tritium nuclei and to analyze the composition of gas mixtures containing tritium with a high accuracy. As calculations show, for a sufficiently reliable (but not complete, as in Ref. 1) quantitative analysis of hydrogen-helium mixtures, the resolving power of the mass spectrometer must be $R_{10\%} \approx 500$. There are a number of ways to increase the resolving power of a mass reflectron.[14] This work is presently being conducted.

[1] S. A. Alekseenko, N. N. Aruev, B. A. Mamyrin *et al.*, At. Energ. **51**, 27 (1981).
[2] R. E. Ellefson, W. E. Moddeman, and H. F. Dylla, J. Vac. Sci. Technol. **18**, 1062 (1981).
[3] S. Hiroki, T. Abe, Y. Murakami *et al.*, J. Vac. Sci. Technol. A **12**, 2711 (1994).
[4] U. Engelmann, M. Glugla, R. D. Perzhorn, and H. J. Ache, Nucl. Instrum. Methods Phys. Res., Sect. A **302**, 345 (1991).
[5] U. Engelmann and G. Vassalo, Fusion Eng. Des. **28**, 324 (1995).
[6] R. Lässer, C. J. Caldwell-Nichols, J. Dallimore *et al.*, Preprint No. JET-P(91)25, pp. 73–78.
[7] N. N. Ryazantseva and A. I. Davydov, At. Energ. **76**, 125 (1994).
[8] M. E. Malinovski, Preprint No. SAND 79-8218, Sandia Livermore National Laboratory, Livermore, CA (1979).
[9] B. A. Mamyrin, S. A. Alekseenko, and N. N. Aruev, Zh. Éksp. Teor. Fiz. **80**, 2125 (1981) [Sov. Phys. JETP **53**, 1109 (1981)].
[10] N. N. Aruev, E. L. Baĭdakov, B. A. Mamyrin, and A. V. Yakovlev, Zh. Tekh. Fiz. **57**, 300 (1987) [Sov. Phys. Tech. Phys. **32**, 180 (1987)].
[11] B. A. Mamyrin, V. I. Karataev, D. V. Shmikk, and V. A. Zagulin, Zh. Éksp. Teor. Fiz. **64**, 82 (1973) [Sov. Phys. JETP **37**, 45 (1973)].
[12] B. A. Mamyrin and D. V. Shmikk, Zh. Eksp. Teor. Fiz. **76**, 1500 (1979) [Sov. Phys. JETP **49**, 762 (1979)].
[13] A. V. Kozlovskiĭ, Mettek Ltd. (applicant), ''Mass spectrometer for gas analysis,'' Favorable decision regarding patent application No. 96102272.07 (7 February 1996).
[14] B. A. Mamyrin, Int. J. Mass Spectrom. Ion Processes **131**, 1 (1994).

Translated by P. Shelnitz
Edited by David L. Book

Nonequilibrium processes in $Hg_{1-x}Cd_xTe$ n^+-p junctions in a magnetic field

I. S. Virt

I. Franko Drogobych State Pedagogic Institute, Drogobych, Ukraine
(Submitted 10 April 1997)
Pis'ma Zh. Tekh. Fiz. **23**, 88–94 (October 26, 1997)

The results of measurements of the relaxation and current–voltage characteristics of $Hg_{1-x}Cd_xTe$ n^+-p junctions in a magnetic field are presented. It is shown that the lifetime of the nonequilibrium electrons in the p-type region undergoes an increase in a magnetic field, which can be associated with the heterogeneous distribution of defects from the junction boundary. The current-voltage characteristics in a magnetic field exhibit suppression of the diffusion component of the current and an increase in the contribution of the generation–recombination channel, as well as the appearance of shunting channels, which are associated with the influence of the surface. © *1997 American Institute of Physics.*
[S1063-7850(97)03310-7]

Electron–hole junctions in $Hg_{1-x}Cd_xTe$ comprise a major component for the creation of devices for infrared technology.[1,2] The technologies for obtaining doped surface layers in these crystals are associated with certain difficulties due to the comparatively easy occurrence of defect formation.[1] For this reason, the structural makeup of n^+-p junctions is fairly complicated,[2,3] One of the methods for studying the structure of $n-p$ junctions is to investigate their recombination characteristics.[4]

This paper presents the results of investigations of n^+-p junctions in magnetic fields. Junctions with an area $A=50\times 50$ μm^2 were fabricated by implanting B^+ ions in p-$Hg_{08}Cd_{02}Te$ crystals with $p\approx 2\times 10^{15}$ cm^{-3} at 100 keV. Current pulses with a duration of 1–2 μs were supplied from a G5-54 generator in the forward direction in the temperature range 300–77 K. The magnetic field was created by a permanent magnet with a strength from 0.0 to 0.8 T in the direction perpendicular to the n^+-p junction. The voltage relaxation curves were recorded using an S8-13 storage oscillograph. The current–voltage characteristics were also measured.

The shape of the injection pulse at $T=77$ K has the form presented in Fig. 1 (inset) when the pulse voltage $U=2.4$ V. The postinjection curve consists of two segments. At first there is an almost instantaneous ohmic voltage drop on the base layer of the n^+-p junction. It is followed by a second segment, which is determined by the recombination of nonequilibrium charge carriers on both sides of the n^+-p junction. Since the doping level of the electron region is considerably higher than that of the hole region, the pulse relaxation time is determined by the larger of the lifetimes of

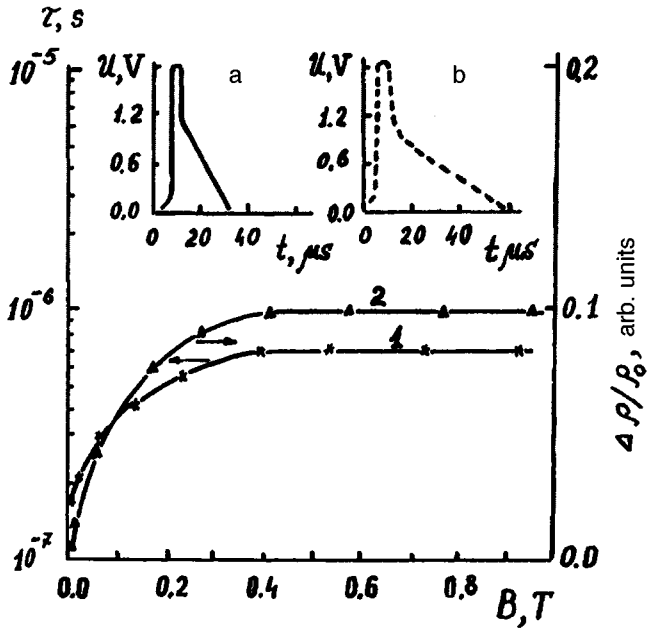

FIG. 1. Field dependence of the lifetime of nonequilibrium charge carriers in the p-type region (*1*) and relative variation of the magnetoresistance of the base layer (*2*) of a $Hg_{08}Cd_{02}Te$ n^+-p junction at 77 K. The inset shows oscillograms of the injection voltage in zero magnetic field (a) and at $B=0.3$ T (b).

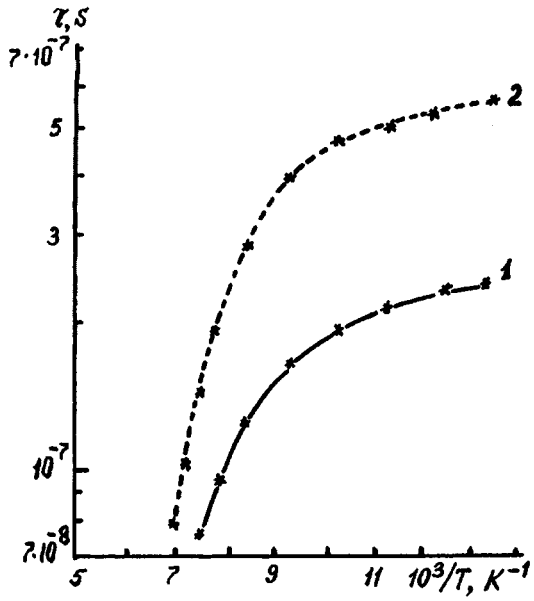

FIG. 2. Temperature dependence of the lifetime of nonequilibrium charge carriers in the p-type region in zero magnetic field (*1*) and at $B=0.3$ T (*2*) for a $Hg_{08}Cd_{02}Te$ n^+-p junction.

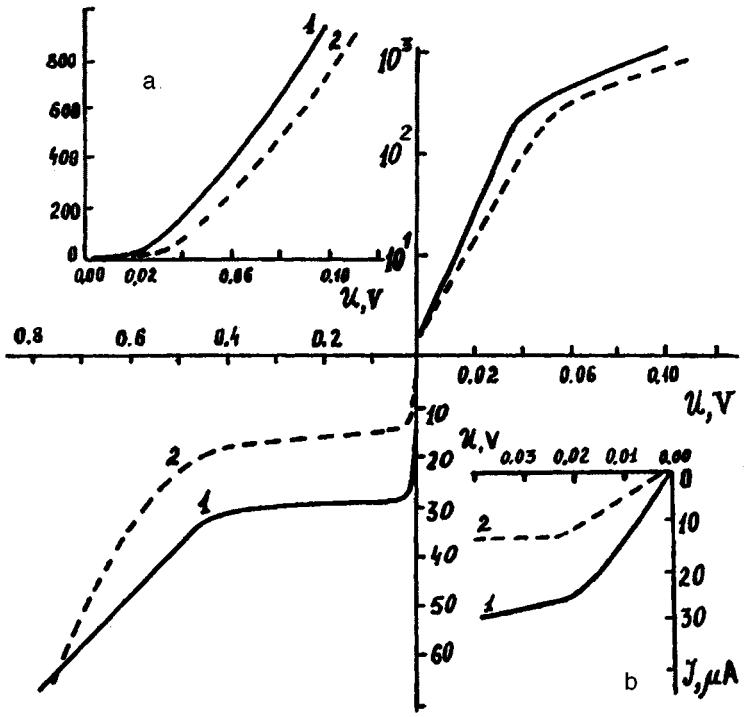

FIG. 3. Current–voltage characteristic of a n^+-p junction in zero magnetic field (*1*) and at $B=0.3$ T (*2*). Inset: a — forward branch of the current–voltage characteristic in linear coordinates; b — linear segment of the reverse branch of the current–voltage characteristic on a magnified scale.

the nonequilibrium charge carriers, which corresponds to the region with less doping, i.e., the electron lifetime τ_n in the p-type region of the junction. The value of τ_n was determined from the linear segment[5] achieved on the postinjection dependence of the voltage

$$(\tau_n)^{-1}=\frac{e}{kT}\frac{\Delta U}{\Delta t}, \tag{1}$$

where $\Delta U/\Delta t$ is the slope of the segment, e is the electron charge, and k is Boltzmann's constant.

The value of τ_n [on the $\tau_n(B)$ curve] at 77 K increases with increasing magnetic fields (Fig. 1) about threefold at a value of the magnetic field $B\approx 0.2$ T and then reaches saturation. The relative change in the resistivity of the base layer $\Delta\rho/\rho_0$ as a function of B, which was determined from the magnitude of the ohmic component of the tailing edge of the pulse, behaves in the same manner.

The dependence of τ_n on the magnetic field is attributed to the fact that recombination of the nonequilibrium charge carriers takes place in different portions of the p-type region. More specifically, as the field increases, the recombination region moves closer to the boundary of the n^+-p junction. The effective diffusion length of the nonequilibrium electrons $L_n=\sqrt{D_n\tau_n}$ (D_n is the diffusion coefficient) in a magnetic field obeys the expression

$$L_n(B)=\sqrt{\frac{D_n\tau_n}{1+\mu_n^2B^2}} \tag{2}$$

(μ_n is the electron mobility). Thus, while $L_n(0)\approx 250$ μm in a material with p-type conduction,[6] at $B\approx 0.8$ T the diffusion length decreases to approximately $L_n(B)\approx 30$ μm. The increase in τ_n thus provides evidence that the recombination properties of these regions are different.

The $\tau_n(T)$ curves (Fig. 2) indicate an Auger mechanism for recombination of the nonequilibrium carriers and that the type of mechanism does not change in a magnetic field. The value of τ_n increases over the entire temperature range for impurity conduction. Under an Auger recombination mechanism this can be associated with a decrease in the acceptor concentration N_A as the junction boundary is approached. According to the $\tau_n(B)$ curve, the coordinate distribution is approximately constant at distances from the n^+-p junction up to 30 μm. Estimation of the concentration of equilibrium holes in the p-type region from the expression $\tau_n=b/p^2$ (b is the Auger recombination constant[6]) reveals that the concentration gradient of the acceptors at the distances 250 μm$\gtrsim d\gtrsim$30 μm is grad $P\approx 10^{17}$ cm^{-4}. During implantation, Frenkel defects can form in the mercury sublattice in the near-surface layers of the crystal as a result of the migration of interstitial mercury atoms into the p-type region, and they can subsequently partially recombine with the mercury vacancies that determine the acceptor concentration.

The form of the current–voltage characteristics also changes in a magnetic field (Fig. 3). On the forward branches of the current–voltage characteristics $[J(U)=J_s\exp(eU/\beta kT)]$ the nonideality parameter increases from $\beta\approx 1.1$ ($B=0$) to $\beta\approx 1.7$ ($B=0.3$ T). On the reverse branch the current decreases, and a slight dependence on the voltage appears. The differential resistance at zero bias $R_0=(\partial U/\partial J)_{U=0}$ increases twofold. These data attest to an increase in the contribution of the generation–recombination component (J_{GR}) to the flow of current. Suppression of the diffusion component (J_D) occurs, because it depends on the magnetic field:[7]

$$J_D = \sqrt{\frac{D_n}{(1+\mu_n^2 B^2)\tau_n}}\frac{n_i^2}{N_A}, \tag{3}$$

where n_i is the intrinsic carrier concentration. In the limit $\mu_n^2 B^2 \gg 1$, J_D decreases with the field as $J_D \sim (B)^{-1}$. The tunneling component, which is manifested at a reverse bias in the range $0.20-0.55$ V, also varies. In this range the current–voltage characteristics are described by the expression:[8]

$$J_T \sim U(U+U_{\text{con}})\exp\left[-\frac{C}{(U+U_{\text{con}})^{1/2}}\right], \tag{4}$$

where U_{con} is the contact potential difference and C is a constant which depends on the doping level of the n- and p-type regions. The less steep dependence of the tunneling branch of the current–voltage characteristic in a magnetic field indicates that the band spectrum is altered in the vicinity of the barrier in the n^+-p junction. In particular, the parameter C obeys the relation

$$C \sim E_g^{3/2}\sqrt{\frac{m_e^*}{N_A}}, \tag{5}$$

where m_e^* is the effective electron mass and E_g is the gap width. It can be presumed that the decrease in J_T is related to the increase in m_e^* due to Lorentz twisting by the magnetic field.

At reverse biases $U > |-0.55|$ V such channels with an ohmic resistance $R_{\text{sh}} \approx 10^4\ \Omega$ contribute to the flow of current. The value of the parallel resistance decreases to $R_{\text{sh}} \approx 5\times 10^3\ \Omega$ in a magnetic field. Most probably, the deflection of electrons toward the surface promotes their passage along the ohmic channels in the near-surface layers.

It follows from the present experimental data that in $Hg_{1-x}Cd_xTe$ n^+-p junctions created by the ion implantation of B^+ ions there is a slight concentration gradient of the acceptors at a sufficient distance along with the sharp concentration gradients of the dopant and the intrinsic defects. In a magnetic field the contribution of the surface to the flow of current increases, particularly because of an increase in the generation–recombination component.

[1] S. C. Shen, Semicond. Sci. Technol. **8**, 443 (1993).
[2] S. V. Belotelov, V. I. Ivanov-Omskiĭ, A. I. Izhnin, and V. A. Smirnov, Fiz. Tekh. Poluprovodn. **25**, 1058 (1991) [Sov. Phys. Semicond. **25**, 637 (1991)].
[3] H. F. Shaake, J. Vac. Sci. Technol. A **4**, 2174 (1984).
[4] M. G. Andrukhiv, S. V. Belotelov, and I. S. Virt, Fiz. Tekh. Poluprovodn. **27**, 1863 (1993) [Semiconductors **27**, 1026 (1993)].
[5] Yu. R. Nosov, *Switching in Semiconductor Diodes*, Plenum Press, New York (1969).
[6] A. V. Lyubchenko, E. A. Sal'kov, and F. F. Sizov, *Physical Principles of Semiconductor Infrared Photoelectronics* [in Russian], Naukova Dumka, Kiev (1984).
[7] S. E. Schacham and E. Finkman, J. Vac. Sci. Technol. A **7**, 387 (1989).
[8] N. L. Bazhenov, S. I. Gasanov, V. I. Ivanov-Omskiĭ, K. E. Mironov, and K. D. Mynbaev, Fiz. Tekh. Poluprovodn. **25**, 2196 (1991) [Sov. Phys. Semicond. **25**, 1323 (1991)].

Translated by P. Shelnitz
Edited by David L. Book